Author: Ivashko, Artem
Title: Sterile neutrinos in the early Universe
Issue Date: 2015-12-09

Sterile neutrinos in the early Universe

Proefschrift

ter verkrijging van
de graad van Doctor aan de Universiteit Leiden,
op gezag van Rector Magnificus prof. mr. C.J.J.M. Stolker,
volgens besluit van het College voor Promoties
te verdedigen op woensdag 9 december 2015
klokke 11.15 uur

door

Artem Ivashko

geboren te Kiev (Oekraïne)
in 1987

Promotor: Prof. Dr. A. Achúcarro
Co-promotor: Dr. A. Boyarsky

Promotiecommissie:

Leden: Dr. M. Drewes (TU München, München, Duitsland)
Dr. O. Ruchayskiy (EPFL, Lausanne, Zwitserland)
Prof. Dr. S. Vilchinskiy (Taras Shevchenko University, Kiev, Oekraïne)
Prof. Dr. E.R. Eliel
Prof. Dr. V. Vitelli

Casimir PhD series Delft-Leiden 2015-30

ISBN 978-90-8593-236-9

An electronic version of this thesis can be found at `https://openaccess.leidenuniv.nl`

The cover shows a configuration of magnetic field with non-vanishing magnetic helicity, which can be generated in the early Universe as a consequence of the processes involving sterile neutrinos (the upper image), and the setup of the SHiP experiment at CERN (`http://cern.ch/ship`), which aims to detect sterile neutrinos N (the lower image).

To my family

Contents

1 Introduction 9

1.1 The Standard Model of particle physics . . . 9
1.2 Beyond the Standard Model (BSM) phenomena . . . 10
  1.2.1 Neutrino masses and oscillations . . . 10
  1.2.2 Dark matter . . . 11
  1.2.3 Matter-antimatter asymmetry of the Universe . . . 13
  1.2.4 Approaches to resolve the BSM problems . . . 14
1.3 Sterile neutrinos and the νMSM model . . . 15
  1.3.1 Sterile neutrinos in the early Universe . . . 18
  1.3.2 Sterile neutrino Dark Matter . . . 24
  1.3.3 Generation of the baryon asymmetry with sterile neutrinos 27
  1.3.4 The Neutrino Minimal Standard Model . . . 32
  1.3.5 Lepton asymmetry and magnetic fields . . . 33
  1.3.6 Electric current along the magnetic field . . . 34
  1.3.7 Chiral Magnetic Effect . . . 36
  1.3.8 Chiral anomaly and dynamics of chiral imbalance . . . 37
  1.3.9 Accelerator searches of sterile neutrinos . . . 40
1.4 This thesis . . . 41
  1.4.1 Chapter 2 . . . 41
  1.4.2 Chapter 3 . . . 42
  1.4.3 Chapter 4 . . . 42
  1.4.4 Chapter 5 . . . 43

2 Experimental bounds on sterile neutrino mixing angles 45

2.1 Introduction . . . 45
  2.1.1 Previous bounds on sterile neutrino interactions . . . 46
2.2 Sterile neutrino Lagrangian . . . 48
  2.2.1 Two quasi-degenerate sterile neutrinos . . . 48
2.3 Solution of the see-saw equations . . . 49
  2.3.1 Parametrization of the Dirac mass matrix . . . 49
  2.3.2 Normal hierarchy . . . 50
  2.3.3 Inverted hierarchy . . . 52

2.3.4 Ratio of sterile neutrino mixing angles for $|z| \sim 1$ 56
2.3.5 Minimal mixing angles in the νMSM 57
2.4 Experimental bounds on sterile neutrino mixings 58
2.4.1 Peak searches 59
2.4.2 Fixed target experiments and neutral currents contribution 59
2.4.3 Reinterpretation of the PS191 and CHARM experiments . . 59
2.4.4 A note on Majorana vs Dirac neutrinos 63
2.5 Results 64
2.5.1 Bounds on the mixing angles of sterile neutrinos 64
2.5.2 The lower bound on the lifetime of sterile neutrinos 64
2.6 Discussion 66

3 Influence of sterile neutrinos on primordial nucleosynthesis 69
3.1 Introduction: Particle physics processes in the expanding Universe 69
3.1.1 Big Bang Nucleosynthesis 69
3.1.2 Influence of decaying particles on primordial nucleosynthesis 70
3.2 Primordial nucleosynthesis with sterile neutrinos 71
3.2.1 Expanding Universe and distributions of particles 72
3.2.2 Baryonic matter 73
3.2.3 Active neutrinos at MeV temperatures 74
3.2.4 Inclusion of neutrino oscillations 75
3.2.5 The impact of sterile neutrinos 78
3.2.6 Course of nuclear reactions 80
3.2.7 Adopted values of abundances of the light nuclei 81
3.3 Tests of the numerical approach 83
3.3.1 Standard Model BBN 83
3.3.2 Test of energy conservation 84
3.3.3 Heavy sterile Dirac neutrino 86
3.3.4 Massive ν_τ 86
3.3.5 Late reheating model 86
3.3.6 Instant thermalization of decay products 88
3.4 Results 89
3.5 Discussion 92

4 Sterile neutrinos between baryogenesis and nucleosynthesis 97
4.1 Leptogenesis and chiral magnetic effect 97
4.2 Chiral Magnetic Effect and non-zero fermion mass 99
4.3 Asymmetric population of left/right helical states 102
4.3.1 Plasma in homogeneous magnetic field 102
4.3.2 Plasma in inhomogeneous magnetic field 103
4.4 Axial self-energy of the fermions 105
4.4.1 Homogeneous magnetic field 106
4.4.2 Inhomogeneous magnetic field 108
4.4.3 Thermal and vacuum contributions to the parity-odd terms 111

4.5 Gauge invariance and Chern-Simons term 114
4.6 Discussion 115
4.A Quantum mechanics of fermions with axial self-energy 117

5 Chiral Magnetic Effect from parity-violating interactions 121
5.1 Chern-Simons term as a result of particle interactions 121
5.2 Theory with $U(1)_{\text{vector}} \times U(1)_{\text{axial}}$ gauge group 123
5.3 1-loop vacuum corrections to Compton scattering 126
5.4 $ff\gamma \to ff\gamma$ diagrams 128
  5.4.1 Self-energy diagrams 130
  5.4.2 $Z\gamma$ mixing diagrams 131
5.5 Discussion 131

Samenvatting 151

Summary 155

List of publications 157

Curriculum vitæ 159

Acknowledgements 161

Chapter 1

Introduction

1.1 The Standard Model of particle physics

One of the greatest achievements of theoretical physics in the XX century is the establishment of the Standard Model (SM) of elementary particles and interactions. This theory describes successfully the Universe at the smallest known scales (probed at high-energy accelerators like the Large Hadron Collider at CERN), and at the largest, cosmological scales. Historically, the electromagnetic forces (like those which bind nuclei and electrons into atoms), the weak forces (responsible for the nuclear beta-decay) and the strong forces (which form nuclei from nucleons) were thought to be disconnected in their origin. However, the attempts to build a consistent theory of weak interactions gave unphysical predictions for the scattering processes (like $e\nu \to e\nu$) at large energies. In order to change the situation, it was suggested that weak and electromagnetic interactions are unified at large energies [1, 2, 3], in a framework of $SU_L(2) \times U_Y(1)$ gauge theory. This unification predicted the existence of new particles, and in further attempts to build a complete and self-consistent theory, people were *forced* to introduce even more new particles. Since the 1960s, when the simplest version of the unified theory was first proposed, we have found many of these particles. Together with the recent discovery of the Higgs boson, *all* the predicted particles have been finally observed, and their properties match the theoretical predictions. Meanwhile, it turned out that the strong interactions are mediated by gauge forces as well [4, 5] with group $SU_C(3)$, which allowed to include the strong interactions in the framework of a single $SU_L(2) \times U_Y(1) \times SU_C(3)$ gauge theory. This theory is actually what we call the Standard Model.

It is worth noting here that the SM has a peculiar structure. First, there is the intrinsic violation of parity under spatial reflections (P-violation). In particular, neutrinos can be only left-handed, and although the other fermions have both left and right components, these left and right components act differently in electroweak interactions (for example, right components do not take part in $SU_L(2)$ interaction). Second, the fermions are organized in three copies (generations), which have identical properties, except for the mass. Among the other peculiarities are the very small magnitude of CP-violation and the wide range of the masses of fermions (they span many orders of magnitude).

1.2 Beyond the Standard Model (BSM) phenomena

Despite the great success of the SM, which has been confirmed in numerous accelerator experiments, in the process of testing this model a number of *observable* phenomena in particle physics, astrophysics, and cosmology were found that remain unexplained. These problems, which usually are referred to as the *Beyond the Standard Model* (BSM) problems, indicate that the SM is not the final theory. It is worth noting that the BSM problems were found initially in the *non-accelerator observations*, as we will see below.

1.2.1 Neutrino masses and oscillations

The first BSM problem that we will consider is the existence of **neutrino oscillations**. In the Standard Model, there are three types (flavours) of neutrinos: electronic (ν_e), muonic (ν_μ), and tauonic (ν_τ). **Neutrino oscillations are the transitions of one neutrino flavour into another, which take place even in empty space (in vacuum).**

The existence of these transitions indicates that the numbers of particles of a given flavour (lepton numbers) are not conserved individually. The indication for neutrino oscillations was first found in studies of fluxes of solar neutrinos [6], which were different from the theoretical expectations based on the so-called Standard Solar Model. The experimental evidence in favour of oscillations has grown: oscillations were confirmed for neutrinos that come from interactions of high-energy particles with the Earth atmosphere [7], reactor neutrinos [8, 9, 10] and accelerator neutrinos [11, 12, 13] oscillate as well. The results of all the well-established experiments in the domain of oscillations fit into the three-flavour mixing scheme [14], for a review, see [15]. In this scheme, neutrinos have mass, but a state with definite flavour does not have a definite mass. In other words, the basis of quantum-mechanical *mass* eigenstates does not coincide with the basis of *flavour* eigenstates, but these two bases are related by a non-trivial linear transformation described by unitary matrix, which is called the Pontecorvo-Maki-Nakagawa-Sakata matrix [16, 17, 18].

It is interesting to note that neutrino oscillations *can* be included in the Standard Model. Indeed, oscillations can be described by including the Majorana mass terms $m_{\alpha\beta}\overline{\nu_\alpha^c}\nu_\beta$ in the Lagrangian. However these terms do not obey $SU_L(2)$

gauge invariance of the theory, since the neutrino field ν_α $(\alpha = e, \mu, \tau)$ is a component of the $SU_L(2)$ lepton doublet L $(L_e = (\nu_e, e)^T)$, which mixes with the other component under the gauge transformation. In order to write a gauge-invariant Lagrangian, which describes neutrino masses, one has to introduce the Higgs doublet field H,

$$\Delta\mathcal{L} = \sum_{\alpha,\beta} \frac{F_{\alpha\beta}}{\Lambda} (\overline{L_\alpha}\tilde{H})(H^\dagger L^c_\beta), \tag{1.1}$$

As a result, we get a higher-order operator, the so-called Weinberg operator [19]. Here $L^c = i\gamma^2(L^\dagger_\alpha)^T$ is the charge-conjugated leptonic field, $\tilde{H} = i\sigma_2(H^\dagger)^T$. Then, after the spontaneous breaking of electroweak symmetry, neutrinos receive masses of order Fv^2/Λ, where $v \sim 200\,\mathrm{GeV}$ is the vacuum expectation value of the Higgs field, and F is a typical value of the matrix elements $F_{\alpha\beta}$. By a rescaling of variables F and Λ, one can make $F \sim 1$ without loss of generality. Noting that the cosmological and terrestial observations imply an upper bound on the neutrino masses of order of eV [20, 21], we conclude that $\Lambda \gtrsim 10^{14}\,\mathrm{GeV}$. Although the Standard Model can accomodate the neutrino oscillations by introducing the Weinberg operator, this higher-order correction implies existence of new physics (which is not captured by the Standard Model) at the energy E which cannot be higher than Λ.[1] At the same time, although the energy scale of $10^{14}\,\mathrm{GeV}$ is huge, it is still much smaller than the Planck mass $M_{\mathrm{Pl}} \sim 10^{19}\,\mathrm{GeV}$, which is thought to be the scale where on the one hand, gravity can be no longer described classically, and on the other hand, the actual quantum description is not known. Therefore, the new physics indicated by presence of the Weinberg operator is expected to be in the regime where gravity is not quantized.

1.2.2 Dark matter

The evidence of the second phenomenon beyond the Standard Model was found outside the Earth, and is related to the existence of the so-called **Dark Matter** (DM). Dark matter manifests itself via different independent types of observations, at very different lengthscales, starting from changing the motion of stars [22] and galaxies, and up to the cosmological scales, affecting formation of large-scale structures and dynamics of the Universe as a whole [23].

---

[1] Otherwise, at higher energies, the unitarity of the scattering matrix is lost, so that some scattering processes can have probability larger than 1, which makes theory inconsistent.

There are three independent traces of gravitational potential in astrophysical systems (velocity curves of stars and galaxies, X-ray emission of intergalactic gas and gravitational lensing [24]) that all show that **gravity in these objects deviates significantly from what is predicted for the observed distributions of ordinary matter by Newton's (or, equally Einstein's) theory of gravity**. Independently, the observed properties of CMB suggest that without an additional component that does not interact with light, ordinary matter would not have enough time to develop all the structure observed in the Universe at the present day [25, 26, 27]. This body of independent evidence suggests that some additional matter, called *Dark Matter* really exists.

In all these cases, however, the only way DM manifests itself is through gravitational interactions with ordinary matter. The origin of this effect can be either in the existence of massive particles that are not involved in the SM gauge interactions (then indeed we deal with "matter"), or in modifications of the laws of gravity. The attempts to modify the gravitational laws at large scales encounter many problems, both from theoretical and experimental sides. The scenario where the DM is composed of particles is simple, natural and universal (for a review, see [28, 29]).

But if the Dark Matter is made of new particles, which particles are they? Can we find them?

Although the Dark Matter constitutes the majority of the matter in the Universe, there is no suitable candidate in the Standard Model that can play a role of the DM particle. At first sight, neutrinos seem to look promising but actually they cannot constitute more than few percent of Dark Matter. Indeed, assuming that all existing particles and interactions are described by the SM, we can unambiguously calculate the number density of relic neutrinos at the present epoch. If the mass of these particles is too large, the contribution to energy density would be too large as well. This gives an *upper* bound on the mass of the "DM neutrino". On the other hand, the astrophysical observations of dwarf galaxies, which are DM-dominated compact objects, show that if the Dark Matter particle is a fermion, then its mass should exceed several hundred eV (otherwise, the number phase space density of the particles would have to exceed that of a degenerate Fermi gas and violate the Pauli principle to explain the observed mass distributions in these objects) [30, 31]. This gives a *lower* bound. Therefore, cosmological and astrophysical requirements for the properties of SM neutrinos to serve as the DM particle *contradict to each other.*

Moreover, we know now from particle physics experiments that the masses of SM neutrinos can not exceed a few eV. For such small particle masses, the structure formation would proceed in a qualitatively different way, with large objects forming earlier than the small ones, which contradicts observations [27, 32]. The data on the abundances of primordial elements and on the properties of the Cosmic Microwave Background also confirm independently that the contribution of neutrinos to the present-day energy density is very small [20, 33]. Thus we can robustly conclude that the SM by itself does not explain Dark Matter and some new physics is required.

1.2.3 Matter-antimatter asymmetry of the Universe

The third BSM problem that we want to mention is related to the observation that **we live in a world filled almost exclusively by matter, with no significant traces of primordial antimatter**.

Let us go back in time, to when the Universe was hot. At high enough temperatures, particles that constitute the matter were relativistic, and were produced in particle-antiparticle pairs. Therefore, the individual densities of baryons n_B and anti-baryons $\bar{n}_B$ were not conserved, only their asymmetry was conserved, $n_B - \bar{n}_B$. The densities of relativistic particles are comparable to each other, therefore $n_B \sim n_\gamma$ (density of photons).

All pairs later annihilate to the photons and therefore the asymmetry at later times is characterised by the so-called baryon-to-photon ratio. This quantity affects a number of observables and therefore its present-day value is known relatively well [34]:

$$\eta_B = \frac{n_B - \bar{n}_B}{n_\gamma} = (6.047 \pm 0.074) \times 10^{-10}, \tag{1.2}$$

The quantity η_B does not change with time, up to the temperatures of about 100 GeV. This property is called the Baryon Asymmetry of the Universe (BAU).

Although η_B is small, it requires an explanation, since if the theory possesses exact symmetry between particles and anti-particles, η_B would never change during the evolution. In such a theory, the only way to have non-zero η_B would be to postulate it as an initial condition. Indeed, our description of the Universe based on the hot Big-Bang cosmology cannot be extended arbitrary far into the past, not only because for high enough temperatures we do not have observational data, but also because we cannot trust the Standard Model anymore (indeed, for energies which are close to the Planck scale, we do not know what is the correct physical description of the Universe). Therefore, maybe the value of the baryon asymmetry is given by initial conditions?

However, if the flatness of the Universe, the initial spectrum of density perturbations (required for development of the observed large-scale structure) and other observed properties of the Universe are explained by an epoch of rapid accelerated expansion (the model of cosmological inflation [35, 36, 37], that is well motivated by the data and has no compelling alternatives at present [38]) – this scenario becomes very unlikely. Indeed, in the inflationary picture all the densities of all charges, including the baryon asymmetry, would be diluted by a very huge factor like e^{-60}, and at the beginning of the post-inflationary stage, all the initial conditions would be “forgotten” [39]. All subsequent dynamics should be governed by the SM, or we should assume the existence of some new particle physics. Regardless, we need a particle physics mechanism that would explain the change of η_B and, therefore, introduce some asymmetry between particles and antiparticles at a fundamental level. In principle, such a mechanism could exist in the SM (the so-called electro-weak baryogenesis) if the spontaneous breaking of the electroweak symmetry would go through a first-order phase transition, which requires the mass of the Higgs boson below 70 GeV [40, 41, 42]. However, since the time of the Large Electron Positron (LEP) collider experiment, we know the mass of the Higgs boson should above 114GeV [43] (according to the LHC data, the mass is 125GeV [44, 45]). Therefore the electroweak baryogenesis should not take place in the early Universe, and we face a real BSM problem here.

In order to explain the abovementioned observational BSM problems, researchers come up with new theories. These theories, on the one hand, should reproduce the behaviour of the Standard Model, which was confirmed in the numerous past experiments, and on the other hand, provide new particles and interactions that are responsible for the new physics.

1.2.4 Approaches to resolve the BSM problems

“BSM model-building” can be roughly divided into two types: the “top-down” and “bottom-up” approaches. In the top-down approach, one attempts to guess the correct theory, which is based on a new physical principle (among the representative examples are supersymmetric theories, theories with extra dimensions and string theory). To guess the correct fundamental principle one may use as a criterion “naturalness”, by trying to explain certain peculiar properties of the SM (hierarchy problem, strong CP-problem etc), or even try to solve a more fundamental problem, e.g. to build a theory of quantum gravity. Solutions to the observational BSM problems typically appear as possible by-products of the postulated fundamental principle. Sometimes the richness of the top-down models becomes their phenomenological drawback, as it is very challenging to falsify the whole class of models based on the same fundamental principle (like, for example, the whole class of supersymmetric extensions of the SM).

The bottom-up approach concentrates on the solution of the BSM problems, by building a theory, falsifiable with available experimental means. If such a theory is confirmed experimentally, one would then start to explore its structure, such as hidden symmetries underlying small parameters, etc. Since the abovementioned BSM phenomena are apparently unrelated, once we have a theory that explains them all simultaneously, a number of non-trivial independent experimental checks becomes available. *In what follows we will concentrate on the bottom-up approach.*

1.3 Sterile neutrinos and the νMSM model

In the bottom-up approach, an interesting possibility to solve several BSM problems is provided by the ***right-handed*** *neutrino.* We have already noticed above that, in the SM, neutrinos can be only left-handed. However, a more precise statement would be that if we add right-handed neutrinos to the SM, these particles will not interact through electromagnetic, weak or strong forces and, therefore, will not affect the confirmed phenomenology of the Standard Model. These right-handed particles are usually called "sterile" neutrinos, and in this context the usual neutrinos are called "active". More formally, "sterile" means that the fields $N_I(x)$ of right-handed neutrinos are singlets under the $U_Y(1) \times SU_L(2) \times SU_C(3)$ gauge group of the Standard Model, therefore sterile neutrinos are sometimes called singlet neutrinos.

Once we include a right-handed neutrino N to the spectrum of particles, the so-called Yukawa coupling

$$\Delta\mathcal{L}_Y = -F\bar{L}(x)\tilde{H}(x)N(x) + \text{h.c.}, \tag{1.3}$$

between left (L) leptons, right neutrinos and the Higgs field H is possible (we use the same notation as before, $\tilde{H} = i\sigma_2(H^\dagger)^T$). After the spontaneous symmetry breaking, this term has the form of the "Dirac mass" $M_D\bar{\nu}N$.[2] This way, left-handed neutrinos receive mass, which is the same as the mass of the right-handed partner. Here, we have considered for simplicity only one lepton generation and one singlet neutrino, but the numbers of left and right particles can be easily extended so that oscillations between different active flavours may take place. In this scenario, neutrinos are Dirac particles, the masses of sterile neutrinos are the same as the masses of active neutrinos, and are very small according to the observations.

However, neutrinos should not be necessarily Dirac particles. Instead, since right-handed neutrinos are neutral, they can carry no conserved quantum number (like the lepton number), so that the additional term becomes possible,

$$\Delta\mathcal{L}_{\text{Maj}} = -\frac{M_s}{2}\overline{N^c}N + \text{h.c.}, \tag{1.4}$$

the so-called Majorana mass term, where M_s is the Majorana mass of the particle. Since right-handed neutrinos are singlets, the Majorana mass term does not violate the gauge symmetry of the SM, in contrast to the Majorana mass term $m_\nu\overline{\nu^c}\nu$ for left-chiral neutrinos. If we consider singlet neutrinos, which have both the Dirac M_D and Majorana M_M masses, then neither of the flavour eigenstates ν and N has a definite mass. In other words, mass eigenstates N_M, ν_M do not

---

[2] Note that the coupling of neutrinos to the Higgs field in (1.3) is important, since $L(x)$ is a two-component field ($SU_L(2)$-doublet), and it transforms non-trivially under $SU_L(2)$ transformations. Recalling that N does not transform under $SU_L(2)$, one concludes that the simple combination $\bar{L}N$ is not gauge-invariant, so that presence of this term would make the extension of the SM self-inconsistent. On the other hand, the combination $\bar{L}HN$ *is* gauge-invariant.

coincide with the flavour eigenstates. Instead, the two bases are related by a 2×2 unitary transformation, which can be reduced to an orthogonal matrix (by a phase redefinition of the fields $\nu(x)$, $\nu_M(x)$, $N(x)$, and $N_M(x)$),

$$\begin{pmatrix} \nu_M \\ N_M \end{pmatrix} = \begin{pmatrix} \cos\theta & \sin\theta \\ -\sin\theta & \cos\theta \end{pmatrix} \begin{pmatrix} \nu \\ N \end{pmatrix} \tag{1.5}$$

The real-valued parameter θ describes the quantum-mechanical mixing between the flavour and mass eigenbases, and is usually called the *mixing angle*. In what follows, we concentrate on the particular case of small Dirac mass, $M_D \ll M_M$. Then, as a result of diagonalization of the Lagrangian with Dirac and Majorana terms, the mixing angle is found to be

$$\theta = \frac{M_D}{M_s} \ll 1, \tag{1.6}$$

the lighter mass eigenstate ν_M is close to the active flavour eigenstate ν, and it has mass

$$m_\nu \sim \frac{M_D^2}{M_s}. \tag{1.7}$$

The heavier mass eigenstate N_M is close to the sterile flavour eigenstate N, and has mass approximately equal to M_s.

If singlet neutrinos are neutral with respect to the SM gauge group, then how do these particles interact with ordinary matter at all? The interaction is described in Fig. 1.1: although sterile neutrinos do not interact directly, they couple to active neutrinos via the Dirac mass, so that a sterile neutrino can trasform into an active neutrino with probability proportional to the squared mixing angle, θ^2. Therefore, we conclude that sterile neutrinos interact with the effective coupling constant θG_F, where G_F is the Fermi constant.

If we consider energies E much smaller than the Majorana mass, $E \ll M_s$, then the singlet state is not produced as a real particle, and the effective interaction of active neutrinos is described by

$$\mathcal{L}_{\text{mass}} = \frac{F^2}{M_s}(\bar{L}\tilde{H})(H^\dagger L^c), \tag{1.8}$$

which is illustrated at the level of Feynman diagrams in Fig. 1.2. One recognizes in $\mathcal{L}_{\text{mass}}$ the Weinberg operator (1.1), if one identifies Λ with M_s.

By looking at (1.7), we can note two important things. First, for $M_D \ll M_s$, the active neutrino mass m_ν can be arbitrary small, $m_\nu \ll M_D$, for any M_D. This explanation of the smallness of the observed neutrino masses (which are below eV) is usually referred to as the "see-saw" mechanism [46, 47, 48, 49]. Second, in neutrino oscillation experiments we measure two independent combinations of neutrino masses m_i, namely $m_1^2 - m_2^2$ and $m_1^2 - m_3^2$. This means that we need at

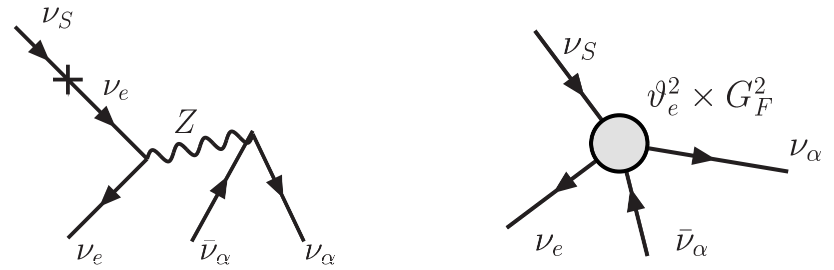

(a) Decay of sterile neutrino $\nu_S \to \nu_e \nu_\alpha \bar{\nu}_\alpha$ through neutral current interactions

(b) Fermi-like interaction with the "effective" Fermi constant $\vartheta_e \times G_F$ for the process in the panel (b).

Figure 1.1: Fermi-like super-weak interactions of sterile neutrino

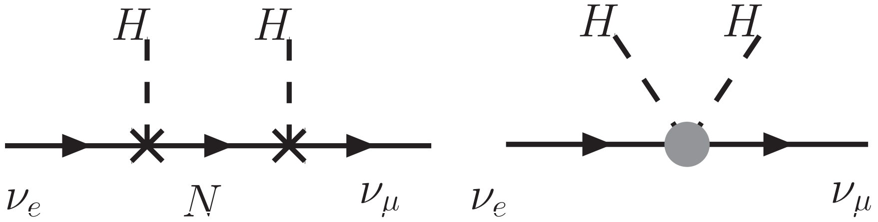

Figure 1.2: Neutrino oscillation $\nu_e \to \nu_\mu$ is mediated by sterile neutrino N (left panel). At low energies, the sterile neutrino line shrinks to a point, so that the local Weinberg operator appears (right panel). In both panels, H is the Higgs field.

least two singlet neutrinos to explain the observations, in which case the lightest active neutrino mass eigenstate is massless [50]. But the absolute value of these neutrino masses is not fixed by the data and if the smallest neutrino mass is different from zero, the minimal number of right-handed neutrinos, needed to explain neutrino flavour oscillations, will be three.

For an arbitrary number of right-handed neutrinos the Lagrangian of the corresponding extension of the SM will be then

$$\mathcal{L} = \mathcal{L}_{\rm SM} + i\bar{N}_I \gamma^\mu \partial_\mu N_I - \left(F_{\alpha I} \bar{L}_\alpha N_I \tilde{H} + \frac{M_I}{2} \overline{N_I^c} N_I + \text{h.c.} \right) . \tag{1.9}$$

Here the sum over the indices of sterile neutrinos I and over the flavour indices α is understood, and $\mathcal{L}_{\rm SM}$ is the Lagrangian of the Standard Model. In the case of three right-handed neutrinos we have equal numbers of right-handed (sterile) and left-handed (active) neutrinos of the SM and the symmetry between left and right fermions is restored, see Fig. 1.3. Moreover, it turns out that this number

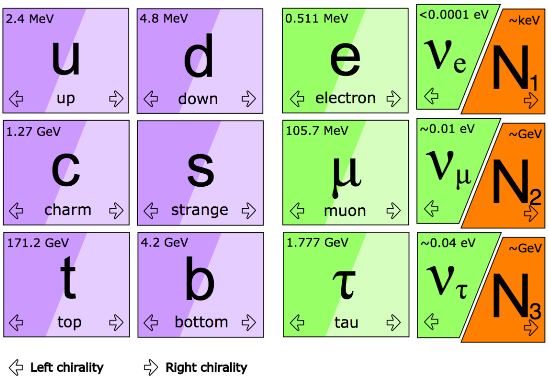

Figure 1.3: The Standard Model extended with three right-handed (sterile) neutrinos, N_1, N_2, and N_3.

is enough to explain all the three abovementioned BSM problems, as we discuss below.

In the case of three sterile neutrinos, the see-saw relation (1.7) is generalized to

$$\hat{m}_\nu = \hat{M}_D \,\mathrm{diag}\left(\frac{1}{M_1}, \frac{1}{M_2}, \frac{1}{M_3}\right) \hat{M}_D^T, \tag{1.10}$$

where $\hat{m}_\nu$ is the 3×3 mass matrix of active neutrinos, $(\hat{M}_D)_{\alpha I} = F_{\alpha I} v$ is the matrix of Dirac masses. According to this formula, the absolute scale of Majorana masses of sterile neutrinos is not fixed. These masses can be as large as 10^{15} GeV, or they can be very small, in principle.

In what follows, we consider a model where there are right-handed (sterile) neutrinos that have masses below the electroweak scale of 100 GeV, so that **no new high-energy scale is added to the Standard Model.** In this case the mixing angles are small and these particles are very hard to observe at accelerators. They do not change the phenomenology of previous experiments and special strategy should be implemented to detect them (see below). **Their role in cosmology, however, can be profound. Indeed, the small probability of interactions can be overcome by the high density of the SM particles in the extreme conditions of the early Universe.**

1.3.1 Sterile neutrinos in the early Universe

To describe the dynamics of sterile neutrinos in the early Universe let us recall that their interaction with the SM matter goes through mixing with active neutrinos. *The properties of active neutrinos are modified (renormalized) in the presence of* *the dense medium of the hot Universe and, therefore, the active-sterile mixing is modified as well.* Indeed, a probe neutrino that propagates through a medium, interacts weakly with all the particles of this medium, and if we average statistically over these interactions, the usual Dirac equation,

$$i\partial_\mu \gamma^\mu \nu(x) = 0 \tag{1.11}$$

which describes neutrinos in vacuum, is modified in presence of medium,

$$(i\partial_\mu \gamma^\mu - \Sigma)\nu(x) = 0. \tag{1.12}$$

The neutrino gets "dressed" by medium, and the effect of dressing is described by the self-energy Σ, which has the form [51]

$$\Sigma = \gamma^0 \left[b \frac{G_F}{M_W^2} p T^4 + c\, G_F (n_L - \bar{n}_L) \right], \tag{1.13}$$

where n_L and $\bar{n}_L$ are the equilibrium densities of leptons and antileptons, respectively. The dimensionless coefficients b and c depend on the particle content of the plasma, and on the neutrino flavour, but regardless both of them are of order 1. Neutrinos with different momenta p get dressed differently, therefore Σ is momentum-dependent.

The presence of self-energy in the modified Dirac equation (1.12) indicates that the dispersion relation of neutrinos in medium is modified,

$$E(p) = p + V, \tag{1.14}$$

where the quantity

$$V = V(p,T) \equiv \gamma^0 \Sigma \tag{1.15}$$

has the meaning of effective potential of the particle in plasma. This potential depends both on temperature and particle momentum. Since the presence of a medium introduces a preferred frame of reference (the one where the plasma is at rest as a whole), the dispersion relation (1.14) no longer has a Lorentz-covariant form. It implies that if we define mass m_ν of neutrino through $m_\nu^2 = E^2 - p^2$, then we find that neutrinos with different momenta have *different* masses.

We define the *effective* mixing angle θ in medium through

$$\hat{H} = \begin{pmatrix} \cos\theta & -\sin\theta \\ \sin\theta & \cos\theta \end{pmatrix} \begin{pmatrix} E_1 & 0 \\ 0 & E_2 \end{pmatrix} \begin{pmatrix} \cos\theta & \sin\theta \\ -\sin\theta & \cos\theta \end{pmatrix}, \tag{1.16}$$

where

$$\hat{H} \equiv \begin{pmatrix} \cos\theta_0 & -\sin\theta_0 \\ \sin\theta_0 & \cos\theta_0 \end{pmatrix} \begin{pmatrix} p & 0 \\ 0 & \sqrt{p^2 + m_N^2} \end{pmatrix} \begin{pmatrix} \cos\theta_0 & \sin\theta_0 \\ -\sin\theta_0 & \cos\theta_0 \end{pmatrix} + \begin{pmatrix} V & 0 \\ 0 & 0 \end{pmatrix} \tag{1.17}$$

is the effective Hamiltonian of active and sterile neutrinos in medium. Here we write the Hamiltonian in the flavour eigenbasis. In other words, θ describes the relation between flavour and mass eigenstates in medium.[3] The first term on the right-hand side of Eq. (1.17) is the same as in vacuum, and tells us that the vacuum mass eigenstates are related to vacuum flavour eigenstates by a rotation with angle θ_0, according to Eq.(1.5) (the subscript 0 indicates here that the mixing angle corresponds to zero temperature). The second term on the right-hand side, however, is the medium correction. This correction is present only for the active flavour eigenstate, since sterile flavour eigenstate does not interact directly via weak interactions.

At finite temperature, the effective mixing angle θ is different from the vacuum mixing angle, and the diagonalization of the effective Hamiltonian shows

$$\theta = \theta(T) \approx \arctan\left[\theta_0 \frac{2\Delta E_{\text{vac}}}{\Delta E_{\text{vac}} + V + \sqrt{(\Delta E_{\text{vac}} + V)^2 + 4\theta_0^2 \Delta E_{\text{vac}}^2}}\right], \quad (1.18)$$

Temperature dependence enters through the potential V (1.15). Here $\Delta E_{\text{vac}} = m_N^2/2p$ is the difference of energies for active and sterile neutrinos in vacuum, for a given common momentum p. At non-zero temperature, however, this difference of energies is modified,

$$\Delta E(p) \equiv E_2(p) - E_1(p) = \sqrt{(\Delta E_{\text{vac}} + V)^2 + 4\theta_0^2 \Delta E_{\text{vac}}^2}. \quad (1.19)$$

Since active neutrinos are in thermal equilibrium at high temperatures, most of them have momentum $p \sim T$. As a consequence, sterile neutrinos have momenta in the same range.

In absence of lepton asymmetry, $n_L - \bar{n}_L = 0$, the mixing angle increases monotonically with lowering the temperature, and reaches the maximal value at zero temperature, $\theta = \theta_0$, see the left panel in Fig. 1.4. Therefore, in this case the mixing angle remains small all the time.

In presence of lepton asymmetry, however, the behaviour of the mixing angle changes. First, the temperature dependence of the mixing angle is non-monotonic anymore, and second, mixing angle can reach large values, $\theta \sim 1$. (See the right panel in Fig. 1.4.) This large value of the mixing happens when $\Delta E_{\text{vac}} + V = 0$, and according to (1.19) it is accompanied by suppression of the energy splitting ΔE. It means that levels of active and sterile neutrinos almost cross each other, so that *resonance* happens.

In order to find the interaction rate Γ_N of sterile neutrinos in medium, one can use the estimate $\Gamma_N \sim n\sigma_N$, where n is the concentration of the SM particles, σ_N is the cross-section of a typical reaction with sterile neutrino, for example $N + \nu \to \nu + \nu$. Concentrations of relativistic particles are $n \sim T^3$, and the cross-section of sterile neutrino is the same as for active neutrino, only the additional

---

[3] In agreement with what was said above about the neutrino mass in medium, by “mass eigenstates” in medium we mean states that have definite energy for a given momentum.

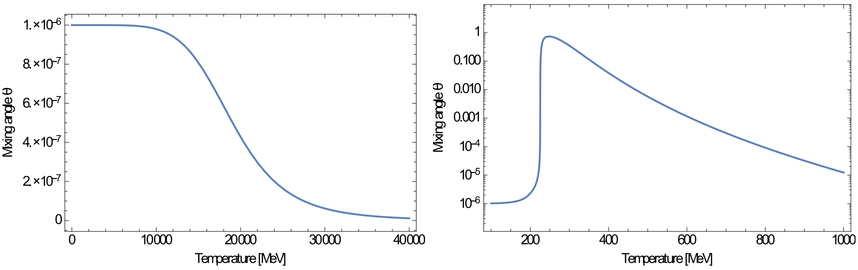

Figure 1.4: Temperature dependence of active-sterile mixing angle. Left panel: $M_s = 1$ GeV, no lepton asymmetry. Right panel: $M_s = 10\,\text{keV}$, the ratio of the lepton number L to the entropy S is $L/S = 10^{-5}$. In both panels, the vacuum mixing angle is $\theta_0 = 10^{-6}$, the neutrino energy is equal to temperature, $E = T$.

suppression factor θ^2 is added, $\sigma_N \sim \theta^2 G_F^2 T^2$. Therefore,

$$\Gamma_N \sim \theta^2(T) G_F^2 T^5. \tag{1.20}$$

If the interaction rate Γ_N is much smaller than the Hubble expansion rate $H(T)$, then singlet neutrinos do not reach thermal equilibrium. In other words, if the Universe expands faster, than the interactions take place, the particles do not have time to come into equilibrium with the rest of the plasma.

From the Friedmann equation $H^2 = 8\pi\rho/3M_{\text{Pl}}^2$, the Hubble rate can be estimated as

$$H(T) \sim \frac{T^2}{M_{\text{Pl}}}. \tag{1.21}$$

Here $M_{\text{Pl}} \approx 1.2 \times 10^{19}$ GeV is the Planck mass, and $\rho \sim T^4$ is the plasma energy density.

If we neglect the temperature dependence (1.18), then at some sufficiently high temperature the interaction rate (1.20) becomes larger than the expansion rate (1.21). However, the temperature dependence of the mixing angle invalidates this conclusion. Instead, the ratio Γ_N/H has a peak at some temperature, as it is illustrated in Fig. 1.5.

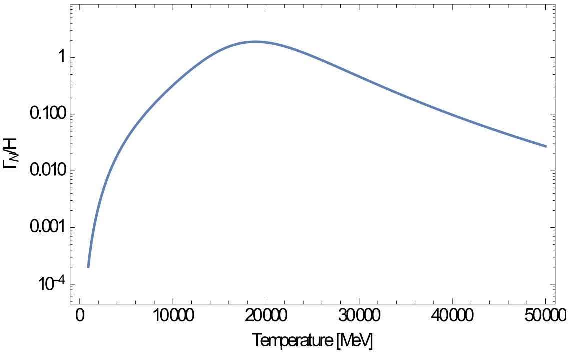

Figure 1.5: Temperature evolution of the ratio Γ_N/H of the sterile neutrino production rate Γ_N to the Hubble expansion rate H. $M_s = 1$ GeV, vacuum mixing angle is $\theta_0 = 10^{-6}$, no lepton asymmetry is present in the Universe. The energy of sterile neutrino is equal to temperature, $E = T$.

The two different scenarios for the evolution of sterile neutrinos in the early Universe are possible.

1. Although the mixing angle is much smaller than 1, the rate of interactions Γ_N can exceed the expansion rate at some temperature, $T = T_+$, and sterile neutrino reaches thermal equilibrium. At smaller temperatures, the interaction rate decreases faster than the expansion rate, so at some point ($T = T_-$) sterile neutrinos fall out of equilibrium.
2. The mixing angle is so small, that thermal equilibrium of N is never reached. In this case, the sterile neutrino number density n_N is smaller than the equibrium value, $n_N < n_{\text{eq}} \sim T^3$, but anyway this density can be significant, especially at the later stages of the Universe evolution, as we will see below.

The ratio Γ_N/H for the first scenario is plotted in Fig. 1.5. For the second scenario, when $\Gamma_N \ll H$ all the time, the density of sterile neutrinos can be estimated very roughly as

$$\frac{n_N}{n_{\text{eq}}} \sim \left(\frac{\Gamma_N}{H}\right)_{\text{Max}} \sim \theta_0^2 M_s M_{\text{Pl}} G_F^{3/2} M_W \simeq \frac{\theta_0^2}{10^{-13}} \frac{M_s}{\text{GeV}} \quad \text{(No lepton asymmetry)} \tag{1.22}$$

in absence of lepton asymmetry. Here we have noticed that the ratio Γ_N/H peaks around the temperature

$$T \sim \left(\frac{M_W^2 M_s^2}{G_F}\right)^{1/6} \simeq 10\,\mathrm{GeV} \times \left(\frac{M_s}{\mathrm{GeV}}\right)^{1/3}, \tag{1.23}$$

where the terms ΔE_{vac} and V in Eq. (1.18) are of the same order.

Here one has to distinguish number density n_N and energy density ρ_N. Even if the number of sterile neutrinos is much smaller than the number of SM particles, $n_N \ll T^3$, it does not mean that they do not contribute to the energy density. Indeed, although sterile neutrinos are produced relativistic, their momenta get smaller with the Hubble expansion, due to the gravitational redshift. It means that if their mass is sufficiently large, these particles can become non-relativistic at some point, and their energy density $\rho_N \sim n_N M_s$ can become comparable to the energy density of SM particles, $\rho_{\mathrm{SM}} \sim T^4$.

For the resonantly produced sterile neutrinos, their density has the same order of magnitude as the density of lepton number,

$$n_N \sim n_L - \bar{n}_L \quad \text{(Large lepton asymmetry)} \tag{1.24}$$

Indeed, sterile neutrinos are produced relativistic, which means that the mass is not important for them. For neutrinos, which are almost massless, the active+sterile lepton number (the SM lepton number plus number of left-helical sterile neutrinos minus number of right-helica sterile neutrinos) is conserved during the oscillations and collisions. The effective resonant production implies then that the significant fraction of SM lepton number was transferred to the "sterile lepton number".

In case when sterile neutrinos do not reach thermal equilibrium, their out-of-equilibrium abundance is different in the two cases:

1. If lepton asymmetry is absent, the effective mixing angle does not exceed its vacuum value θ_0, and the abundance is suppressed by θ_0^2 (non-resonant production).
2. If lepton asymmetry is present, resonant enhancement of the effective mixing angle can happen, the abundance of sterile neutrinos is not suppressed by θ_0^2, and is proportional to lepton asymmetry (resonant production).

As we have noticed above, extensions of the Standard Model should explain all the previous experiments, which were expained by the SM. Similarly, the well-established cosmological phenomena, which were explained by the SM, should not change in these extensions as well. For example, the SM describes very good the so-called Big-Bang Nucleosynthesis (BBN), which is essentially the epoch, when the first light nuclei are formed out of the initial neutrons and protons (see reviews [52, 53, 54]). Theoretical predictions of the SM are in nice agreement with the astrophysical observations of the relic abundances of light nuclei such as ^{2}H, ^{3}He, and ^{4}He [52]. If the Standard Model is extended with sterile neutrinos, this agreement should not be lost.

What is the influence of sterile neutrinos on the BBN? First, presence of sterile neutrinos increases the energy density of plasma, and according to the Friedmann equations, it increases the expansion rate of the Universe. Second, sterile neutrinos introduce deviation from thermal equilibrium, so that spectra of active neutrinos are distorted, the rate of weak reactions is altered, and the moment when neutrons fall out of equilibrium is shifted (this moment is crucial, since it defines the ratio of concentrations of neutrons and protons at the onset of the BBN).

In order not to spoil the agreement between the SM predictions of the Big-Bang Nucleosynthesis and observations, sterile neutrino should be either long-lived and be present in negligible amount in plasma, or to be short-lived, and to decay before the nucleosynthesis starts. If sterile neutrinos describe neutrino oscillations, their mixing angles are large enough so that the scenario with long-lived particles does not take place for them. **The impact on the nucleosynthesis of such sterile neutrinos is discussed in detail in Chapter 3**.

Having discussed the potential importance of sterile neutrino in the early Universe, below we will discuss in detail how this particle can play a role of Dark Matter, and how it can give rise to the Baryon Asymmetry of the Universe.

1.3.2 Sterile neutrino Dark Matter

It is known that sterile neutrino N with mass in the keV region is a viable Dark Matter candidate [55, 56, 57]. Then, this neutrino has to be stable on the cosmological timescales, or equivalently, its lifetime should exceed the age of the Universe. **Therefore, N has a small mixing angle.**

Moreover, if we return to the previous discussion of the dynamics of sterile neutrino in the early Universe, we can conclude that the mixing angle should be small enough for sterile neutrino *not to* reach equilibrium in the early Universe. Indeed, if our DM particle went through the equilibrium period, its number density n_N would be comparable to the number density of photons or ordinary neutrinos or be even larger. Therefore, like for active neutrinos, to give the correct DM mass density, the mass of sterile neutrino with such a number density would have to be $M_s \simeq 10$ eV (see e.g. [33]). Exactly like for ordinary neutrinos, this number would contradict the Pauli principle applied to DM-dominated astrophysical objects (Tremaine-Gunn bound [30]), which implies that $M_s \gtrsim 400$ eV [31]. Therefore, the DM sterile neutrinos should be out of thermal equilibrium at all temperatures and therefore their number density is suppressed as compared to the number density of ordinary neutrinos or photons, and mass can be in keV range (or it can be even larger).

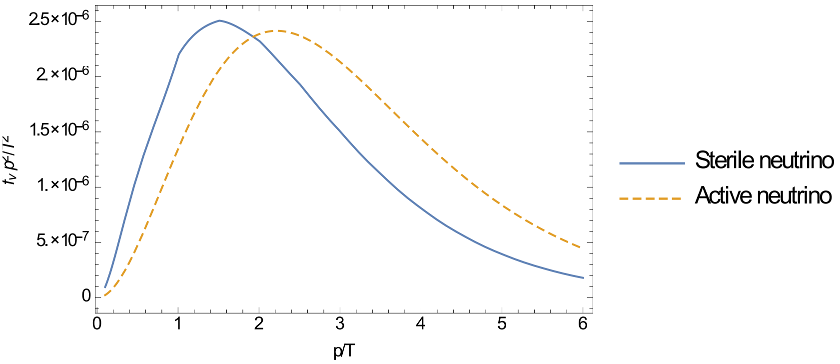

Figure 1.6: Comparison of sterile neutrino distribution function $f_s(p)p^2/T^2$ and the equilibrium Fermi distribution $f_{\rm Fermi}(p)p^2/T^2$ (p is the particle momentum, T is temperature). The mass of sterile neutrino is $M_s = 10\,\text{keV}$, the vacuum mixing angle is $\theta_0 = 10^{-6}$, lepton asymmetry is absent. The absolute scale of the Fermi distribution is reduced so that the two spectra vary in the same range.

According to the estimate (1.23), the dominant fraction of DM particles with keV mass is produced around the temperature $T \sim 100$ MeV. Therefore (in absence of lepton asymmetry, see below) their spectrum has form that is close to the equilibrium Fermi-Dirac distribution with this temperature (that decreases as the Universe expands) [55] (see Fig. 1.6), although the normalisation of spectrum is smaller than 1, as the thermal equilibrium was not established.

As it was already discussed above, a different scenario takes place in presence of lepton asymmetry. In this case a resonant enhancement of the effective mixing angles takes place. This resonant production [56, 58] requires smaller vacuum mixing angles to produce the correct DM abundance for the same particle mass, than the non-resonant production described above. In the resonant case the shape of the spectra of resonantly produced sterile neutrinos can deviate significantly from the Fermi distribution [58, 59] (if the lepton asymmetry is large enough, i.e. comparable with the number of DM particles), see Fig. 1.7. In both resonant and non-resonant cases production of Dark Matter particles happens at temperatures $T \lesssim$ GeV [58, 60, 61].

Of course, here we assume (in the spirit of bottom-up approach) that sterile neutrinos are produced only from their mixing with ordinary neutrinos. If some other new particles exist, apart from sterile neutrinos, there can be more mechanisms of the sterile neutrino DM production. We do not consider these models here.

If DM particle is a sterile neutrino, this particle has so small mixing angle that its contribution to the active neutrino masses is negligible (see e.g. [62]).

The Dark Matter particle can be searched in the cosmic X-ray emission [63, 62]. Although N is stable on cosmological scales, it nevertheless decays. The life time

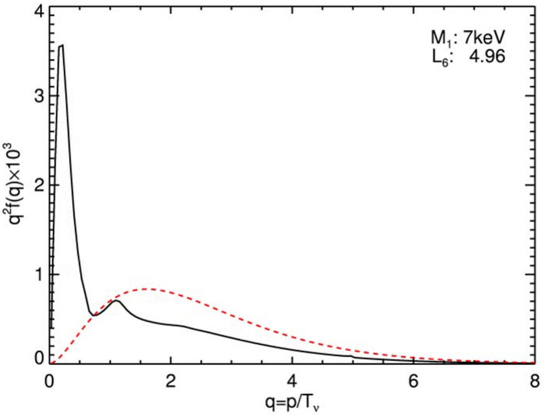

Figure 1.7: Sterile neutrino DM distribution function $f_s(q)q^2$ ($q = p/T$, where p is the particle momentum, T is the temperature). The solid line corresponds to resonantly produced sterile neutrino with initial ratio of lepton asymmetry to entropy equal to 4.5×10^{-5}. The dashed line is the spectrum of non-resonantly produced sterile neutrino. The mass of sterile neutrino in both cases is $M_s = 7\,\text{keV}$.

of this particle is defined by the dominant tree-level three-body decay channel $N \to \nu\nu\bar{\nu}$. There exists also a radiative two-particle decay channel into neutrino and photon, $N \to \nu\gamma$. This decay channel is sub-dominant [64], since it involves a combination of weak and electromagnetic processes at one loop. Although the life time with respect to this decay channel is even longer than for the previous one (and therefore is much longer than the life time of the Universe), the photons emitted in this way can in principle be produced in detectable amounts, due to very large number of DM particles in DM-dominated astrophysical objects. As this is a two-body decay into (almost) massless particles, the energy of the emitted photons is *fixed*, and is equal to one half of the sterile neutrino mass. This property implies a peak in the X-ray spectrum of Dark-Matter dominated regions of space [65, 66]. (The peak is smeared only slightly, by the Doppler effect, caused by the velocity dispersion of Dark Matter particles.)

Recently, an unidentified 3.5 keV line was found in the spectrum of X-rays [67, 68]. The behaviour of this line is consistent with the DM origin: in DM-dominated regions of space, the signal is stronger, in regions with low DM abundance the signal is not found. Therefore, it may be an indication of Dark Matter decay. If this signal comes from decays of DM sterile neutrinos, it should be resonantly produced, implying large enough lepton asymmetry at the temperatures $T \lesssim$ GeV [59, 60, 61].

X-ray bounds show that for both resonant and non-resonant production the mass of DM sterile neutrino should be in the keV range (assuming no other new physics at the relevant temperatures). Therefore, these particles are produced relativistic and have significant *free-streaming length.* This means that the structure formation will be suppressed at the smaller scales as compared to the Cold Dark Matter case (DM particle created non-relativistic). Although sterile neutrino Dark Matter has non-thermal primordial velocity distribution, it is clear that for the smaller masses the effect of free-streaming will be stronger (see Fig. 1.8) and therefore cosmological observations could provide a *lower bound* on Dark matter mass (for each given lepton asymmetry), while X-ray observations provide upper bounds. Free-streaming scales corresponding to DM particles with masses in keV range are such that, for example, CMB observations are not sensitive to them. Cosmological lower bounds require complicated non-linear analysis of structure formation at small scales, subject also to uncertainties related to (largely unknown) baryonic physics. Although promising, this approach requires a lot of additional work to be done. Nevertheless, for the case of the non-resonantly produced sterile neutrino DM, the contradiction between astrophysical X-ray upper bound and cosmological lower bound on DM mass is rather strong (see [69, 70, 71]) and, even with all uncertainties of the method taken into account, this scenario should be considered as strongly disfavoured by the data. For resonantly produced sterile neutrino, however, both cosmological and astrophysical bounds are weaker, leaving enough room for sterile neutrino DM to be produced from interactions with the SM particles [72].

The Dark Matter is made of sterile neutrinos produced from interactions with the SM plasma, the observational bounds imply that they have to be produced resonantly. This requires lepton asymmetry, which is much larger than the baryon asymmetry, to be present at temperatures $T \lesssim$ GeV.

1.3.3 Generation of the baryon asymmetry with sterile neutrinos

It turns out, that sterile neutrinos can not only explain neutrino oscillations and serve as a Dark Matter candidate, but can also generate the Baryon Asymmetry of the Universe, as we discuss below.

In general, to generate the baryon asymmetry, three conditions (the “Sakharov conditions”) should be satisfied [75]

1. Baryon number is not conserved
2. C- and CP-symmetries are violated
3. The Universe must be out of thermal equilibrium during the process of generation of the baryon asymmetry

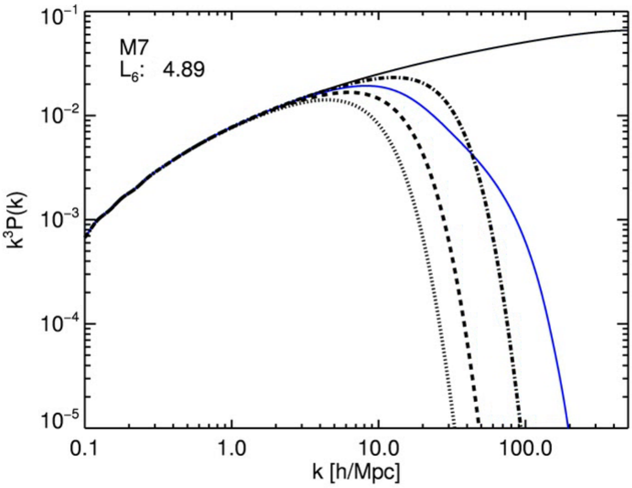

Figure 1.8: Power spectrum $k^3P(k)$ (measure of inhomogeneities of matter distribution in the Universe at different wavenumbers k) for different parameters of sterile neutrino Dark Matter. The monotonically growing solid line corresponds to sterile neutrinos with negligible initial velocity dispersion (Cold Dark Matter), the other solid line – to resonantly produced sterile neutrino with mass $M_s = 7\text{keV}$, and initial ratio of lepton number to entropy equal to 4.4×10^{-5}. The dotted, dashed, and dot-dashed lines correspond to sterile neutrinos with masses $M_s = 1.5\,\text{keV}, 2\,\text{keV}, 3.3\,\text{keV}$ respectively, which have equilibrium (Fermi) form of spectrum. In each case, the abundance of the DM is matched to the observed value.

The first Sakharov condition is satisfied in the Standard Model [76]. Although the baryon number is conserved in elementary collision processes, it is violated by the quantum phenomenon called chiral anomaly [77, 78]

$$\partial_\mu j^\mu_B = \frac{3g^2}{16\pi^2}\mathrm{Tr}\left[F_{\mu\nu}\tilde{F}^{\mu\nu}\right] \tag{1.25}$$

where j^μ_B is the 4-current of baryons (the zeroth component j^0_B is the baryon density), $F_{\mu\nu}$ is the strength tensor of the $SU_L(2)$ gauge field, $\tilde{F}^{\mu\nu} = \epsilon^{\mu\nu\alpha\beta}F_{\alpha\beta}$ is the dual field, g is the $SU_L(2)$ coupling constant, and the trace is taken over the $SU(2)$ indices. Similarly, the lepton current j^μ_L is not conserved due to the same chiral anomaly, such that the combination $B-L$ is preserved, while $B+L$ is *not* preserved [76]. Here $B = \int d^3x j^0_B$ is the baryon number and $L = \int d^3x j^0_L$ is the lepton number. In order to use the chiral anomaly for generation of B, one has to generate first L. Here we want to note that the baryon number violation is better constrained experimentally, than the violation of lepton number [15]. The source

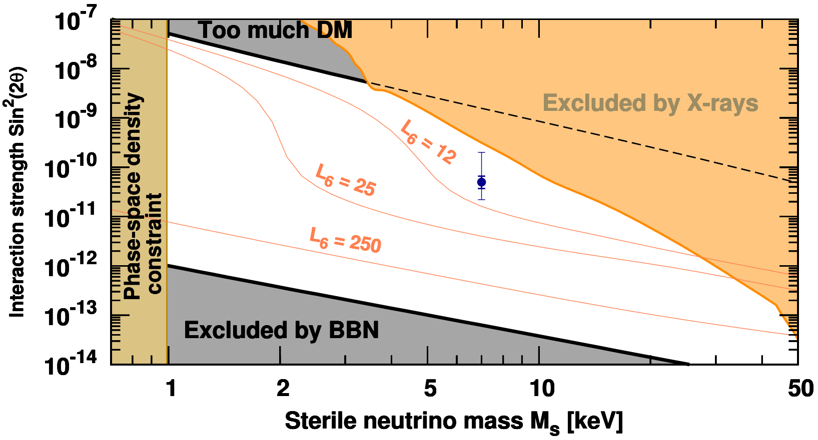

Figure 1.9: Observational constraints on the mixing angle θ of the Dark Matter sterile neutrino. The left shaded region is excluded by the Pauli principle applied to compact DM-dominated objects [30, 31], the upper black line corresponds to the non-resonant production, the right orange corner is excluded by the X-ray observations [63, 62], the region below the lower thick black line is excluded by the Big-Bang Nucleosynthesis [73, 74]. The curves labeled by different values of L_6 correspond to resonant production of the DM at different values of lepton asymmetry ($L_6 \equiv 10^6 L/9S$, where L is the lepton number, S is entropy). The point in the center with error bars corresponds to the observed 3.5keV X-ray signal [67, 68].

of lepton number violation can be provided by Majorana sterile neutrinos.

The integral of the expression $\mathrm{Tr}\,[F_{\mu\nu}\tilde{F}^{\mu\nu}]$ over time and space can take only discrete values n, due to its non-trivial topological properties. Therefore, in order for chiral anomaly to operate and to transform lepton number into baryon number, we need $SU(2)$ field configurations with non-zero n. These configurations exist and are known as sphalerons [79]. They are populated in plasma only at high temperatures, where the electroweak symmetry is unbroken ($T \gtrsim 100\,\mathrm{GeV}$).

Sterile neutrinos lead to successful leptogenesis. If they are much heavier than 100 GeV, according to the see-saw formula (1.7), they have relatively large mixing angles, so that they enter equilibrium at $T \gg 100\,\mathrm{GeV}$. While the Universe cools down, their interaction rate decreases, they fall out of thermal equilibrium ("freeze-out"), and start to decay (the third Sakharov condition). Due to CP-violation, which is present in sterile neutrino sector (the second Sakharov condition), sterile neutrinos interact a bit differently with particles and anti-particles, so that in the decays, the number of lepton and anti-leptons is different, and non-zero lepton number is generated. This is the standard scenario of thermal leptogenesis [80].

It turns out that leptogenesis works for lighter sterile neutrinos, $M_s \ll 100$GeV as well [81, 82]. In this case, however, sterile neutrinos should not come into thermal equilibrium while the electroweak symmetry is unbroken, as we argue below. Instead, they are produced gradually in reactions of the SM particles while the Universe cools down, and due to the CP violation, in reactions with SM particles sterile neutrinos produce different amount of leptons and anti-leptons, so *non-vanishing* lepton numbers are generated. For $M_s \ll 100$ GeV, sterile neutrinos are relativistic, and for relativistic particles, mass does play much role (in particular, whether it is Dirac of Majorana). It means, that the total lepton number is effectively conserved, if one includes into this number the "sterile" lepton number. (The sterile lepton number can be defined as the difference between left-helical sterile neutrinos (particles) and the number of right-helical sterile neutrinos (antiparticles).) This way, the lepton number is *not produced* (as it happened for heavy sterile neutrinos above), but *is distributed* between active and sterile neutrinos. In thermal equilibrium, processes that increase asymmetry in active flavours go with the same speed as the processes that decrease the asymmetry, and the lepton asymmetry is washed out. Therefore, sterile neutrinos should not come into thermal equilibrium during the baryogenesis epoch (third Sakharov condition).

How the lepton numbers in different active flavours are related to each other, depends on the particular pattern of active-sterile mixing. For example, if sterile neutrinos do not couple to electronic flavour, then no asymmetry between electron neutrinos and antineutrinos is produced at high temperatures.

For successful leptogenesis, we need at least two sterile neutrinos. Note that this is the same number, as required for neutrino oscillations. And in what follows, we will implicitly assume that the sterile neutrinos which generate lepton asymmetry, explain neutrino oscillations at the same time. In order to produce the required baryon asymmetry (1.2) with two neutrinos, the CP-violating effect should be enhanced by resonance between the two neutrinos. It requires very small splitting in their masses [82].

An important feature of sphaleron transitions is that they tend to make $B \sim L$ [76]. Therefore at high temperatures, when sphalerons still operate effectively, the small value of baryon asymmetry (1.2) is accompanied by the same small value of lepton asymmetry. However, when temperature decreases below 100 GeV, and baryon number becomes conserved, the generation of lepton asymmetry still takes place, and there is no reason why the value of this asymmetry cannot exceed the value of baryon asymmetry. Production of lepton number, which is much larger than the baryon number, is the specific feature of leptogenesis with relatively light sterile neutrinos (masses below 100 GeV). Leptogenesis takes place until the sterile neutrinos finally reach thermal equilibrium ($T = T_+$). At this moment, lepton asymmetry gets washed away, according to what was said above. Sterile neutrinos spend some time in this equilibrium regime, until their collisions become so rare that thermal equilibrium ceases to hold for them. ("Freeze-out" happens, $T = T_-$.) The subsequent evolution is similar to what happens with very heavy

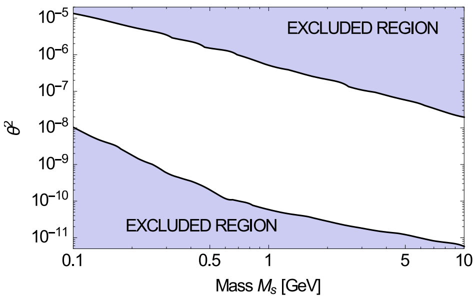

Figure 1.10: Parameter space of two sterile neutrinos which produce the observed Baryon Asymmetry of the Universe [84, 85]. The horizontal axis corresponds to the average mass of sterile neutrinos M_s (the difference between the two masses is much smaller than M_s), the vertical axis corresponds to the average square of the mixing angle, θ^2. The upper filled region is excluded, since for larger mixing angles sterile neutrinos come into thermal equilibrium before the end of baryogenesis and therefore wash out the baryon asymmetry. The lower filled region is excluded, since for smaller mixing angles, sterile neutrinos couple to plasma too weakly, and are not able to produce enough baryon asymmetry.

singlet neutrinos $M_s \gg 100$ GeV: sterile neutrinos freely propagate in plasma, until they start to decay, the numbers of particles and antiparticles produced in these decays are a bit different, so lepton asymmetry is generated again. The successful baryogenesis implies both the lower and the upper bounds on sterile neutrino mass, MeV $\lesssim M_s \lesssim 20$ GeV [81, 82, 83].

The observed value of baryon asymmetry can be generated by sterile neutrinos N_2 and N_3 with masses $M_{2,3}$ in the MeV-GeV range, provided that they have small mass splitting,

$$|M_2 - M_3| \ll M_2 \tag{1.26}$$

The generation of lepton asymmetry by these particles continues at temperatures below 100GeV, when the baryon asymmetry is no longer generated. This way lepton asymmetry can become much larger than the baryon asymmetry. If N_1 does not describe the Dark Matter, this particle can significantly contribute to neutrino oscillations via the see-saw mechanism, and can influence the baryogenesis. In this case, successful baryogenesis does not require smallness of the mass splitting [86], and the lightest active neutrino mass eigenstate does not have to be massless.

1.3.4 The Neutrino Minimal Standard Model

Since the mixing angle of the DM sterile neutrino N_1 is small, it does not contribute significantly to the neutrino masses via the see-saw mechanism. Therefore, in order to explain neutrino oscillations,we need at least another two sterile neutrinos, N_2 and N_3, which can simultaneously give rise to the observed baryon asymmetry. **The resulting number of right-handed neutrinos is three.** If we choose masses of sterile neutrinos below 100GeV, we get the model which is called **the Neutrino Minimal Standard model (νMSM)** [50, 82] (for a recent review, see [62]). In this model, the lightest active neutrino mass eigenstate is massless.

Although we have experimental constraints on different corners of parameter space of the νMSM, there still exists large open window. Here we want to note, that apart from the three Majorana masses M_1, M_2, M_3, there are 15 physically observable parameters in the Yukawa matrix $F_{\alpha I}$. In total, the model is characterized by 18 parameters [50].

If we add to the νMSM non-minimal coupling of the Higgs field to gravity, we can provide an inflationary model, which explains very well the cosmological observations [87, 88]. This way, the history of the Universe can be described up to the very early stages (Planck scales).

Having this consistent theoretical framework, we can no longer consider different phenomena independently. For example, one cannot just say that the lepton asymmetry neeeded for resonant production of Dark-Matter particles, is some given external quantity. As we have noticed above, the value of the lepton asymmetry is controlled by the properties of N_2 and N_3, so one has to consider the interplay between the properties of the light and heavy singlets consistently [85, 84].

If the large lepton asymmetry, which is needed for the resonant production of DM particles, is generated after the freeze-out of $N_{2,3}$ ($T < T_-$), we need such a small value of the mass splitting $|M_2 - M_3|$, that it becomes sensitive to radiative (loop) corrections. In order to get this small number, a fine-tuning of the νMSM parameters should be done, which makes the model “unnatural” [89]. On the other hand, if the lepton asymmetry is produced at higher temperatures ($T > T_+$), then according to the discussion in Sec. 1.3.3, singlet neutrinos come to equilibrium, and the lepton asymmetry is expected to be washed out.

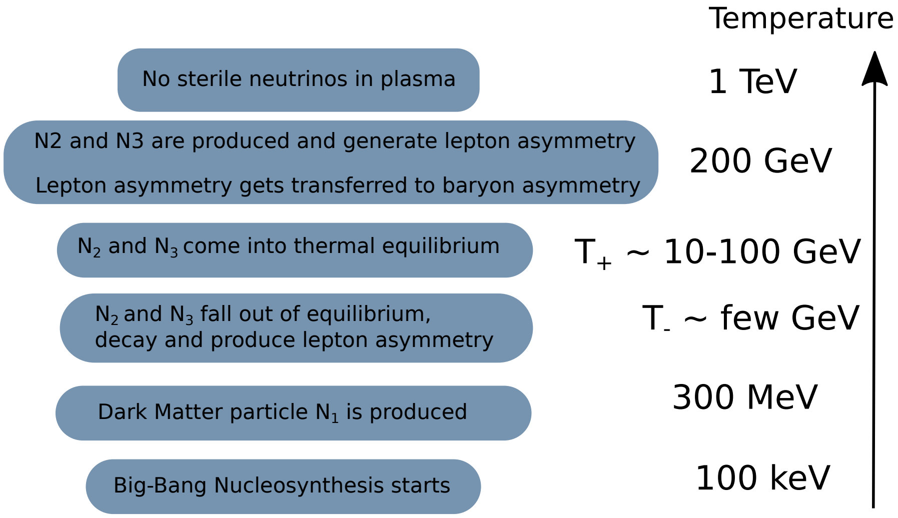

Figure 1.11: The timeline of the processes in the early Universe in the νMSM model.

The νMSM is a testable model, which is constrained by a set of independent cosmological and astrophysical observations, however the window of parameters of this model still remains open. The systematic account of the observational constraints, which is not finished at the present moment, will reduce the parameter space. For example, in order to satisfy the constraints on the DM, $N_{2,3}$ should not only produce the observed baryon asymmetry, but to produce lepton asymmetry, which is much larger than this asymmetry.

It is problematic to produce lepton asymmetry after sterile neutrinos have frozen out ($T < T_-$), while it is much easier to produce the asymmetry at higher temperatures, where sterile neutrinos are still out of thermal equilirium ($T > T_+$). However, in the intermediate region, $T_- < T < T_+$, sterile neutrinos come into thermal equilibrium, and how does the lepton asymmetry evolve here is an open question. Below, we consider an *additional* effect, which is important for the description of lepton asymmetry at these intermediate temperatures.

The timeline of the processes in the early Universe in the νMSM model is plotted in Fig. 1.11.

1.3.5 Lepton asymmetry and magnetic fields

Due to the parity-violating nature of the interactions of SM fermions with electroweak gauge bosons (W, Z and photons), interactions of sterile neutrinos with left and right SM charged fermions are different. Therefore, left and right particles are produced in different amounts during the leptogenesis. Namely, only neutrinos interact with sterile neutrinos. Fast interactions with $W^\pm$ bosons equilibrate the number density of neutrinos and charged leptons (electrons, muon, tau leptons). However, all the gauge interactions respect chirality, and therefore do not change the asymmetries in sectors of left and right particles. Nevertheless, a disbalance between these two sectors gets relaxed to zero since all the charged particles are massive, therefore the numbers of left and right particles are not conserved individually. Namely, there exist collision processes (*chirality-flipping processes*), in which left particle can transform into right one. An example of such a process is Compton scattering, $e_\mathrm{L}\gamma \to e_\mathrm{R}\gamma$, where e_L and e_R are left and right electrons, respectively, and γ is a photon. However, these chirality-flipping processes are relatively slow, chirality-flipping rate Γ_flip is suppressed with respect to the rate of ordinary collisions (*chirality-preserving rate*) $\Gamma_\textsc{lte}$ as m^2/T^2, where m is the fermion mass. Therefore, two different timescales appear in the problem.[4]

The first timescale, $\sim \Gamma^{-1}_\textsc{lte}$, corresponds to the time when partial equilibrium is established in the left and right sector of the theory *separately*, bringing the momentum distribution in each of the sectors to the Fermi-Dirac form:

$$f_\mathrm{L}(\boldsymbol{p}) = \frac{1}{\exp\left(\frac{E_{\boldsymbol{p}}-\mu_\mathrm{L}}{T}\right)+1}, \quad f_\mathrm{R}(\boldsymbol{p}) = \frac{1}{\exp\left(\frac{E_{\boldsymbol{p}}-\mu_\mathrm{R}}{T}\right)+1}, \tag{1.27}$$

where the chemical potentials μ_L and μ_R of these distributions are *independent*, so that the axial chemical potential is non-vanishing,

$$\mu_5 \equiv \mu_\mathrm{L} - \mu_\mathrm{R} \neq 0 \tag{1.28}$$

The second timescale, $\Gamma^{-1}_\mathrm{flip} \gg \Gamma^{-1}_\textsc{lte}$, is much longer than the first one, and corresponds to the time when particles reach equilibrium *between* left and right sectors, due to their mass term and due to the residual Higgs boson decays, $H \to e_\mathrm{L} + \bar{e}_\mathrm{R}$, so that at these times *left and right particles are described by the Fermi-Dirac distribution with a common chemical potential*, $\mu = (\mu_\mathrm{L} + \mu_\mathrm{R})/2$, corresponding to the conserved fermion number.

In other words, fermions spend some time with chiral asymmetry, while having equilibrium spectra (1.27). The chiral imbalance in the plasma of charged particles has drastic consequences for its evolution.

1.3.6 Electric current along the magnetic field

In order to demonstrate how does the chiral imbalance affect the system of charged particles, we will use the quantum mechanical description, originally presented in the pioneering work [90]. Namely, we consider the system of charged fermions (massless for simplicity) in the uniform magnetic field, pointing along the z axis.

---

[4] This is of course a simplification. Below we discuss the simplest case when only electrons, neutrinos and sterile neutrinos are present in the plasma, to avoid discussing the whole hierarchy of times, related to different particles, leptons vs. quarks, etc.

Particles occupy the so-called Landau levels. The energies of these levels are characterized by one discrete integer number $n \geq 0$ and *one* continuous number – momentum p_z along the direction of the field,

$$\varepsilon_n(p_z) = \sqrt{p_z^2 + 2|eB|n}, \qquad n = 0, 1, 2 \ldots \tag{1.29}$$

The level with $n = 0$ (*lowest Landau level*) is different from $n > 0$ levels. The motion of particles is that of *free one-dimensional massless fermions* with $\varepsilon_0(p_z) = \pm|p_z|$ with *their spin always pointing opposite to the direction of the magnetic field*. Therefore the particles with $p_z > 0$ have negative projection of spin onto momentum (so called *left-chiral* particles) and the particles with $p_z < 0$ have positive projection of the spin onto momentum (right-chiral particles).[5] The allowed range of p_z is different for $n = 0$ and $n > 0$, namely

$$-\infty < p_z < \infty \quad (n \neq 0, \quad \text{both chiralities}) \tag{1.30}$$

$$0 \leq p_z < \infty \quad (n = 0, \quad \text{left chirality}) \tag{1.31}$$

$$-\infty \leq p_z \leq 0 \quad (n = 0, \quad \text{right chirality}). \tag{1.32}$$

(these ranges hold for both particles and anti-particles.)

In the vacuum (at zero temperature and zero chemical potentials) all the states with $\varepsilon_n(p_z) < 0$ are filled (the *Dirac sea*) while all the states with $\varepsilon_n(p_z) > 0$ are empty. In thermal equilibrium, the distribution functions are characterized by chiral Fermi distributions (1.27) with $E_{\boldsymbol{p}} = \varepsilon_n(p_z)$, different for left and right particles.

Given the distribution functions, the electric current density can be calculated by the statistical formula

$$\begin{aligned}\boldsymbol{j} = e\frac{|e\boldsymbol{B}|}{2\pi}\left[\int\limits_0^\infty \frac{dp^z}{2\pi}\,\psi_{p^z}\boldsymbol{\gamma}\psi_{p^z} f_{\mathrm{L}}(p^z) + \int\limits_{-\infty}^0 \frac{dp^z}{2\pi}\,\bar{\psi}_{p^z}\boldsymbol{\gamma}\psi_{p^z} f_{\mathrm{R}}(p^z)\right] + \text{anti-particles}+ \\ + \text{sum over Landau levels with } n > 0\end{aligned} \tag{1.33}$$

(where ψ_{p^z} are the eigen functions of the Dirac equation on the lowest Landau level, and the factor $|eB|/2\pi$ is the number of states with given momentum p^z, per two-dimensional area perpendicular to the direction of the magnetic field). The sum over the higher Landau levels does not contribute to the current and therefore only the first line in (1.33) gives non-zero contribution:[6]

---

[5] Here, for definiteness, we have chosen $eB < 0$, and this choice will be used in what follows. If the sign of eB is opposite, then the directions of propagation along z are flipped: the left-chiral states have then $p_z < 0$, the right-chiral states have $p_z > 0$.

[6] We use **bold** notations for 3-dimensional vectors, $\boldsymbol{x}$, $\boldsymbol{A}$. Their components are denoted with Latin indices i. 4-dimensional vectors are denoted by p, q etc and Greek indices run from $0 \ldots 3$.

$$\boldsymbol{j} = -\frac{e^2}{4\pi^2}(\mu_{\rm L} - \mu_{\rm R})\boldsymbol{B} \tag{1.34}$$

This current, flowing along the direction of the magnetic field and proportional to the chiral imbalance, is known as *chiral magnetic current* or *chiral magnetic effect* (CME).

1.3.7 Chiral Magnetic Effect

In the field-theoretical approach, the existence of the Chiral Magnetic Current (1.34) signals a presence of the *parity-odd part* of the low-energy effective action (free energy) of the gauge fields,

$$\mathcal{F}[\boldsymbol{A}] = \frac{1}{2}\int d^3\boldsymbol{q}\, A^i(-\boldsymbol{q})\Pi^{ij}(\boldsymbol{q})A^j(\boldsymbol{q}) \tag{1.35}$$

where the parity-odd part of the polarization operator Π^{ij} is fixed by the gauge and rotational invariance to be of the form

$$\Pi_2^{ij}(\boldsymbol{q}) = -i\epsilon^{ijk}q^k\Pi_2(\boldsymbol{q}^2) \tag{1.36}$$

If $\Pi_2(0) \equiv \Pi_{\rm CS} \neq 0$, then a parity-odd *Chern-Simons term*,

$$\mathcal{F}_{\rm CS}[\boldsymbol{A}] = \Pi_{\rm CS}\int d^3\boldsymbol{x}\, \boldsymbol{A}\cdot\boldsymbol{B}, \tag{1.37}$$

is a part of the free energy (1.35). The current due to the field $\boldsymbol{A}(\boldsymbol{q})$ is given of course as

$$\langle j^i(\boldsymbol{q})\rangle = \frac{\delta\mathcal{F}[\boldsymbol{A}]}{\delta\boldsymbol{A}} = \Pi^{ij}A^j(\boldsymbol{q}) \tag{1.38}$$

The non-zero $\Pi_{\rm CS}$ leads to the current

$$\boldsymbol{j} = \Pi_{\rm CS}\nabla\times\boldsymbol{A} \tag{1.39}$$

which is just the current (1.34) after the identification

$$\Pi_{\rm CS} = -\frac{e^2}{4\pi^2}(\mu_{\rm L} - \mu_{\rm R}) \tag{1.40}$$

The Chern-Simons term has less derivatives than the usual kinetic term $\int d^3x\frac{\boldsymbol{B}^2}{2} = -\int d^3q\frac{(\boldsymbol{q}\times\boldsymbol{A})^2}{2}$ and is therefore more relevant for the infrared physics (i.e., when the wavenumbers $\boldsymbol{q}$ are very small). However, the Chern-Simons term (1.37) is no positive definite, since it involves the odd (first) power of derivative. As a result, the effective action for the electromagnetic fields in the medium with chiral imbalance is unbounded from below for sufficiently small $|\boldsymbol{q}|$ and we can expect the development of instability for $\boldsymbol{A}(\boldsymbol{q})$. And indeed, the Maxwell equations with the current (1.34) are unstable against generation of gauge fields with $|\boldsymbol{q}| \ll \Pi_{\rm CS}$ [91, 92, 93, 94].

1.3.8 Chiral anomaly and dynamics of chiral imbalance

Not only the presence of chiral imbalance changes the dynamics of electromagnetic fields, but also the electromagnetic fields themselves affect the change in time of the chiral chemical potential. This coupling is the consequence of the phenomenon, called quantum anomaly, which was mentioned in context of baryon asymmetry and sphaleron transitions in Sec. 1.3.3. The phenomenon of chiral (or axial) anomaly was known for many decades [77, 78], which is basically the non-conservation of axial fermionic charge $j^{\mu 5} = \langle \bar{\psi}\gamma^\mu\gamma^5\psi\rangle$ in presence of strong electric $\boldsymbol{E}$ and magnetic $\boldsymbol{B}$ fields,

$$\partial_\mu j^{\mu 5} = -\partial_\mu j^\mu_{\rm L} + \partial_\mu j^\mu_{\rm R} = \frac{e^2}{2\pi^2}\boldsymbol{E}\cdot\boldsymbol{B}. \tag{1.41}$$

Here $j^\mu_{\rm L}$ is the electric current density of left-chiral particles, $j^\mu_{\rm R}$ is the contribution of their right-chiral counterparts. Since the magnetic field is unstable, it becomes time-dependent, which induces the electric field, according to the Faraday law, $\boldsymbol{\nabla}\times\boldsymbol{E} = -\partial_0\boldsymbol{B}$. In presence of both electric and magnetic fields, the chiral anomaly starts to operate. Although separately the left- and right-chiral charges are not conserved, their sum is conserved,

$$\partial_\mu(j^\mu_{\rm L} + j^\mu_{\rm R}) = 0. \tag{1.42}$$

This latter requirement is crucial for self-consistency of the theory, otherwise the gauge invariance of the theory is lost. (At the same time, we do not associate the axial current $j^{\mu 5}$ with any kind of gauge symmetry, so the non-conservation of this latter current does not spoil the theory).

As a result of chiral anomaly, the left and right charges get changed, while the combinations

$$\tilde{Q}_{\rm L} = \int d^3x \left(j^0_{\rm L} - \frac{e^2}{4\pi^2}\boldsymbol{A}\boldsymbol{B}\right) \tag{1.43}$$

$$\tilde{Q}_{\rm R} = \int d^3x \left(j^0_{\rm R} + \frac{e^2}{4\pi^2}\boldsymbol{A}\boldsymbol{B}\right) \tag{1.44}$$

are preserved with time. Therefore, it is natural to call these two combinations as generalized chiral charges. One may check, that at zero temperature, the conservation of the generalized charges leads to a *reduction* of the energy splitting $\mu_{\rm L} - \mu_{\rm R}$ between the two Fermi levels $\varepsilon_p = \mu_{\rm L}$ and $\varepsilon_p = \mu_{\rm R}$, with time, provided that the Chern-Simons contribution to the energy density (1.37) is negative. In other words, magnetic fields get produced by "absorbing" the fermionic disbalance, and in the asymptotic equilibrium state, one expects that the Fermi levels for different chiralities become indistinguishable.

Inclusion of temperature does not change qualitatively the picture above, since the form of the electric current (1.34) is independent of the temperature, and is applicable at all temperatures. The system of hydrodynamic equations is

$$\nabla \boldsymbol{E} = \rho, \quad \nabla \boldsymbol{B} = 0, \tag{1.45}$$

$$\nabla \times \boldsymbol{E} = -\frac{\partial \boldsymbol{B}}{\partial t}, \quad \nabla \times \boldsymbol{B} = -\frac{e^2}{4\pi^2}(\mu_{\mathrm{L}} - \mu_{\mathrm{R}})\boldsymbol{B} + \sigma \boldsymbol{E} + \frac{\partial \boldsymbol{E}}{\partial t}, \tag{1.46}$$

$$\frac{\partial(\mu_{\mathrm{L}} - \mu_{\mathrm{R}})}{\partial t} = -\frac{3e^2}{\pi T^2}\boldsymbol{E}\cdot\boldsymbol{B} - \Gamma_{\mathrm{flip}}(\mu_{\mathrm{L}} - \mu_{\mathrm{R}}). \tag{1.47}$$

which are the Maxwell equations together with the Adler-Bell-Jackiw equation (1.41), where in the last one, the axial current is rewritten through chemical potentials. Note the inclusion of the Ohmic current $\sigma\boldsymbol{E}$, where σ is the conductivity of plasma. In what follows, we consider an electrically neutral plasma, so that the charge density ρ vanishes, $\rho = 0$. Another important simplification is that we consider relatively slow evolution of the system, so that the displacement current $\partial\boldsymbol{E}/\partial t$ can be neglected, as compared to the Ohmic current. One notes, that in the Adler-Bell-Jackiw equation, we have added contribution $-\Gamma_{\mathrm{flip}}(\mu_{\mathrm{L}} - \mu_{\mathrm{R}})$, which describes the change of chirality due to particle collisions (the abovementioned chirality-flipping processes), and this tern is not related directly to chiral anomaly. Γ_f has the sense of the chirality-flipping rate (number of chirality-flipping reactions for a given particle, per unit time).

Going to Fourier space with respect to spatial coodinate $\boldsymbol{x}$, we find that the electric and magnetic fields are transversal, $\boldsymbol{q}\cdot\boldsymbol{E} = \boldsymbol{q}\cdot\boldsymbol{B} = 0$. Excluding the electric field, we get

$$\frac{\partial \boldsymbol{B}}{\partial t} = -\frac{1}{\sigma}(q^2\boldsymbol{B} + i\frac{e^2}{4\pi^2}\mu_5\, \boldsymbol{q}\times\boldsymbol{B}). \tag{1.48}$$

Here the shorthand notation $\mu_5 = \mu_{\mathrm{L}} - \mu_{\mathrm{R}}$ for the chiral disbalance was introduced. The term with μ_5 in the right-hand side involves first power of wavenumber q, while the other term in the right-hand side involves the second power of q. The wavenumbers where the term with μ_5 becomes larger than the term with q^2, are

$$q \ll \frac{e^2}{4\pi^2}\mu_5 \tag{1.49}$$

In this infrared region, the term with μ_5 dominates the dynamics of the magnetic field. On the other hand, the sign of this term depends on the helicity of the magnetic field (whether it is left- or right-helical), therefore one of the helicities grows exponentially with time [92], which is the sign of the instability, which was mentioned above.

Having in mind the setup of very early Universe, the chirality-flipping rate is known to be larger than the Hubble expansion rate

$$H \sim \frac{T^2}{M_{\text{pl}}}, \tag{1.50}$$

at temperatures $T \lesssim 80$ TeV [95]. (Here $M_{\text{pl}} \sim 10^{19}$ GeV is the Planck mass.) This result means, that chirality-flipping reactions are very active at these temperatures, and the anomalous instability process does not take place: instead of producing magnetic fields, the chiral disbalance is washed away by collision processes.

Therefore, we see that magnetic field affects the evolution of the chiral asymmetry $\mu_{\text{L}} - \mu_{\text{R}}$, and these two quantities get coupled. Considered separately, both chiral asymmetry (destroyed by chirality flips) and magnetic fields (destroyed by magnetic diffusion) would disappear from the plasma relatively fast. The picture changes, however, if their coupled evolution is considered.

It was shown recently [96, 97], that the evolution of this coupled system is non-trivial, and large chiral asymmetry together with magnetic fields that are triggered by this asymmetry may survive as long as plasma has charged fermions which are still relativistic. Recalling that the lightest charged fermion is electron, and that it has mass 0.5 MeV, magnetic fields can survive up to temperatures of few MeV.

Moreover, weak interaction violates parity symmetry and therefore the effective properties of the left and right electrons in dense medium are not the same. It was therefore argued in [98], that even if $\mu_{\text{L}} = \mu_{\text{R}}$ (or if the chiral asymmetry in the initial state of the system is small), in the presence of *lepton asymmetry* weak interactions can trigger Chiral Magnetic Effect. This would mean that even the equilibrium state of the SM plasma at high temperatures should be populated by magnetic fields.

Although lepton asymmetry disappears from the plasma once sterile neutrinos enter thermal equilibrium, if strong helical magnetic fields are generated as a by-product of this lepton asymmetry, there is no reason for these magnetic fields to disappear when sterile neutrinos are in thermal equilibrium. Then, once sterile neutrinos are out of equilibrium again, the same CME and chiral asymmetry that accompany helical magnetic fields would quickly regenerate effective lepton asymmetry in the plasma.

Lepton and chiral asymmetries are coupled to magnetic fields. In order to make a reliable prediction of the lepton asymmetry evolution in the temperature range $T_- < T < T_+$ in the νMSM (which is important for determination of the DM abundance), one has to understand the coupled dynamics of these degrees of freedom. The steps towards systematic exploration of this question are made in Chapters 4 and 5.

1.3.9 Accelerator searches of sterile neutrinos

Sterile neutrinos can be searched at particle accelerators [99]. A number of accelerator searches was carried out in the past and are planned for the future. The main strategy of these searches is not to increase the energies of the colliding particles, as it takes place in the LHC collider, where the center-of-mass energy is of order of 10TeV (*high-energy frontier*), but to reach high statistics of the rare events (*high-intensity frontier*).

Cosmological bounds play here important role, since they reduce the wide window of possible parameters of the model for such terrestial searches. The νMSM can be regarded here as a benchmark bottom-up model, which illustrates how well can we explore the parameter space using methods of particle physics, cosmology and astrophysics.

The systematic account of cosmological and accelerator constraints of the νMSM is not finished at the present moment, and the current thesis attempts to make a step in this direction.

The past experiments are reviewed in Chapter 2. Here we want to describe one of the most promising *future* experiments to search for the two heavier νMSM neutrinos, the SHiP experiment (Search for Hidden Particles) [100, 101, 102] (the website of the collaboration is `http://ship.web.cern.ch/ship/`). This experiment is a proposed general-purpose fixed target facility at the CERN SPS (Super Proton Synchrotron).

The setup of the SHiP experiment is plotted in Fig. 1.12. The incoming flux of protons with energy 400GeV from the SPS accelerator hits the dense fixed target. As a result of strong interactions, a flux of secondary hadrons (pions, kaons, D-mesons) is produced, and these unstable secondary particles decay into charged leptons and neutrinos, where in addition of active neutrinos, a small admixture of sterile neutrinos appears. The thick wall of absorbing material behind the target ensures that no charged particles pass through it. Next to the wall, the large decay volume is placed, where the decays of new unstable neutral particles can be detected. In this scheme, sterile neutrinos are produced in decays of D-mesons, and can be detected in different two- and three-body decay channels like $N \to \pi^+ e^-$ and $N \to \nu e^+ e^-$.

In the SHiP experiment the center-of-mass energy of the colliding particles (which are the proton from SPS and a proton of the target nucleus) is just several

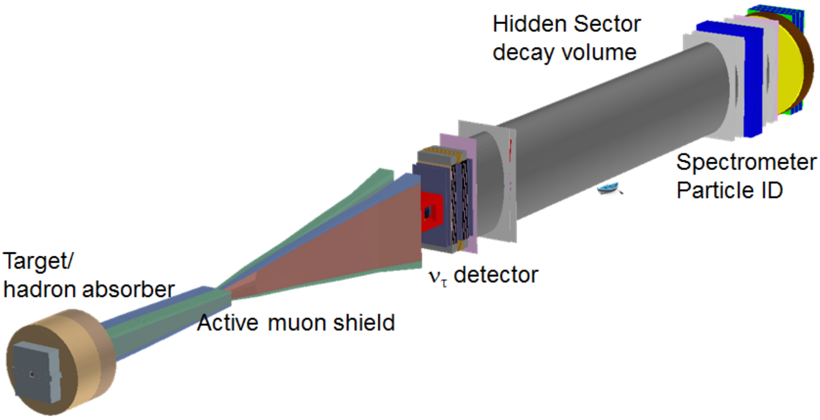

Figure 1.12: The setup of the SHiP experiment [102]. The incident proton beam from the SPS accelerator hits the target, the charged particles are stopped in the active muon shield, while the unstable neutral particles reach the decay volume, where they decay.

tenths of GeV. However, the expected number of protons, which hit the target in this experiment during the 5 years of running, is of order of 10^{20}, which is a tremendous number. This way, the high-intensity frontier is reached.

The mass of the D-meson is approximately 2 GeV, therefore SHiP is not sensitive to sterile neutrinos heavier than 2 GeV. In order to probe the range of larger masses, one can study the decays of heavier mesons [86], B-mesons, which have mass around 5 GeV and are produced in large quantities in experiments like LHCb and Belle.

For $M_s > 5$ GeV, searches at high-energy frontier experiments become more perspective. An example of the planned experiment is FCC-ee [103], which is an electron-positron collider. At this experiment, a large amount of real Z bosons are produced (up to 10^{13} in a few years), which can decay into sterile neutrino.

1.4 This thesis

1.4.1 Chapter 2

In Chapter 2, we study the pattern of the mixings between the Standard Model (active) neutrinos and their right-chiral (sterile) counterparts, which give rise to active neutrino masses via the see-saw mechanism. The bounds on these mixings are derived by combining neutrino oscillation data and results of direct accelerator searches. We reinterpret the results of searches for sterile neutrinos by the PS191 and CHARM experiments, considering not only charged current but also neutral current-mediated decays, as applicable in the case of the νMSM. The resulting *lower bounds* on sterile neutrino lifetime are up to an order of magnitude *stronger* than previously discussed in the literature. We demonstrate that the mixing of sterile neutrinos with any given active flavour can be significantly suppressed, as compared to the mixings with two remaining flavours.

1.4.2 Chapter 3

In Chapter 3, we analyze the influence of sterile neutrinos on the Big-Bang Nucleosynthesis, in particular the primordial abundances of Helium-4 and Deuterium. We solve explicitly the set of kinetic equations (Boltzmann equations) for all particle species, which are driven out of thermal equilibrium by presence of sterile neutrinos, and we take into account neutrino flavour oscillations. We demonstrate that the nuclear abundances are sensitive *mostly* to the sterile neutrino lifetime and only weakly to the way how the active-sterile mixing is distributed between flavours. The decays of sterile neutrinos also perturb the spectra of (decoupled) active neutrinos and heats photons, changing the ratio of neutrino to photon energy density, that can be interpreted as extra neutrino species at later epochs. We derive upper bounds on the lifetime of sterile neutrinos based on both astrophysical and cosmological measurements of Helium-4 and Deuterium. Combination of these results with the lower bound on the lifetime from Chapter 2 rules out the possibility that two sterile neutrinos with the masses between 10 MeV and the pion mass are solely responsible for neutrino flavour oscillations.

1.4.3 Chapter 4

In the Chapter 4, we are interested in the dynamics of primordial plasma after the baryogenesis and long before the primordial nucleosynthesis. As we have argued before, the leptogenesis in the νMSM still takes place at these intermediate temperatures, and the chiral asymmetry is produced as a by-product. Therefore, the Chiral Magnetic Effect may become important, and trigger the growth of magnetic fields. The scale of coherence of the magnetic fields, however, is very large. On the other hand, we know that charged particles, which are the key ingridient for the Chiral Magnetic Effect, are massive, and their mass m is larger than the inverse lengthscale, q, of the magnetic field. However, in the literature the fermion mass is usually neglected, which corresponds to the opposite limit, $q \gg m$. As a result, the calculation of the current is made for massless fermions, two different chiralities of which are in thermal equilibrium with its own chemical potential, either μ_{L} or μ_{R} (Note that we have considered this approximation in the actual derivation of the Eq. (1.34).) However, strictly speaking, massive fermions do not have a definite chirality anymore, and are not in the state of thermal equilibrium, due to chirality-flipping processes, so the calculation of the current is not straightforward. In order to overcome this difficulty, we consider two systems. In the first one, we consider a definite ensemble of quantum-mechanical states, which corresponds to the (local) thermal equilibrium on the one hand, and is characterized by chiral asymmetry, on the other hand. In the second system, the chiral asymmetry is introduced at the level of the particle dispersion relation, by introducing axial self-energy of the form (4.21). Therefore, the asymmetry is expected to be present in the state of thermal equilibrium, which allows application of the standard equilibrium method of imaginary-time field theory (Matsubara technique). However, if one proceeds in a straightforward way, we argue that one does not necessarily get the correct answer for the electric current.

1.4.4 Chapter 5

As we have mentioned above, the analysis [98] indicates that the Chern-Simons term *is* induced by parity-violating particle interactions in a theory with local four-fermion interaction (Fermi theory). However, we know that in the Standard Model, this interaction is actually non-local, but is mediated by massive W- and Z-bosons. Therefore, in Chapter 5 we extend the original study [98] to a simplified theory with *one* massive boson, which mediates the parity-violating four-fermion interaction. The conclusion is that different contributions to the Chern-Simons term in plasma cancel each other, so that no parity-odd effective action is induced for the electromagnetic field. We argue that the reason of this apparent conflict with the result of the local theory lies in that the prediction for the Chern-Simons term in Fermi theory actually involves an ambiguity, which was not taken into account before.

Chapter 2

Experimental bounds on sterile neutrino mixing angles

2.1 Introduction

As discussed in the Introduction (Section 1.2.1), neutrinos are massive and can change their *flavours* while propagating (see e.g. [104] for a review). This is one of the few firmly established phenomena beyond the Standard Model of particle physics. While the absolute scale of neutrino masses is not determined yet, combinations of direct measurements and oscillations experiments put the sum of their masses below 2 eV [105] while from the cosmological data one can infer an upper bound of 0.58 eV at 95% CL [106].

Thus the neutrinos are massive but their mass is at least million times smaller than the masses of other fermions.

A traditional explanation of *both* neutrino oscillations *and* the smallness of neutrino masses is provided by the *see-saw mechanism* [46, 47, 48, 49], see also Section 1.3. It assumes the existence of several *right-handed neutrinos* (Fig. 1.3) coupled to their Standard Model counterparts via the Yukawa interaction, providing the Dirac masses, M_{D}, for neutrinos. The Yukawa interaction terms dictate the SM charges of the right-handed particles: they turn out to carry no electric, weak and strong charges; therefore they are often termed “singlet,” or “sterile” fermions. Sterile neutrinos can thus have Majorana masses, M_s, consistent with the gauge symmetries of the Standard Model. If the Majorana masses are much larger than the Dirac ones, the *type I seesaw formula* (1.10) holds [46, 47, 48, 49]. The masses of sterile neutrinos are much heavier than the active neutrino masses as a consequence of this formula. This creates quite a unique situation: the left-chiral and right-chiral counterparts behave as two distinct particles with different masses and interaction strengths.

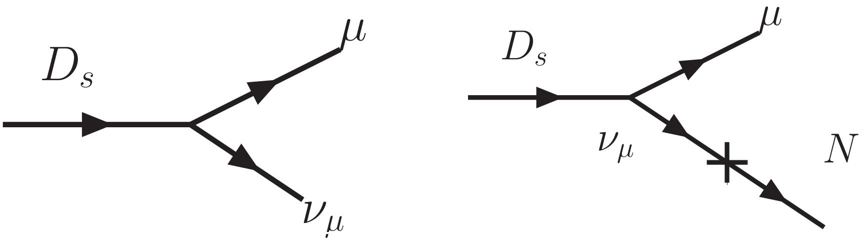

Figure 2.1: Leptonic decay of the D_s meson, $D_s \to \mu^+ + \nu_\mu$ (left) is accompanied by the decay to sterile neutrino, N, $D_s \to \mu^+ + N$ (right). On the right, the weak eigenstate ν_μ is converted to the mass eigenstate of N. The relative probability of the left and right processes is different by $\vartheta^2 = |M_{\rm D}/M_s|^2$.

As we have argued in Sec. 1.3, although sterile neutrinos are neutral with respect to the SM charges, they interact with the SM matter through mixing with active neutrinos, and can be detected (See Fig. 2.1). This opens a possibility to search for sterile neutrinos at particle physics experiments.

Any process with active neutrino in the initial or final state **has its counterpart with sterile neutrino** (if kinematically allowed) with the probability suppressed by the squared mixing angle ϑ^2.

2.1.1 Previous bounds on sterile neutrino interactions

Numerous searches for sterile neutrinos in the mass range up to $\sim$ 500 GeV had been performed in the past (see the corresponding section in Particle Data Group [105],[1] see also [107, 101] and refs. therein). These searches provided *upper bounds* on the strength of interaction of these neutral leptons with the SM neutrinos of different flavours – active-sterile neutrino *mixing angles* for sterile neutrino with the mass M_s.[2] These bounds then can be interpreted as *lower bounds* on the lifetime of sterile neutrinos τ_s via

$$\tau_s^{-1} = \frac{G_F^2 M_s^5}{96\pi^3} \sum_\alpha \vartheta_\alpha^2 \sum_X B_X^{(\alpha)}, \tag{2.1}$$

where the sum runs over various kinematically allowed decay modes X of sterile neutrinos. The coefficients $B_X^{(\alpha)}$ depend on the sterile neutrino mass. For example,

---

[1] `http://pdglive.lbl.gov/Rsummary.brl?nodein=S077&inscript=Y`

[2] Here and below we use the letter ϑ for *active-sterile mixing angles* (defined by Eq. (2.12) below) while reserving θ_{12}, θ_{13} and θ_{23} for the measured parameters of the active neutrinos matrix $\hat{m}_\nu$. These quantities ϑ_α are often denoted $|V_{4\alpha}|^2$ or $|U_{x\alpha}|^2$ in the experimental papers, to which we refer. Here and below the Greek letters α, β are flavour index e, μ, τ and $i, j = 1, 2, 3$ denote active neutrino mass eigenstates.

if sterile neutrino is lighter than two electron masses, then the only kinematically allowed decay mode is $N \to \nu\nu\bar{\nu}$, and

$$B^{e}_{\nu\nu\nu} = B^{\mu}_{\nu\nu\nu} = B^{\tau}_{\nu\nu\nu} = 1 \tag{2.2}$$

For higher masses, the coefficients $B_X^{(\alpha)}$ can be read from [99].

The lower bound on the lifetime τ_s is usually dominated by the least constrained mixing angle, which happens to be ϑ_τ^2 (as will be shown later). This bound can be made *stronger* if one assumes that the same particles are also responsible for the neutrino oscillations. The see-saw formula (2.3) limits (at least partially) possible values of ratios of the mixing angles $\vartheta_\alpha^2/\vartheta_\beta^2$. In the simplest case when only two sterile neutrinos are present (the minimal number, required to explain two observed neutrino mass differences) the ratios of mixing angles varies within a limited range, see e.g. [108, 109]. While this range can be several orders of magnitude large (owing to our ignorance of certain oscillation parameters, such as e.g. a CP-violating phase [108, 109]), the implied (lower) bounds on the lifetime become much stronger, essentially being determined by the *strongest*, rather than the weakest direct bound on ϑ_α.

The structure of this Chapter

In this Chapter we summarize restrictions on sterile neutrino lifetime in view of the recent results of the Daya Bay [10] and RENO [9] collaborations, that measured a non-zero mixing angle θ_{13} (see also [13, 12]). We demonstrate that in the case when there are only two sterile neutrinos, responsible for the observed neutrino oscillations, the oscillation data allow for such a choice of the active-sterile Yukawa couplings that the mixing of sterile neutrinos with any given flavour can be strongly suppressed. This happens *only* for a non-zero values of θ_{13}, in the range consistent with the current measurements [110, 111, 10, 9]. The results of this Chapter partially overlap with [112] (also [113]), and we make the comparison with the previous works in the corresponding places.

This Chapter is organized as follows: in Section 2.2 we briefly describe the model of sterile neutrinos that we use. We then investigate the relations between different mixing angles imposed by the see-saw mechanism and demonstrate that the mixing with any flavour ϑ_α^2 can become suppressed (Section 2.3). Section 2.4 is devoted to the overview of the experiments, searching for sterile neutrinos with the masses below 2 GeV, and the way one should interpret their results to apply to the see-saw models that we study. Section 2.5 summarizes our revised bounds on mixing angles and translates them into the resulting constraints on sterile neutrino lifetime (Figs. 2.8). We conclude in Section 2.6, discussing implications of our results and confronting them with the bounds from primordial nucleosynthesis.

2.2 Sterile neutrino Lagrangian

The minimal way to add sterile neutrinos to the Standard Model is provided by the Type I see-saw model (Eq. (1.9) in Section 1.3), see also [46, 47, 48, 49], [114, 115, 116, 117] and refs. therein). This model contains $\mathcal{N}$ new fermions N_I — sterile neutrinos. *How many of them can there be?*

The masses of the active neutrinos are given by the seesaw relation

$$\hat{m}_\nu = -M_{\text{D}} M_s^{-1} M_{\text{D}}^T, \tag{2.3}$$

where $\hat{m}_\nu$ is a 3×3 matrix of active neutrino masses, mixings, and (possible) CP-violating phases, M_s is the matrix of the Majorana masses of sterile neutrinos N_I and the M_{D} is the usual Dirac mass term coupling active and sterile neutrinos. Formula (1.10) is a particular case of the relation (2.3) for $mathcal N = 3$ and diagonal form of the Majorana matrix M_s.

The number of these singlet fermions must be $\mathcal{N} \geq 2$ to explain the data on neutrino oscillations. In the case of $\mathcal{N} = 2$ there are *11 new parameters* in the Lagrangian (1.9), while the neutrino mass/mixing matrix $\hat{m}_\nu$ has 7 parameters in this case. The situation is even more relaxed for $\mathcal{N} > 2$. The see-saw formula (2.3) does not allow to fix the scale of Majorana and Dirac $M_{\text{D},\alpha I} = F_{\alpha I}\langle\Phi\rangle$ masses.

2.2.1 Two quasi-degenerate sterile neutrinos

In this work we will mostly concentrate on sterile neutrinos with their masses M_s in the MeV–GeV range – the range in which the past direct accelerator searches were the most sensitive. To further simplify our analysis we will concentrate on the case when the masses of both sterile neutrinos are close to each other (so that $\Delta M \ll M_s$). One important example of such model is provided by the *Neutrino Minimal Standard Model* (the νMSM) ([118, 119], see [120] for review). Within the νMSM there are **3** sterile neutrinos, whose masses are roughly of the order of those of other leptons in the Standard Model (see Section 1.3.4). Two of these particles are approximately degenerate in their mass and are responsible for baryogenesis and neutrino oscillations and the third one is playing the role of dark matter. As we have noticed in Section 1.3, the requirement of dark matter stability on cosmological timescales makes its coupling with the Standard Model species so feeble, that it does not contribute significantly to the neutrino oscillation pattern [118, 121]. Therefore, when analyzing neutrino oscillations, the N_1 can be omitted from the Lagrangian and index I in the sums runs through 2 and 3 only. Taking into account that $M_2 \approx M_3 \approx M_s$, we perform a rotation in the space $(N_2, N_3) \to (\boldsymbol{N}_2, \boldsymbol{N}_3)$ such that the Majorana mass term of the see-saw Lagrangian (1.9) is off-diagonal[3]

---

[3] This parametrization coincides with [109, Eq. (2.1)].

$$\Delta\mathcal{L}^{\nu\mathrm{MSM}}_{N_2,N_3} = i\bar{\boldsymbol{N}}_I \partial\!\!\!/ \boldsymbol{N}_I - M_{\mathrm{D},\alpha I}\bar{\nu}_\alpha \boldsymbol{N}_I - M^*_{\mathrm{D},\alpha I}\bar{\boldsymbol{N}}_I \nu_\alpha - M_s\left(\bar{\boldsymbol{N}}^c_2 \boldsymbol{N}_3 + \bar{\boldsymbol{N}}_3 \boldsymbol{N}^c_2\right) \tag{2.4}$$

In what follows we will abuse the notations and continue to use N_2, N_3 also for the basis of the Lagrangian (2.4).

2.3 Solution of the see-saw equations

In this Section we investigate how mixing angles between active and sterile neutrinos are related to parameters of the observable neutrino matrix $\hat{m}_\nu$. We will demonstrate that the mixing angle ϑ^2_e in the case of normal hierarchy and the mixing angles ϑ^2_μ or ϑ^2_τ in the case of inverted hierarchy, can become suppressed as we vary the parameters of the neutrino matrix away from their best-fit values (but within the experimentally allowed 3σ bounds).

2.3.1 Parametrization of the Dirac mass matrix

We use the Pontecorvo–Maki–Nakagawa–Sakata (PMNS) parametrization of the neutrino matrix $\hat{m}_\nu$ (see e.g. Eqs.(2.10) and (2.12) of [104])

$$\hat{m}_\nu = V^*\mathrm{diag}(m_1 e^{-2i\zeta},\ m_2 e^{-2i\xi},\ m_3)V^\dagger\ , \tag{2.5}$$

where V is the unitary matrix, whose explicit standard form is (cf. e.g. [104])

$$V = \begin{pmatrix} 1 & 0 & 0 \\ 0 & c_{23} & s_{23} \\ 0 & -s_{23} & c_{23} \end{pmatrix} \begin{pmatrix} c_{13} & 0 & s_{13} \\ 0 & e^{i\phi} & 0 \\ -s_{13} & 0 & c_{13} \end{pmatrix} \begin{pmatrix} c_{12} & s_{12} & 0 \\ -s_{12} & c_{12} & 0 \\ 0 & 0 & 1 \end{pmatrix}$$

$$= \begin{pmatrix} c_{12}c_{13} & c_{13}s_{12} & s_{13} \\ -c_{23}s_{12}e^{i\phi} - c_{12}s_{13}s_{23} & c_{12}c_{23}e^{i\phi} - s_{12}s_{13}s_{23} & c_{13}s_{23} \\ s_{23}s_{12}e^{i\phi} - c_{12}c_{23}s_{13} & -c_{12}s_{23}e^{i\phi} - c_{23}s_{12}s_{13} & c_{13}c_{23} \end{pmatrix}\ . \tag{2.6}$$

where $c_{ij} = \cos\theta_{ij}$, and $s_{ij} = \sin\theta_{ij}$.

Redefining a Dirac mass matrix as[4]

$$M_{\mathrm{D}} \to \tilde{M}_{\mathrm{D}} \equiv V^T M_{\mathrm{D}}\ , \tag{2.7}$$

we can rewrite the see-saw relation (2.3) in the following form:

$$\mathrm{diag}(m_1 e^{-2i\zeta},\ m_2 e^{-2i\xi},\ m_3)_{ij} = -\frac{\tilde{M}_{\mathrm{D},i2}\tilde{M}_{\mathrm{D},j3} + \tilde{M}_{\mathrm{D},i3}\tilde{M}_{\mathrm{D},j2}}{M_s}\ , \tag{2.8}$$

---

[4] The Dirac matrix $\tilde{M}_{\mathrm{D}}$ has indexes $I = 2, 3$ and $i, j = 1, 2, 3$, which correspond to sterile and active neutrino mass eigenstates, respectively.

	Normal hierarchy		Inverted hierarchy
Δm^2_{21}	$(7.09 - 8.19) \times 10^{-5}$ eV^2		
Δm^2_{31}	$(2.14 - 2.76) \times 10^{-3}$ eV^2	Δm^2_{13}	$(2.13 - 2.67) \times 10^{-3}$ eV^2
$\sin^2\theta_{12}$	$0.27 - 0.36$		
$\sin^2\theta_{23}$	$0.39 - 0.64$		
$\sin^2\theta_{13}$	$0.010 - 0.038$ $(0.013 - 0.040)$		

Table 2.1: The 3σ bounds on the parameters of the mass matrix $\hat{m}_\nu$, adopted from [123, 111, 10, 9]. Here $\Delta m^2_{ij} = m^2_i - m^2_j$. The boundaries for inverted hierarchy are the same as for the normal one, unless written explicitly. The range of $\sin^2\theta_{13}$ is taken from the data of the Daya Bay experiment [10] (the values in parentheses – from RENO [9]).

The rank of the active neutrino mass matrix $\mathcal{M}_\nu$ is 2 in the case of two sterile neutrinos, meaning that one of the masses m_i is zero.

In neutrino oscillations, only two independent combinations $m_2^2 - m_1^2$ and $m_3^2 - m_1^2$ of the active neutrino mass eigenvalues m_1, m_2, m_3 are measured. Based on this, two choices of "hierarchies" are possible, which cannot be distinguished from neutrino oscillation data alone. The first one is called *normal hierarchy* (NH) and corresponds to $0 \leq m_1 < m_2 < m_3$. The second one is called *inverted hierarchy* (IH) and is realized for $0 \leq m_3 < m_1 < m_2$.

Once the mass M_s is fixed, the solutions of Eq. (2.8) contain one unknown complex parameter, z. Its presence reflects a symmetry of the see-saw relation (2.8) under the change $(\tilde{M}_{\text{D},i2}, \tilde{M}_{\text{D},i3}) \to (z\tilde{M}_{\text{D},i2}, z^{-1}\tilde{M}_{\text{D},i3})$ [122]. It is this freedom that does not allow to fix the absolute scale of $\tilde{M}_\text{D}$ (i.e. the value of ϑ^2) even if M_s is chosen.

The change $z \to z^{-1}$ is equivalent to the redefinition of $N_2 \to N_3$, $N_3 \to N_2$ together with shift of the Majorana phase $\xi \to \xi + \pi$ in (2.8). Therefore in subsequent analysis we will choose $|z| \geq 1$ without the loss of generality.

2.3.2 Normal hierarchy

For normal hierarchy the explicit see-saw relation is

$$\text{diag}(0,\ m_2 e^{-2i\xi},\ m_3)_{ij} = -\frac{\tilde{M}_{\text{D},i2}\tilde{M}_{\text{D},j3} + \tilde{M}_{\text{D},i3}\tilde{M}_{\text{D},j2}}{M_s}\ . \tag{2.9}$$

Diagonal components of this matrix equation give

$$\tilde{M}_{\text{D},12}\tilde{M}_{\text{D},13} = 0,\ \ \tilde{M}_{\text{D},22}\tilde{M}_{\text{D},23} = \frac{1}{2}m_2 M_s e^{-2i\xi},\ \ \tilde{M}_{\text{D},32}\tilde{M}_{\text{D},33} = \frac{1}{2}m_3 M_s\ . \tag{2.10}$$

Using $m_2, m_3 \neq 0$ we find that $\tilde{M}_{\text{D},22}$, $\tilde{M}_{\text{D},23}$, $\tilde{M}_{\text{D},32}$, $\tilde{M}_{\text{D},33}$ are *all* non-zero. Analysis of non-diagonal terms reveals that *both* $\tilde{M}_{\text{D},12}$ and $\tilde{M}_{\text{D},13}$ are zero and there are two general solutions (c.f. [122]):

$$\tilde{M}^{\pm}_{\mathrm{D},i2} = iz\sqrt{\frac{M_s}{2}}(0,\ \pm ie^{-i\xi}\sqrt{m_2},\ \sqrt{m_3}),\ \ \tilde{M}^{\pm}_{\mathrm{D},i3} = iz^{-1}\sqrt{\frac{M_s}{2}}(0,\ \mp ie^{-i\xi}\sqrt{m_2},\ \sqrt{m_3})\ . \tag{2.11}$$

The solution $\tilde{M}^{+}_{\mathrm{D}}$ with $\xi = \psi + \pi$ equals to $\tilde{M}^{-}_{\mathrm{D}}$ with $\xi = \psi$. It allows us to consider only one solution $\tilde{M}^{+}_{D}$ on the interval $0 \leq \xi < 2\pi$. In what follows we therefore omit the superscript $+$.[5]

The mixing angles of the active-sterile neutrinos are defined as follows:

$$2\vartheta^2_\alpha \equiv \sum_I |(M_{\mathrm{D}}M_s^{-1})_{\alpha I}|^2 = \sum_I |(V^*\tilde{M}_{\mathrm{D}}M_s^{-1})_{\alpha I}|^2 = \frac{1}{M_s^2}\sum_I |(V^*\tilde{M}_{\mathrm{D}})_{\alpha I}|^2\ . \tag{2.12}$$

Inserting the explicit solution (2.11) for $\tilde{M}_{\mathrm{D}}$ results in

$$\vartheta^2_\alpha = \frac{|z|^2}{4M_s}\left|\sqrt{m_3}V_{\alpha 3} - ie^{i\xi}\sqrt{m_2}V_{\alpha 2}\right|^2 + \frac{1}{4M_s|z|^2}\left|\sqrt{m_3}V_{\alpha 3} + ie^{i\xi}\sqrt{m_2}V_{\alpha 2}\right|^2 . \tag{2.13}$$

For $|z| \gg 1$ the contribution of $\tilde{M}_{\mathrm{D},i3}$ is suppressed compared with that of $\tilde{M}_{\mathrm{D},i2}$ and therefore we neglect the former (we will comment below on the case $|z| \gtrsim 1$).

As the value of the Majorana phase ξ is undetermined experimentally, the condition $\vartheta_\alpha = 0$ is satisfied iff $m_3|V_{\alpha 3}|^2 = m_2|V_{\alpha 2}|^2$ (we neglect second term on the r.h.s. of (2.13)). For the electron flavour ($\alpha = e$) it translates into

$$\sin^2\theta_{12}\frac{m_2}{m_3} = \tan^2\theta_{13}, \tag{2.14}$$

which, in principle, can be satisfied only for non-zero θ_{13}. This result has been already obtained in [112].

The bounds on the parameters of the mass matrix $\hat{m}_\nu$ at the 3σ level that we use are shown in Table 2.1. Note that in the present analysis we do not take into account statistical correlations between different oscillation parameters, allowing them to vary independently within their 3σ intervals. Consequently, we obtain the 3σ intervals for the combinations of parameters, entering Eq. (2.14)[6]:

$$\begin{array}{rcccl} 0.043 & < & \sin^2\theta_{12}\frac{m_2}{m_3} & < & 0.070, \\ 0.010(0.014) & < & \tan^2\theta_{13} & < & 0.039(0.042), \end{array} \tag{2.15}$$

---

[5] Unlike the parametrizations used e.g. in Ref. [124, 122, 112] this way of parametrizing the solution of the see-saw equations shows that there is only one branch of solutions, with all other related to it via redefinitions $N_2 \leftrightarrow N_3$ and shift of the Majorana phases. In particular in the parametrization we used it is much easier to analyze whether mixing angles become zero. The relation $|z| = \exp(\mathrm{Im}\,\omega)$ holds, where the parameter ω was employed in [112].

[6] Throughout this Chapter whenever two numbers are given instead of one, the first is based on the results of the Daya Bay experiment [10], and the second one (in parentheses) is obtained based on the result of application of the RENO bounds [9] (see Table 2.1).

They imply that the relation (2.14) *does not* hold exactly for the neutrino oscillation parameters, presented in Table 2.1. Therefore the mixing angle ϑ_e^2 cannot become zero, but has a non-trivial lower bound. To find the minimal value that it can reach, we consider the ratio of the angles $\vartheta_e^2/(\vartheta_e^2+\vartheta_\mu^2+\vartheta_\tau^2)$. Due to the unitarity of V, the denominator is

$$\sum_\alpha \vartheta_\alpha^2 \approx \frac{1}{2M_s^2}\sum_{\alpha,\beta,\gamma} V^*_{\alpha\beta}\tilde{M}_{\mathrm{D},\beta 2}V_{\alpha\gamma}\tilde{M}^*_{\mathrm{D},\gamma 2} = \frac{1}{2M_s^2}\sum_\beta |\tilde{M}_{\mathrm{D},\beta 2}|^2 = \frac{|z|^2}{4M_s}(m_2+m_3). \tag{2.16}$$

Let us denote the ratio of the mixing of sterile neutrinos with one flavour to the sum of all mixings by T_α,

$$T_\alpha \equiv \frac{\vartheta_\alpha^2}{\sum\limits_\beta \vartheta_\beta^2}. \tag{2.17}$$

Then we get the following expression for T_e:

$$T_e = \frac{|ie^{i\xi}c_{13}s_{12}\sqrt{\frac{m_2}{m_3}} - s_{13}|^2}{1+\frac{m_2}{m_3}}. \tag{2.18}$$

The minimum is achieved if we push θ_{12} and Δm_{21}^2 to their 3σ lower boundaries, θ_{13} and Δm_{31}^2 to their upper boundaries, and choose $\xi = -\pi/2$. The maximum is achieved when we set Δm_{31}^2 equal to its lower bound, θ_{13}, θ_{12} and Δm_{21}^2 to their upper bounds, and by choosing the Majorana phase $\alpha = \pi/2$. The bounds on T_e from Table 2.2 translate into the bound for the muon and tau flavours combined:

$$0.83 \le T_\mu + T_\tau. \tag{2.19}$$

The minimum and maximum of different T_α are listed in the Table 2.2 and in Fig. 2.2.

This analysis was conducted in approximation of large $|z|$. See Sec. 2.3.4 for the account of finite-$|z|$ effects.

2.3.3 Inverted hierarchy

Similarly to the previous case, for the inverted hierarchy we get a solution of the see-saw equations (2.8)

$$\tilde{M}_{\mathrm{D},i2} = iz\sqrt{\frac{M_s}{2}}(e^{-i\zeta}\sqrt{m_1},\, ie^{-i\xi}\sqrt{m_2},\, 0),\;\; \tilde{M}_{\mathrm{D},i3} = iz^{-1}\sqrt{\frac{M_s}{2}}(e^{-i\zeta}\sqrt{m_1},\, -ie^{-i\xi}\sqrt{m_2},\, 0) \tag{2.20}$$

Normal hierarchy	Inverted hierarchy
$T_e \leq 0.15$	$0.02 \leq T_e \leq 0.98$
$0.09 \leq T_\mu \leq 0.89$	$0 \leq T_\mu \leq 0.60$
$0.08 \leq T_\tau \leq 0.88$	2×10^{-4} $(7 \times 10^{-5}) \leq T_\tau \leq 0.62$
The ranges are based on 2σ *bounds*	

Normal hierarchy	Inverted hierarchy
$T_e \leq 0.17$	$0.02 \leq T_e \leq 0.98$
$0.07 \leq T_\mu \leq 0.92$	$0 \leq T_\mu \leq 0.63$
$0.06 \leq T_\tau \leq 0.90$	$0 \leq T_\tau \leq 0.65$
The ranges are based on 3σ *bounds*	

Table 2.2: The ratio of the sterile neutrino mixing with a given flavour α to the *sum* of the three mixings, T_α (defined by (2.17)). **Left** table shows the upper and lower values of T_α when parameters of neutrino oscillations are allowed to vary within their 2σ boundaries (taken from [123]). The **right** table shows the results when the parameters of active neutrino oscillations are varied within their 3σ limits (see Table 2.1). For the explanation of the numbers in parentheses, see Footnote 6.

for $0 \leq \xi < 2\pi$. In this case ϑ_μ^2 or ϑ_τ^2 can become very suppressed, as we will show soon.

The mixing angles are

$$\vartheta_\alpha^2 = \frac{|z|^2}{4M_s} \left| \sqrt{m_1} V_{\alpha 1} - i e^{i(\xi - \zeta)} \sqrt{m_2} V_{\alpha 2} \right|^2 + \frac{1}{4M_s |z|^2} \left| \sqrt{m_1} V_{\alpha 1} + i e^{i(\xi - \zeta)} \sqrt{m_2} V_{\alpha 2} \right|^2 . \tag{2.21}$$

For $|z| \gg 1$ they can become close to zero only if $\sqrt{m_1}|V_{\alpha 1}| = \sqrt{m_2}|V_{\alpha 2}|$. For $\alpha = \mu$ this condition translates into

$$|\tan\theta_{12} + \sin\theta_{13} \tan\theta_{23} e^{-i\phi}| = \sqrt{\frac{m_2}{m_1}} |1 - \sin\theta_{13} \tan\theta_{12} \tan\theta_{23} e^{-i\phi}|. \tag{2.22}$$

For the parameter set close to the best fit, left-hand side is *less* than the right-hand side, because then $\sin\theta_{13} \approx 0$, while $\tan\theta_{12} < 1$ and $m_1 \approx m_2$. To attain the equality one has to push left-hand side up and the right-hand side down. $\phi = 0$ makes phases of both complex terms inside $|...|$ on the left-hand side equal, thereby the absolute value of their sum becomes maximal. Simultaneously the right-hand side becomes minimal. For this specific choice of the Dirac angle the equality (2.22) turns into

$$\frac{\sqrt{\frac{m_2}{m_1}} - \tan\theta_{12}}{\sqrt{\frac{m_2}{m_1}} \tan\theta_{12} + 1} = \sin\theta_{13} \tan\theta_{23}. \tag{2.23}$$

The 3σ bounds for inverted hierarchy in general are the same as for the normal one (see Table 2.1) with the exception of the "atmospheric" mass difference, that slightly differs. Using these values we find

$$0.14 < \frac{\sqrt{\frac{m_2}{m_1}} - \tan\theta_{12}}{\sqrt{\frac{m_2}{m_1}}\tan\theta_{12} + 1} < 0.24, \quad 0.08\ (0.09) < \sin\theta_{13}\tan\theta_{23} < 0.26. \tag{2.24}$$

We see that two regions overlap, therefore the relation (2.22) can be satisfied and ϑ_μ^2 can be zero in a wide region of values of the parameters of the neutrino oscillation matrix. See, however, Sec. 2.3.5 below.

Similarly, the condition $\vartheta_\tau = 0$ (for $\phi = \pi$) translates into

$$\frac{\sqrt{\frac{m_2}{m_1}} - \tan\theta_{12}}{\sqrt{\frac{m_2}{m_1}}\tan\theta_{12} + 1} = \sin\theta_{13}\cot\theta_{23}, \tag{2.25}$$

and can be satisfied, because the quantity on the right hand side varies from 0.07 (0.09) to 0.24 (0.25), well within the range of (2.24).[7]

On the other hand, ϑ_e can be zero only if

$$\cot\theta_{12} = \sqrt{\frac{m_2}{m_1}} \tag{2.26}$$

can be realized. The left hand side is always larger than the right hand side (within the 3σ region), therefore no ϑ_e suppression can occur. However it is important to know what minimal value this mixing angle can reach. According to Eq.(2.21) electron mixing angle is given by

$$\vartheta_e^2 = \frac{|z|^2}{4M_s}\cos^2\theta_{13}\left(m_1\cos^2\theta_{12} + m_2\sin^2\theta_{12} + \sin(\xi-\zeta)\sin 2\theta_{12}\sqrt{m_1 m_2}\right). \tag{2.27}$$

For $\xi - \zeta = -\pi/2$ this quantity is minimal

$$\vartheta_{e,min}^2 = \frac{|z|^2}{4M_s^2}\cos^2\theta_{13}\left(\sqrt{m_1}\cos\theta_{12} - \sqrt{m_2}\sin\theta_{12}\right)^2. \tag{2.28}$$

To compare it with the other mixing angles, we note that the relation

$$\sum_\alpha \vartheta_\alpha^2 \approx \frac{|z|^2}{4M_s}(m_1 + m_2) \tag{2.29}$$

---

[7] It was pointed out in [112] that both ϑ_μ and ϑ_τ can be suppress in inverted hierarchy, for $\theta_{13} = 0$. For this to happen the relation $\sqrt{\frac{m_2}{m_1}} = \tan\theta_{12}$ should hold, as one can also see from Eqs. (2.23) and (2.25). The corresponding value of θ_{12} is however well outside the 3σ interval. The general case $\theta_{13} \neq 0$ has not been analyzed in [112].

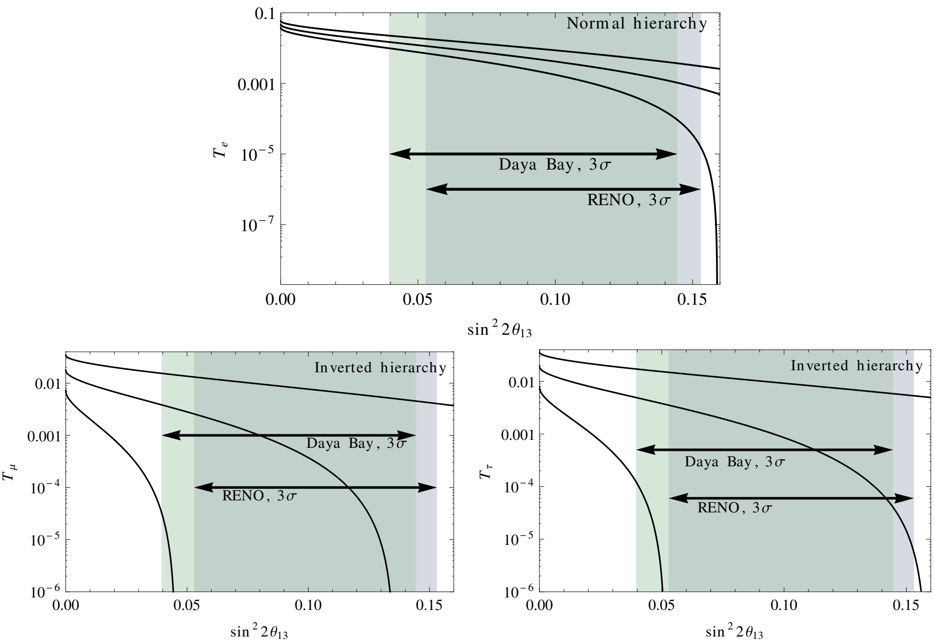

Figure 2.2: The minimal ratios of mixing angles $T_\alpha = \vartheta_\alpha^2 / \sum \vartheta_\beta^2$. **The upper** figure depicts normal hierarchy, **two lower** ones – IH. In all figures, the lower curve corresponds to the choice of the mixing angles and mass splittings that minimizes the ratio within the 3σ range, upper – that maximizes it, middle employs the best-fit parameters (for details of the choices, see Secs. 2.3.2, 2.3.3). CP-phases are $\xi = -\pi/2$ for the T_e-plot, $\phi = 0$, $\xi - \zeta = \pi/2$ for T_μ, and $\phi = \pi$, $\xi - \zeta = -\pi/2$ for T_τ. The bands *Daya Bay* and *RENO* correspond to the 3σ ranges of θ_{13}, indicated by the corresponding experiments [10, 9].

holds (similar to Eq.(2.16) in the case of normal hierarchy). Therefore

$$\frac{\vartheta_{e,min}^2}{\sum\limits_\alpha \vartheta_\alpha^2} = \frac{\cos^2\theta_{13}}{1 + \frac{m_2}{m_1}} \left(\cos\theta_{12} - \sqrt{\frac{m_2}{m_1}} \sin\theta_{12} \right)^2 . \tag{2.30}$$

The results of the analysis are listed in Table 2.2 and Fig. 2.2. From the upper bound on T_α we derive the bound

$$T_\mu + T_\tau \geq 0.02 \, . \tag{2.31}$$

We see that in this mass hierarchy it is possible for the overall coupling of the sterile neutrino to both μ and τ flavours to become tiny compared to the electron flavour coupling.

The analysis for the inverted hierarchy was made for $|z| \gg 1$. See the Sec. 2.3.4 below for the case $|z| \sim 1$.

2.3.4 Ratio of sterile neutrino mixing angles for $|z| \sim 1$

As the expressions (2.13) and (2.21) show, the mixing angles have two terms: one is proportional to $|z|^2$ and another to $|z|^{-2}$ (recall that $|z| \geq 1$). It was shown in Sec. 2.3.3 that for inverted hierarchy the $|z|^2$-term can be zero for ϑ_μ^2 and ϑ_τ^2, while the $|z|^{-2}$ term in general stays finite.

For a given value of $|z|$, the $|z|^{-2}$-term is bounded from above. According to (2.13) and (2.21), its maximum is realized simultaneously with the maximal value of

$$L_\alpha^{NH} = |V_{\alpha 3} + ie^{i\xi}\sqrt{\frac{m_2}{m_3}}V_{\alpha 2}|^2 \tag{2.32}$$

in the normal hierarchy, and

$$L_\alpha^{IH} = |V_{\alpha 1} + ie^{i(\xi-\zeta)}\sqrt{\frac{m_2}{m_1}}V_{\alpha 2}|^2 \tag{2.33}$$

in the inverted hierarchy.

Analysis, similar to that of the Sections 2.3.2–2.3.3 shows that

$$L_e^{NH} \leq 0.2, \quad L_\mu^{NH} \leq 1.1, \quad L_\tau^{NH} \leq 1.1, \quad L_e^{IH} \leq 1.96, \quad L_\mu^{IH} \leq 1.3, \quad L_\tau^{IH} \leq 1.3\,. \tag{2.34}$$

These bounds allow to estimate the contribution of the $|z|^{-2}$-terms to the whole sum of the squared mixing angles

$$\sum_\alpha \vartheta_\alpha^2 = \frac{m_1+m_2+m_3}{4M_s}\left(|z|^2 + \frac{1}{|z|^2}\right)\,. \tag{2.35}$$

The ratio of (2.32)–(2.33) to (2.35) gives

$$R_\alpha^{NH} = \frac{L_\alpha^{NH}}{(1+\frac{m_2}{m_3})}\frac{1}{|z|^4+1}, \quad R_\alpha^{IH} = \frac{L_\alpha^{IH}}{(1+\frac{m_2}{m_1})}\frac{1}{|z|^4+1}\,. \tag{2.36}$$

For $z \sim 1$ it can become of order unity. However, we restrict ourselves to the sufficiently large values $z \gtrsim 10$, that are consistent with the upper bound, indicated by the experiments (see Fig.2.9)

$$R_e^{NH} \lesssim 2\times 10^{-5}, \quad R_{\mu,\tau}^{NH} \lesssim 10^{-4}, \quad R_e^{IH} \lesssim 10^{-4}, \quad R_{\mu,\tau}^{IH} \lesssim 5\times 10^{-5}\,. \tag{2.37}$$

Comparison these results with the *lower* bounds (Table 2.2) we see that z^{-1} terms are unimportant for the for all mixing angles in NH and ϑ_e in IH. What concerns the remaining angles ϑ_μ and ϑ_τ in IH, they can be substantially modified by account of z^{-1}-terms, but anyway each of them can become small enough, compared to the other angles, as explained in next section. As a corollary, analysis and results of Secs. 2.3.2,2.3.3 do not change significantly for large enough values of z.

2.3.5 Minimal mixing angles in the νMSM

Finally, we find the *minimal* values of the sterile neutrino mixing angles in the νMSM , compatible with the neutrino oscillation data. These angles will turn out to be much smaller than the experimental upper bounds in all regions of masses, probed by the experiments. A general solution of the see-saw equations (2.13), (2.21) gives ϑ as a function of $|z|$:

$$\vartheta_\alpha^2 = A_\alpha |z|^2 + \frac{B_\alpha}{|z|^2} \tag{2.38}$$

with coefficients A_α and B_α independent of $|z|$. The minimum of this expression is reached for $|z|_\alpha^2 = \sqrt{B_\alpha/A_\alpha} \geq 1$ and is given by

$$(\vartheta_\alpha^2)_{\text{min}} = 2\sqrt{A_\alpha B_\alpha}. \tag{2.39}$$

To find the *absolute* lower bound on the mixing angle for a given sterile neutrino mass, we vary this expression over the parameters of neutrino oscillations. The resulting mixing angles and the corresponding values of $|z|$ are listed in Table 2.3.[8] One can see that the values presented therein do not depend significantly on the 3σ upper bound on θ_{13} that we choose. The only exception is the minimum of the ϑ_e angle. In this case the exact value of the upper bound on θ_{13} defines how close A_α, and hence $(\vartheta_\alpha^2)_{\text{min}}$, can come to zero.

For the mixing angles $\vartheta_{\mu,\tau}^2$ in the case of inverted hierarchy $A_\alpha = 0, B_\alpha \neq 0$ and formally for infinitely large $|z|$ they would become zero. The value of $|z|$, however, is bounded from above, $|z| < z_{\text{max}}$, by the requirement that *none of three* mixing angles exceeds its upper bound (for quantitative estimates of z_{max}, look at Fig. 2.9). Therefore the couplings to μ and τ neutrinos remain *finite*. Estimates of mixing angles can be provided for B_α given by L_α^{IH} (2.33,2.34), along with $A_{\mu,\tau} = 0$, $z = z_{\text{max}}$

$$\vartheta_{\mu,\tau}^2 \gtrsim 2\times 10^{-8}\frac{\text{MeV}}{M_s z_{\text{max}}^2}, \qquad \text{(IH)} \tag{2.40}$$

---

[8] Notice, that the ratio of the mixing angles $\vartheta_\alpha^2/\vartheta_\beta^2$ does not reach its minimum when (2.39) is satisfied. The values of $|z|$ for which the bounds on the lifetime are relaxed the most are those when some of the mixing angles reach their upper experimentally allowed value.

Flavour α	$(\vartheta^2_\alpha)_{\min}$ @ 1 MeV	$\lvert z\rvert$
e	7×10^{-10}	2.2 (2.4)
μ, τ	10^{-8}	1.5

(a) NH, best-fit

Flavour α	$(\vartheta^2_\alpha)_{\min}$ @ 1 MeV	$\lvert z\rvert$
e	10^{-10} (4×10^{-11})	6.2 (9.8)
μ	8×10^{-10} (6×10^{-10})	5.4 (6.3)
τ	1.2×10^{-9} (1.0×10^{-10})	4.6 (5.1)

(b) NH, 3σ

Flavour α	$(\vartheta^2_\alpha)_{\min}$ @ 1 MeV	$\lvert z\rvert$
e	10^{-8}	2.3
μ, τ	2×10^{-9}	3.5

(c) IH, best-fit

Flavour α	$(\vartheta^2_\alpha)_{\min}$ @ 1 MeV	$\lvert z\rvert$
e	6×10^{-9}	2.7
μ, τ	see text	

(d) IH, 3σ

Table 2.3: Minimal values of the active-sterile mixing angles ϑ^2_α, obtained using the best-fit values of neutrino oscillation parameters or by varying the neutrino oscillation data within their 3σ intervals, listed in Table 2.1. The values for $(\vartheta^2_\alpha)_{\min}$ are provided for sterile neutrinos with the mass $M_s = 1$ MeV. For other masses one should multiply them by $(\,\text{MeV}/M_s)$. Columns "$|z|$" show the values of $|z|$ for which the minimum in (2.38) is reached. For the explanation of numbers in brackets, see Footnote 6.

2.4 Experimental bounds on sterile neutrino mixings

The direct experimental searches for neutral leptons had been performed by a number of collaborations [125, 126, 127, 128, 129, 130, 131, 132, 133, 134, 135, 136, 137] (see e.g. [108, 107] for review of various constraints). The negative results of the searches are converted into the *upper* bound on $\vartheta_\alpha \vartheta_\beta$ for different flavours. If neutrino oscillations are mediated by these sterile neutrinos, these bounds can be translated into the *upper* bounds on parameter $|z|$ and *lower* bounds on sterile neutrino lifetime.

Below, we take a closer look at two main types of experiments ("peak searches" and "fixed target experiments")[9] and describe *reinterpretation of these bounds* in

---

[9] The neutrinoless double-beta decay ($0\nu\beta\beta$) does not provide significant restrictions on the

the case, when sterile neutrinos with MeV–GeV masses are also responsible for neutrino oscillations.

2.4.1 Peak searches

In "*peak search*" experiments [140, 141, 142, 143], one considers the two-body decay of charged π or K mesons to charged lepton ($e^\pm$ or $\mu^\pm$) and neutrino (see e.g. [107] for discussion). In case of the pion decay the limit on ϑ_e^2 for masses in the range $60\,\mathrm{MeV} \leq M_s \leq 130\,\mathrm{MeV}$ is provided by the searches for the secondary positron peak in the decay $\pi^+ \to e^+ N$ to the massive sterile neutrino N as compared to the primary peak coming from the $\pi^+ \to e^+ \nu_e$ decay. Recent analysis of [136] puts this limit at $\vartheta_e^2 < 10^{-8}$ in the mass range $60 - 129\,\mathrm{MeV}$, for earlier results see [127, 128]. In the smaller mass region ($4\,\mathrm{MeV} \lesssim M_s \lesssim 60\,\mathrm{MeV}$) Refs. [127, 128] provided the bound based on the change of the number of events in the primary positron peak located at energies $M_\pi/2$. Similar bounds were obtained for the same mixing angle in studies of *kaon* decays [131] and for the ϑ_μ^2 in the decays of both pions [133, 134, 135] and kaons [131, 132].

The *lower* bound on the sterile neutrino lifetime τ_s in the model (2.4), based on the peak search data and neutrino oscillations is shown in Fig. 2.3 by dot-dashed green lines. The parameters of neutrino mixing matrix are allowed to vary within their 3σ limits (to minimize τ_s, while still keeping the values of all mixing angles compatible with the bounds from direct experimental searches).

2.4.2 Fixed target experiments and neutral currents contribution

The second kind of experiments ("*fixed target experiments*") [126, 129, 130] aims to create sterile neutrinos in decays of mesons and then searches for their decays into pairs of charged particles. Notice, that the expected signal in this second case is proportional to ϑ_α^4 or $\vartheta_\alpha^2\vartheta_\beta^2$ (and not to ϑ_α^2 as in the case of peak searches, discussed in the Section 2.4.1). We will demonstrate below that in the models like (2.4) (and in particular in the νMSM) the results of some fixed target experiments should be reinterpreted and will provide stronger bounds than discussed in previous works [108, 107, 112] (see also [144]).

2.4.3 Reinterpretation of the PS191 and CHARM experiments

The experiment **PS191** at CERN was a "fixed target" type of experiment described above [125, 126]. In searches for sterile neutrinos lighter than the pion

---

parameters of the sterile neutrinos in the type-I see-saw models (contrary to the case discussed in e.g. [107]), see discussion in [112, 138]. In particular, this is the case in the νMSM [139].

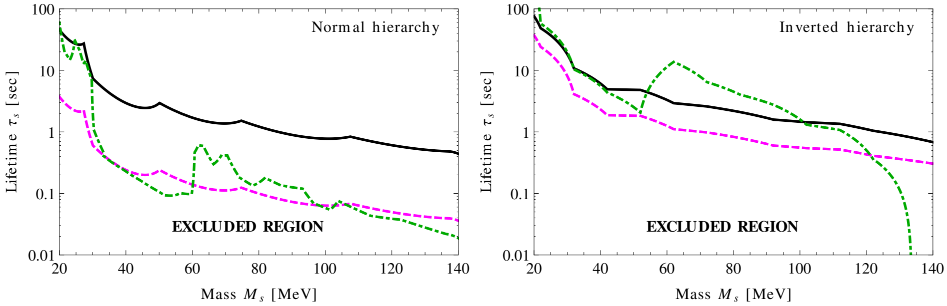

Figure 2.3: The lower bounds on the lifetime of sterile neutrinos, responsible for the mixings between active neutrinos of different flavours in the see-saw models (2.4). The bounds are based on the combination of negative results of direct experimental searches [125, 126, 128, 136, 131, 132, 133, 134, 135] with the neutrino oscillation data [123]. The neutrino oscillation parameters are allowed to vary within their 3σ confidence intervals to minimize the lifetime. The solid black curve is based on our reinterpretation of PS191 data *only*, that takes into account charged and neutral current contributions (see Sec. 2.4.3). The interpretation of the PS191 experiment, taking into account only CC interactions (used e.g. in the previous works [108, 112]) is shown in magenta dashed line. The bound from peak searches experiments *only* [128, 136, 131, 132, 133, 134, 135] is plotted in green dot-dashed line.

$M_s < M_\pi$, the pair of charged particles that were searched for in the neutrino decay comprised mostly of electron and positron:

$$\begin{aligned} \pi^+/K^+ \to e^+ + \quad & N \\ & \hookrightarrow e^+ \, e^- \nu_\alpha \ , \end{aligned} \tag{2.41}$$

where N is a sterile neutrino with the mass M_s. The first reaction in the chain is solely due to the *charged-current* (CC) interaction, and its rate is proportional to the ϑ_e^2.

If sterile neutrinos interact through both *charged and neutral currents* (CC+NC) as it is the case in the models with the see-saw Lagrangian (2.4), any of three active-neutrino flavours may appear in the decay of N in (2.41). The decay widths are [140]:

$$\Gamma(N \to e^+ e^- \nu_\alpha) = c_\alpha \vartheta_\alpha^2 \frac{G_F^2 M_s^5}{96\pi^3}, \tag{2.42}$$

with the following definition[10]

$$c_e = \frac{1 + 4\sin^2\theta_W + 8\sin^4\theta_W}{4}, \quad c_\mu = c_\tau = \frac{1 - 4\sin^2\theta_W + 8\sin^4\theta_W}{4}, \tag{2.43}$$

---

[10] Note that in the Ref. [145] there is a typo in the expression for c_τ (Eq. (2)).

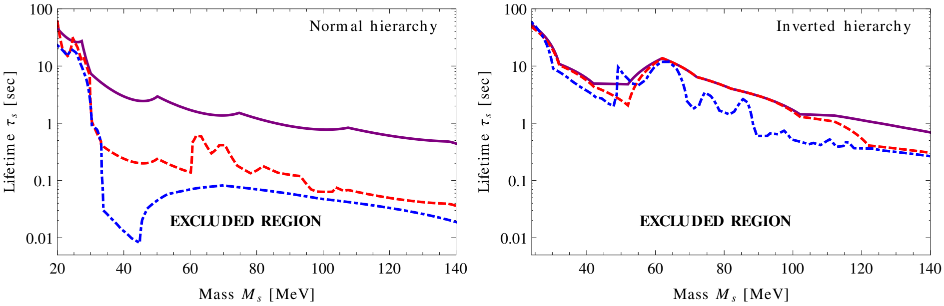

Figure 2.4: Comparison with the previous bounds on sterile neutrino lifetime in the νMSM [112]. The solid purple curves represent the results of the present analysis, obtained by the combination of peak searches experiments [128, 136, 131, 132, 133, 134, 135] together with the reanalysis of PS191, that takes into account neutral currents (a union of black and green bounds from Fig. 2.3). The red dashed curve is based on the combination of the same peak searches with the *original* interpretation of PS191 (i.e., with charged current interactions only). The blue dot-dashed line is taken from [112]. *Notice*, that the results of [112] were multiplied by a factor 2 to account for the Majorana nature of the particles (see discussion in Sec. 2.4.4), that was missing therein. The difference between the red and blue lines in the case of normal hierarchy is explained by wider 3σ intervals for neutrino oscillation data, used in [112], compared to our analysis.

and θ_W is the Weinberg's angle so that $\sin^2\theta_W \approx 0.231$ and $c_e \approx 0.59$, $c_{\mu(\tau)} \approx 0.13$. Therefore, the total number of events inside the detector that registers electron-positron pairs would be proportional to the combination of mixing angles $\vartheta_e^2 \times (\sum c_\alpha \vartheta_\alpha^2)$.

However, the model employed in the interpretation of the PS191 experiment [125, 126] was different, as has already been pointed in [144]. In the original analysis it was assumed that sterile neutrino interacts *only via charged currents*, but not through neutral currents. In our language it means that $c_e = 1, c_{\mu(\tau)} = 0$ was used instead of the values (2.43)[11]. As was noticed above, the probability of meson decay into sterile neutrino does not alter if we exclude the neutral-current interaction, and therefore the total number of events with the electron-positron pair would be proportional to $\vartheta_e^2 \times \vartheta_e^2$.

Therefore if we denote the bounds listed in [125, 126] as $\vartheta_e^4 \leq \vartheta_{e(exp)}^4$, then

---

[11] Model described in [125, 126] contains only one Dirac neutrino, while in the νMSM we have two Majorana fermions. Therefore actually $c_e = 1/2$ in the original model. For details see Sec. 2.4.4

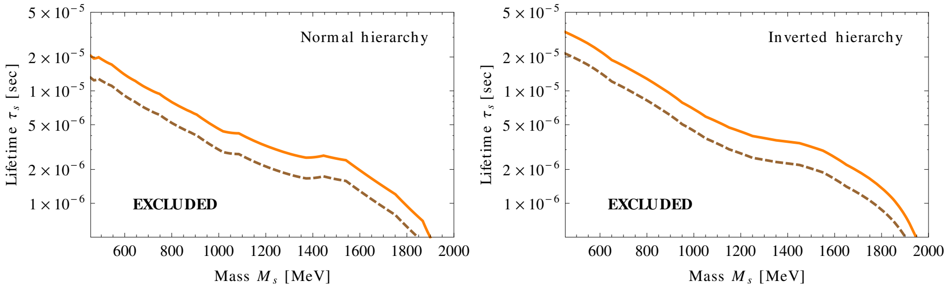

Figure 2.5: Comparison of the bounds on sterile neutrino lifetime (in the model (2.4)) based on the results of the CHARM experiments [130] *solely* (combined with the neutrino oscillation data). The orange (upper) curves correspond to the model with charged and neutral current interactions of sterile neutrinos, the brown (lower) – to the model with charged current interactions only. For details, see Sec. 2.4.3.

the bound for the νMSM takes form

$$\vartheta_e^2 \left(\sum_{\alpha=\{e,\mu,\tau\}} c_\alpha \, \vartheta_\alpha^2 \right) \leq \vartheta^4_{e(exp)} \,. \tag{2.44}$$

Similar bounds can be extracted from the reanalysis of meson decays into *muon* and sterile neutrino, that leads to replacement $e \to \mu$ in (2.44). As a result, the reinterpretation of the results of the PS191 experiment in combination with neutrino oscillation data produces up to an order of magnitude *stronger* bounds on lifetime than in the previous works (see Figs. 2.3 and 2.4).

Similarly, the CHARM experiment [130] provided bounds on the mixing angles of sterile neutrinos in the mass range $0.5\text{ GeV} \lesssim M_s \lesssim 2\text{ GeV}$. In the original analysis NC contributions *were neglected*. Therefore, to apply the results of this experiment to the case of the νMSM , we reanalyzed the data as described above. In Fig. 2.5 we compare lifetime bounds coming from the CHARM experiment solely for CC and CC+NC interactions of sterile neutrinos. The difference in this case is about a factor of 2.[12]

---

[12] In the case of the PS191 experiment, when using CC only for masses below the mass of pion suppression of the ϑ_e^2 mixing angle due to neutrino oscillations meant that instead of ϑ_e^2 bounds the lifetime is defined by the (much weaker) ϑ_μ^2 bounds. That led to the significant relaxation of the lower bound on the lifetime. If NC were taken into account, this was not possible anymore and therefore the lower bound on sterile neutrino lifetime became stronger by as much as the order on magnitude (black vs. magenta curve on the left panel in Fig. 2.3. In case of the CHARM experiment, both ϑ_e^2 and ϑ_μ^2 are strongly constrained and switching from one constraint to another makes (numerically) much smaller difference.

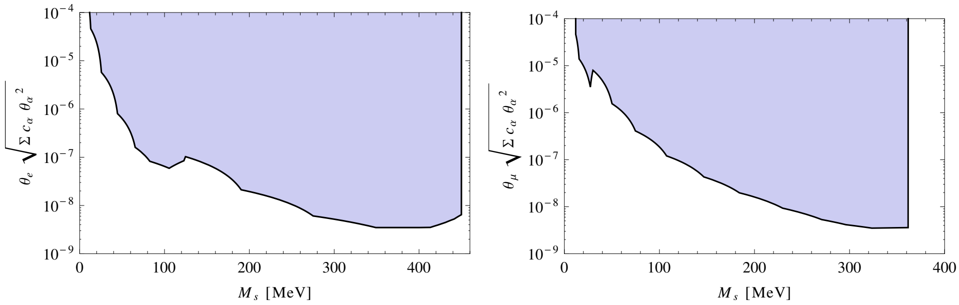

(a) Bound on the combination $\vartheta_e\sqrt{\sum c_\alpha\vartheta_\alpha^2}$ (b) Bound on the combination $\vartheta_\mu\sqrt{\sum c_\alpha\vartheta_\alpha^2}$

Figure 2.6: Direct accelerator bounds on the combination of active-sterile neutrino mixing angles, resulting from the reanalysis of the PS191 experiment [125, 126], taking into account decays of sterile neutrino through both charged and neutral currents and their Majorana nature. The shaded region is excluded. The case, analyzed in the original works [125, 126] (decay of sterile neutrino through the charged current only) corresponds to the choice $c_e = 1$, $c_\mu = c_\tau = 0$, for details, see Sec. 2.4.3. We plot the bounds for *two Majorana* neutrinos (as in Fig. 2.7) while in the original works [125, 126] a single Dirac neutrino was analyzed.

2.4.4 A note on Majorana vs Dirac neutrinos

For completeness we briefly discuss the difference in interpreting experimental results for *Majorana vs. Dirac sterile neutrinos*. Similar discussion can be found e.g. in [108]. When interpreting the experimental results one should take into account that in present analysis we consider *two Majorana sterile neutrinos*, while the experimental papers often phrase their bounds in terms of the mixing with a single *Dirac* neutrino, that we will denote U_α^2. In the νMSM twice more sterile neutrinos are produced per single reaction (because there are two sterile species – N_2 and N_3), and, owing to their Majorana nature, each sterile neutrino decays twice faster (additional charge-conjugated decay modes are present). Notice, that the mass splitting between between two sterile states N_2, N_3 is small $|M_2 - M_3| \ll \frac{1}{2}(M_2 + M_3) = M_s$ and once born, the states oscillate fast into each other. Averaging over many oscillations can be accounted for by an extra factor $\frac{1}{2}$ in the number of N_2 and N_3 species. Therefore, for fixed target experiments one gets the same number of the detector events involving one Dirac sterile neutrino as one gets in the νMSM if $(\vartheta_{\alpha 2}^2 + \vartheta_{\alpha 3}^2)^2 = U_\alpha^4$. That is, one should identify $2\vartheta_\alpha^2$ with the measured U_α^2 (recall (2.12) that $\vartheta_\alpha^2 = \frac{1}{2}(\vartheta_{\alpha 2}^2 + \vartheta_{\alpha 3}^2)$). In the case of peak searches, the bound U_α^2 should be interpreted in the νMSM as $\vartheta_{\alpha,2}^2 + \vartheta_{\alpha,3}^2 \le U_\alpha^2$, as production of *any* state N_2 or N_3 contributes to the number of events in the secondary peak, i.e. again $2\vartheta_\alpha^2$ should be identified with U_α^2. Notice, that this factor 2 is missing in [112].

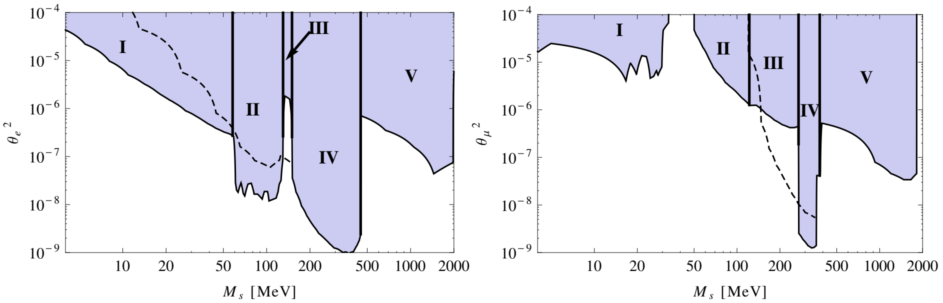

Figure 2.7: Direct accelerator bounds on the mixing angles. **Left panel:** ϑ_e^2 bounds, taken from [128] (region I), [136] (region II), [131] (region III), [126, 146] (region IV) and [130] (region V). **Right panel:** ϑ_μ^2 bounds, taken from [133, 134, 135] (region I), [131](region II), [132] (region III), [126](region IV) and [129] (region V). The shaded regions are ruled out by the experimental findings. Dashed curves indicate mixing angle bounds given by original interpretation of PS191 experiment, but we *do not* use them to derive our final results, as explained in Sec. 2.4.3. The bounds are shown for the Majorana neutrino and are therefore two times *stronger* (see Section 2.4.4), while in the original works [125, 126] a single Dirac neutrino has been considered.

2.5 Results

In this Section we summarize our results: the upper bound on the (combination of) mixing angles of sterile and active neutrinos in the see-saw models (2.1) in the range 10 MeV – 2 GeV and the lower bound on sterile neutrino lifetime, obtained in combination of these bounds with constraints, coming from neutrino oscillation data.

2.5.1 Bounds on the mixing angles of sterile neutrinos

For the models (2.4) (two Majorana sterile neutrinos, interacting through both charged and neutral interactions), the compilation of constraints on various combinations of active-sterile mixing angles (ϑ_e^2, ϑ_μ^2, $\vartheta_e\sqrt{\sum c_\alpha \vartheta_\alpha^2}$, $\vartheta_\mu\sqrt{\sum c_\alpha \vartheta_\alpha^2}$) that we used in this study are plotted in Figs. 2.6 and 2.7.[13]

2.5.2 The lower bound on the lifetime of sterile neutrinos

The result of the Sections 2.3.2–2.3.3, combined with these experimental bounds can be translated into the *lower* limits on the lifetime of sterile neutrinos. These

---

[13] Notice that in the published results of the PS191 experiment [126] bounds are given up to $M_s = 400$ MeV. We extend these bounds up to 450 MeV, using the PhD Thesis of J.-M. Levy [146].

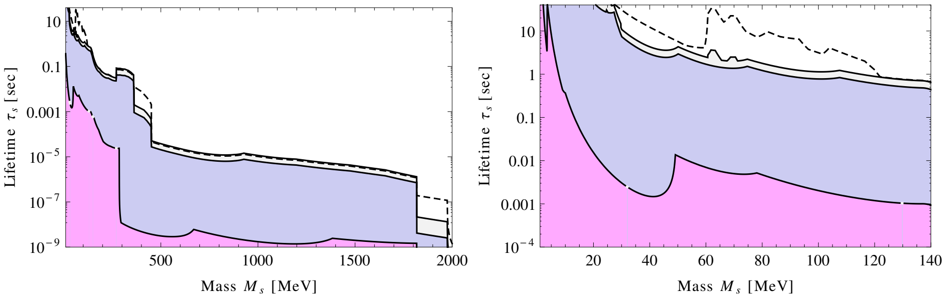

(a) Normal hierarchy, mass range 10 MeV – 2 GeV (b) Normal hierarchy, zoom at the mass range 10 MeV – 140 MeV

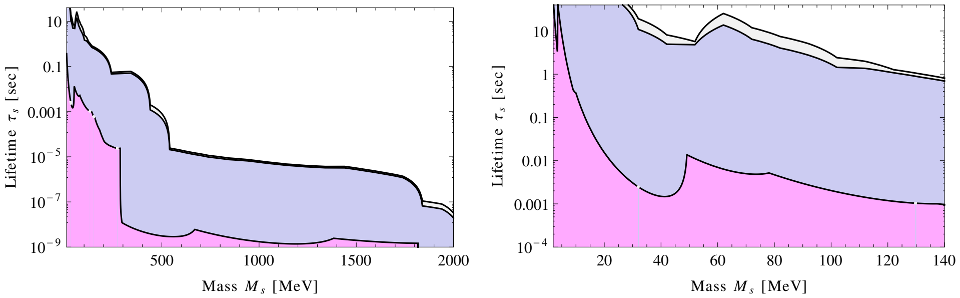

(c) Inverted hierarchy, mass range 10 MeV – 2 GeV (d) Inverted hierarchy, zoom at the mass range 10 MeV – 140 MeV

Figure 2.8: The resulting lower bounds on sterile neutrino lifetime τ_s as a function of their mass, obtained by requiring that two Majorana sterile neutrinos are responsible for neutrino oscillations and their parameters do not contradict the negative results of direct experimental searches. In all figures the upper curve comes from using of the best fit neutrino oscillation parameters, the middle one – from their variation within the 3σ limits, and the lower one does not take into account neutrino oscillation data and puts all three mixing angles equal to their direct experimental bounds. The dashed line for NH corresponds to the best-fit values of PMNS parameters with $\theta_{13} = 0$ and shows how much the bounds on the lifetime relax for non-zero value of θ_{13} (see text, Section 2.5 for discussion).

results are presented in Figs. 2.8 on the preceding page. Additionally, we plot the lifetime bounds for the best-fit values of the PMNS parameters yet with $\theta_{13} = 0$ (as used e.g. in [108, 147]). For normal hierarchy we see that our bounds with $\theta_{13} \neq 0$ are relaxed by as much as the order of magnitude at some masses, compared to $\theta_{13} = 0$ case. The difference for IH is not so pronounced. *Notice*, that the bounds of [108, 147, 112] were different from what we show as dashed line in Fig. 2.8 because of ignoring the neutral current contributions to the results of PS191 experiment (for details see discussion in Section 2.4 and Figs. 2.3, 2.4).

2.6 Discussion

In this Chapter, we have investigated experimental restrictions on the parameters of the see-saw Lagrangian in the case when two sterile neutrinos with the masses between ~ 10 MeV and 2 GeV are responsible for neutrino oscillations. Combined with the results of the direct experimental searches, the neutrino oscillation data provide stringent lower bounds on their lifetime, τ_s and allows to determine both *maximum* and *minimum* values of the mixing angles ϑ_α^2.

We have reinterpreted the results of the PS191 experiment [125, 126], following [144], by taking into account not only charged, but also neutral-current interactions (as both of these are present in the Type I see-saw Lagrangian). Our results demonstrated that below the mass of the pion the fixed target experiments (ϑ^4 experiments) provide *stronger* restrictions than the peak search experiments (ϑ^2 experiments) in case of *normal hierarchy*. In *inverted hierarchy* the reanalysis of the PS191 experiment turns out to be very important as well. In the original analysis of the CHARM experiment [129] neutral-current contributions were neglected as well and we have reinterpreted these results in a similar way to PS191. The final results are presented in Figs. 2.8.

Future experiments (for example, the SHiP experiment at CERN [100, 101, 102], see Sec. 1.3.9) have a great potential of discovering light neutral leptons of the νMSM or significantly improving the bounds on their parameters (see discussion in [148] and [149]). Due to the strong suppression of the mixing angles ϑ_e^2 in the case of NH and ϑ_μ^2 in the case of IH, the peak searches in the kaon decays (such as e.g. [150]) may miss the sterile neutrino (cf. [112]).[14]

As we have discussed in Sec. 1.3.3, the out-of-equilibrium behaviour of sterile neutrinos may lead as well to the successful baryogenesis scenario [153, 119, 147]; the generation of large lepton asymmetry at temperatures below the sphaleron freeze-out [109]. In Fig. 2.9 we superimpose the bounds on $|z|$, coming from the direct experimental searches on the region of parameters ($|z|$, M_s) in which the successful baryogenesis is possible (the region inside the black contours marked "BAU" based on the Ref. [147]).

---

[14] GeV-scale sterile neutrinos in the models with extended Higgs sector [151] can be searched at the LHC [152].

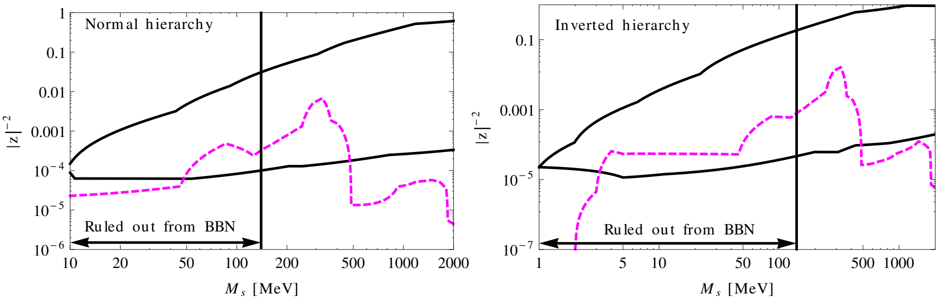

Figure 2.9: The region of successful baryogenesis in the νMSM compared with the experimental upper bounds on the parameter $|z|$. The vales of M_s and $|z|$, lying inside the black solid lines lead to the production of the observable baryon asymmetry (from [147]). The magenta dashed line marks is the *lower* bound on $|z|^{-2}$ (parameter, called ϵ in [109, 147]) such that for smaller values at least one of the mixing angles ϑ_α^2 is in contradiction with direct experimental searches (for the best-fit values of the PMNS mixing angles and masses). The value of $|z|$ corresponding to the bound is what we refer to as $z_{\max}$ in Sec. 2.3.5. The region to the left of $M_s = 140\,\mathrm{MeV}$ is ruled out from comparison with primordial nucleosynthesis bounds (Fig. 3.13).

Chapter 3

Influence of sterile neutrinos on primordial nucleosynthesis

3.1 Introduction: Particle physics processes in the expanding Universe

The characteristic feature of the physical processes in the early Universe is a peculiar interplay of gravity and microscopic physics. Gravity introduces the *Hubble time parameter* $\tau_H = H^{-1}$ (H is the Hubble expansion rate, see Eq. (3.2) for the definition) that indicates the timescale on which the global properties of the Universe (geometry, temperature, etc.) change significantly. The Hubble time is determined solely by the energy density of the matter filling the space. The microscopic matter constituents, particles, are involved in the interaction processes, that are believed to be described fundamentally by three known forces — electromagnetic, weak and strong. According to our discussion in Sec. 1.3.1, as long as the timescale τ of any given microscopic physical process is much smaller than τ_H, the expansion can be neglected on that timescale. If time τ is enough to establish thermal equilibrium between the particles, then the equilibrium it maintained in the course of the Universe expansion, while $\tau \ll \tau_H$ holds. When this inequality ceases to hold, the state of equilibrium is lost. The main reason for that is that interparticle distances become larger, hence interactions are less likely to occur.

3.1.1 Big Bang Nucleosynthesis

In this Chapter we are considering the formation of light nuclei in the primordial environment – Big Bang Nucleosynthesis (BBN). All three fundamental interactions are important for this phenomenon, all playing different roles. Charged particles together with photons are subject to electromagnetic forces and the equilibration timescale of corresponding processes is tiny with respect to the expansion time. Therefore these particles are kept in thermal equilibrium at the common temperature T. Due to expansion the temperature is *decreasing* with time, the Universe cools down. The equilibration time of the weak interactions changes abruptly so that at $T \gtrsim$ few MeV weakly interacting neutral particles (neutrinos and neutrons) stay in equilibrium, while at lower temperatures they fall out of it (freeze out).

At high temperatures processes like $n + \nu_e \to p + e^-$ maintain the so-called *chemical* equilibrium, that is the neutron-to-proton conversion exhibits the same finite intensity as the opposite process. Chemical and thermal equilibria are interconnected, so they are lost simultaneously, when neutron-to-proton ratio freezes out. Finally, the strong interactions are responsible for the production of nuclei comprising more than one nucleon. The most important fusion reaction for the formation of the first nucleus, deuteron, $n + p \to D$, *releases* energy of at least the binding energy of deuteron $E_D \approx 2.2\,\mathrm{MeV}$, and proceeds effectively in dense primordial medium. At temperatures of the order of E_D, however, energetic photons collide with deuteron and lead to its destruction (this process is called photodissociation). As baryon density is much lower than the density of photons (see Eq. (1.2)), there are *many* photons with energies much higher than E_D that collide with deuterons and hence postpone the production of the significant deuteron density until the temperature when the photodissociation is not effective anymore, $T \simeq 80\,\mathrm{keV}$, which is much lower than the binding energy. The net abundance of deuterium is, however, non-zero at all times till this moment and is given by the equilibrium Boltzmann distribution. Deuterium that is created at lower temperatures, serves as a fuel for the formation of ^{3}He, ^{4}He and other nuclides.

Although the times of elements' production and the moment of the departure from the chemical $p - n$ equilibrium are well-separated, the former process is very sensitive to the latter. Firstly, the details of the freeze-out set the ratio of the neutron to proton densities, and secondly, the time elapsed between the two moments determines the fraction of neutrons that have decayed since then (recalling that neutron is an unstable particle).

The seminal ideas of the primordial synthesis of light elements were first outlined in the so-called $\alpha\beta\gamma$ paper, [154], published in the late 1940s. Since then the theory of the Big Bang Nucleosynthesis has evolved and its main predictions were confirmed, making it a well-developed model from both theoretical and observational points of view. A lot of reviews of the standard BBN scenario and its implication for particle physics models exist (see e.g. [155, 53, 54]).

3.1.2 Influence of decaying particles on primordial nucleosynthesis

In this Chapter we investigate the influence of *sterile neutrinos* on primordial nucleosynthesis. Massive sterile neutrinos can decay, but due to their feeble interaction strength their lifetime can be of order seconds. The decay products of the sterile neutrinos are injected into the primordial environment, increasing its temperature and shifting the p-n equilibrium.

Several works had previously considered the influence of MeV-scale particles on primordial nucleosynthesis. Compared to the Refs. [156, 157], the present study accounts for the neutrino flavour oscillations in the plasma and employs more accurate strategy of solving Boltzmann equations, which results in the revision of the bounds of [156, 157] (see Section 3.5 for detailed comparison). The authors of [158] developed a new code that can perform treatment of active and sterile neutrinos with arbitrary distribution functions, non-zero lepton asymmetry, etc. However, as of time of writing this code has not been made publicly available and the Ref. [158] did not derive bounds on sterile neutrino parameters. A number of other works ([159, 160, 161, 162, 163]) analyzed the influence of decaying MeV particles on BBN. We compare with them in the corresponding parts of the Chapter.

The structure of this Chapter

We explain the modifications of the standard BBN computations due to the presence of sterile neutrinos in the plasma and describe our numerical procedure in Sec. 3.2. In Sec. 3.3 we describe tests of this numerical procedure. The results are summarized in Sec. 3.4. We conclude in Sec. 3.5.

3.2 Primordial nucleosynthesis with sterile neutrinos

The section below summarizes our setup for the BBN analysis with decaying particles. The notations and conventions closely follow the series of works [157, 164, 165].

We will be interested only in the tree-level interactions of sterile neutrinos with the primordial plasma. In this case the interaction is fully determined by the squares of their mixing angles. We will consider two Majorana particles each having 2 degrees of freedom, corresponding to two possible helicity states and three *active-sterile mixing angles* ϑ_α^2.

We consider in this Chapter only sterile neutrinos with the masses in the range $1\,\mathrm{MeV} < M_s < M_\pi \approx 140\,\mathrm{MeV}$. For heavier particles, two-particle decay channels appear (e.g. $N \to \pi_0 \nu_\alpha, \pi^\pm e^\mp$) and our procedure of solving Boltzmann equations (described below) should be significantly modified. The lower bound was chosen to be around 1 MeV by the following considerations. In this mass range, the sterile neutrino lifetime τ_s (Eq. (2.1)) becomes explicitly [108]

$$\begin{aligned}\tau_s^{-1} = \Gamma_s &= \frac{G_F^2 M_s^5}{96\pi^3}\left[(1+\tilde{g}_L^2+g_R^2)(\vartheta_\mu^2+\vartheta_\tau^2)+(1+g_L^2+g_R^2)\vartheta_e^2\right]\\ &\approx 6.9\ \text{sec}^{-1}\left(\frac{M_s}{10\ \text{MeV}}\right)^5\left[1.6\,\vartheta_e^2+1.13(\vartheta_\mu^2+\vartheta_\tau^2)\right]\end{aligned} \tag{3.1}$$

where θ_W is the Weinberg's angle and $g_R = \sin^2\theta_W \approx 0.23$, $g_L = \frac{1}{2}+\sin^2\theta_W$, $\tilde{g}_L = -\frac{1}{2}+\sin^2\theta_W$.[1] From this expression one sees that sterile neutrinos lighter than about 2 MeV have lifetime of at least several hundred seconds even for very large mixing angles $\vartheta \sim 1$. Therefore, such particles survive till the onset of the BBN, and freeze-out at temperatures $T \sim 2-3$ MeV. They would be relativistic at that time, i.e. their average momentum would be of the order of temperature, $\langle p\rangle \sim T$, and their contribution to the number of relativistic neutrino species would be significant, $\Delta N_{\text{eff}} \simeq 2$. In the course of the Universe expansion $\langle p\rangle$ would scale as temperature due to the gravitational redshift, and at some point would become smaller than the mass of sterile neutrino. At that moment the energy density of sterile neutrinos would start to change with expansion as a^{-3} rather than a^{-4} (where a is a scale-factor) so that the contribution of these massive particles to the energy density would quickly become dominant, making $N_{\text{eff}} \gg 1$ before the production of light elements starts. It contradicts the current bound that puts $N_{\text{eff}} = 3.74^{+0.8}_{-0.7} \pm 0.06(\text{syst})$ at 2σ [166].[2]

Additionally, in the νMSM the successful baryogenesis is possible only for the masses of sterile neutrinos *above* few MeV [119, 147]. Therefore we restrict the analysis to the region of masses higher than 1 MeV.

3.2.1 Expanding Universe and distributions of particles

We consider expansion of the homogeneous and isotropic Universe with the flat Friedmann–Robertson–Walker metric in the form $ds^2 = dt^2 - a^2 d\vec{x}^2$, where $a = a(t)$ is a time-dependent scale factor, whose evolution is described by the Friedmann equation

$$H \equiv \frac{\dot{a}}{a} = \sqrt{\frac{8\pi G_N}{3}\rho}\ , \tag{3.2}$$

where H is the Hubble expansion rate. The total energy density ρ is the sum of all the energy densities present in the medium, and G_N is the Newton's constant. The energy density together with the total pressure p satisfy the "energy conservation" law

$$a\frac{d\rho}{da} + 3(p+\rho) = 0, \tag{3.3}$$

---

[1] The expression (3.1) is for Majorana particle. For Dirac particle the lifetime would be twice larger.

[2] Here the systematic error is due to the different values of neutron lifetime between the average value from Particle Data group, [167] and the recent measurement of [168].

which is actually the second Friedmann equation. At the temperatures of interest the dominant components of the plasma are photons γ, electrons and positrons $e^{\pm}$, three flavours of active neutrinos $(\nu_e, \nu_\mu, \nu_\tau)$ and sterile neutrinos.[3] Working with the particle kinematics in the expanding Universe it is convenient to use *conformal momentum* y instead of the usual physical momentum p. The two are related through $y = pa$. The quantitative description of the plasma population is provided by the distribution functions f_α, that are the numbers of particles α per "unit cell" of the phase space $d^3p\, d^3x = (2\pi)^3$. At keV–MeV temperatures the medium is homogeneous and the distribution functions are independent of spatial coordinates of particles, and due to isotropy f_α do not depend on the direction of the particle momentum. That simplifies the description of their evolution and therefore

$$\frac{df}{dt} \equiv \left(\frac{\partial f}{\partial t} - Hp\frac{\partial f}{\partial p}\right) = \frac{\partial f(t,y)}{\partial t} \tag{3.4}$$

holds. The goal is to find the time evolution of the distribution functions of all relevant particles and to use them to compute the energy density and pressure as a function of time and scale-factor, closing the system of Eqs. (3.2)–(3.3) via

$$\rho = \sum_i \frac{g_i}{2\pi^2}\int f_i E_i p^2 dp \quad ; \quad p = \sum_i \frac{g_i}{6\pi^2}\int f_i \frac{p^4}{E_i} dp \tag{3.5}$$

Here the summation goes over all plasma particles, g_i, m_i is the number of degrees of freedom and mass of i-th particle respectively, $E_i = \sqrt{p^2 + m_i^2}$.

If interaction rate of the particles is much faster than the Hubble expansion rate, their distribution functions are given by either the Bose-Einstein, or the Fermi-Dirac distributions. This is the case for photons, electrons and positrons — that are kept in equilibrium due to intensive electromagnetic interactions

$$f_\gamma = \frac{1}{e^{E/T} - 1}, \quad f_e = \frac{1}{e^{E/T} + 1}. \tag{3.6}$$

The contribution of these particles to the energy and pressure in Eqs. (3.2), (3.3) is hence determined by the single parameter – temperature. However, to describe the contributions of the other particles one has to solve *kinetic* equations involving them (see Secs. 3.2.3–3.2.5 below).

3.2.2 Baryonic matter

The contribution of the baryonic matter to the evolution of the hot plasma of relativistic species is proportional to the baryon-to-photon ratio η_B (Eq. (1.2)). Since this value is very small, baryons are present in negligible amount before and

---

[3] Muons may appear in plasma from the decays of the sterile neutrinos with $M_s > 106\,\mathrm{MeV}$. See Sec. 3.2.5 for details.

during the BBN, and do not influence the dynamics of the remaining medium. This allows to analyze our problem in two steps. At STEP I we omit baryonic species and study how the temperature of the plasma, the expansion factor and neutrino distributions evolve in time from temperatures of the order of 100 MeV, when sterile neutrinos typically start to go out of equilibrium,[4] down to $T_{\rm Fin} \simeq 10\,\mathrm{keV}$ when nuclear fusion reactions have ended. At STEP II we use these results to determine the outcome of the nuclear reaction network against the background of evolving electromagnetic plasma (Sec. 3.2.6).

3.2.3 Active neutrinos at MeV temperatures

Weak interactions are not able to maintain the thermal equilibrium of active neutrinos with the plasma during all the expansion period we consider. A simple comparison of the weak collision rate $G_F^2 T^5$ and $H(T)$ tells that neutrino maintain their equilibrium with the rest of the plasma down to temperatures $T_{\rm dec} \sim$ few MeV. The process of neutrinos going out of equilibrium is usually referred to as *neutrino decoupling*. Throughout this Chapter we assume that *no* lepton asymmetry is present so that the number of neutrinos is equal to the number of antineutrinos.[5] At temperatures higher than $T_{\rm dec}$ the distribution is therefore given by the Fermi-Dirac one, while at lower temperatures we have to solve the set of three Boltzmann equations

$$\frac{df_{\nu_\alpha}}{dt} = I_\alpha, \quad \alpha = e, \mu, \tau \tag{3.7}$$

The details of the interactions, such as particle collisions, are encoded in the so-called collision terms I_α. The terms are explicitly [173]

$$I_\alpha = \frac{1}{2E_\alpha} \sum_{\rm in,out} \int S|\mathcal{M}|^2 F[f](2\pi)^4 \delta^4(p_{\rm in} - p_{\rm out}) \prod_{i=2}^{Q} \frac{d^3 p_i}{(2\pi)^3 2E_i} \tag{3.8}$$

The sum runs over all the possible initial states "in" involving ν_α (represented by a particle set ν_α, 2, 3, $\ldots$, K) and the final states "out" ($K+1$, $\ldots$, Q). Matrix element $\mathcal{M}$ corresponds to the probability of the transition "in"–"out" to occur and the delta-function ensures the conservation of 4-momentum $p_{\rm in} = p_{\rm out}$. Symmetrization factor S is equal to 1, except of the transitions involving identical particles either in initial or in a final state. Relevant matrix elements together with the symmetrization factors are listed in Table 3.1. The interaction rates are dependent on the population of the medium, and the functional $F[f]$ describes this. In case when all the incoming and outgoing particles are fermions,

$$F[f] = (1-f_{\nu_\alpha})\ldots(1-f_K)f_{K+1}\ldots f_Q - f_{\nu_\alpha}\ldots f_K(1-f_{K+1})\ldots(1-f_Q). \tag{3.9}$$

---

[4] The exact "freeze-out" temperature depends on the mixing angle.

[5] For the previous studies of the BBN outcomes *with* the lepton asymmetry present see e.g. [169, 170, 171, 158, 172].

Process $(1+2 \to 3+4)$	S	$SG_F^{-2}\lvert\mathcal{M}\rvert^2$
$\nu_\alpha + \nu_\beta \to \nu_\alpha + \nu_\beta$	1	$32(p_1 \cdot p_2)(p_3 \cdot p_4)$
$\nu_\alpha + \bar{\nu}_\beta \to \nu_\alpha + \bar{\nu}_\beta$	1	$32(p_1 \cdot p_4)(p_2 \cdot p_3)$
$\nu_\alpha + \nu_\alpha \to \nu_\alpha + \nu_\alpha$	1/2	$64(p_1 \cdot p_2)(p_3 \cdot p_4)$
$\nu_\alpha + \bar{\nu}_\alpha \to \nu_\alpha + \bar{\nu}_\alpha$	1	$128(p_1 \cdot p_4)(p_2 \cdot p_3)$
$\nu_\alpha + \bar{\nu}_\alpha \to \nu_\beta + \bar{\nu}_\beta$	1	$32(p_1 \cdot p_4)(p_2 \cdot p_3)$
$\nu_e + \bar{\nu}_e \to e^+ + e^-$	1	$128[g_L^2(p_1 \cdot p_4)(p_2 \cdot p_3)+$ $g_R^2(p_1 \cdot p_3)(p_2 \cdot p_4) + g_L g_R m_e^2 (p_1 \cdot p_2)]$
$\nu_e + e^- \to \nu_e + e^-$	1	$128[g_L^2(p_1 \cdot p_2)(p_3 \cdot p_4)+$ $g_R^2(p_1 \cdot p_4)(p_2 \cdot p_3) - g_L g_R m_e^2 (p_1 \cdot p_3)]$
$\nu_e + e^+ \to \nu_e + e^+$	1	$128[g_L^2(p_1 \cdot p_4)(p_2 \cdot p_3)+$ $g_R^2(p_1 \cdot p_2)(p_3 \cdot p_4) - g_L g_R m_e^2 (p_1 \cdot p_3)]$
$\nu_{\mu(\tau)} + \bar{\nu}_{\mu(\tau)} \to e^+ + e^-$	1	$128[\tilde{g}_L^2(p_1 \cdot p_4)(p_2 \cdot p_3)+$ $g_R^2(p_1 \cdot p_3)(p_2 \cdot p_4) + \tilde{g}_L g_R m_e^2 (p_1 \cdot p_2)]$
$\nu_{\mu(\tau)} + e^- \to \nu_{\mu(\tau)} + e^-$	1	$128[\tilde{g}_L^2(p_1 \cdot p_2)(p_3 \cdot p_4)+$ $g_R^2(p_1 \cdot p_4)(p_2 \cdot p_3) - \tilde{g}_L g_R m_e^2 (p_1 \cdot p_3)]$
$\nu_{\mu(\tau)} + e^+ \to \nu_{\mu(\tau)} + e^+$	1	$128[\tilde{g}_L^2(p_1 \cdot p_4)(p_2 \cdot p_3)+$ $g_R^2(p_1 \cdot p_2)(p_3 \cdot p_4) - \tilde{g}_L g_R m_e^2 (p_1 \cdot p_3)]$

Table 3.1: Squared matrix elements for weak processes involving active species only. S is the symmetrization factor; $\alpha, \beta = e, \mu, \tau$. In all processes we take $\alpha \neq \beta$. The results coincide with those of Ref. [165].

When some of particles are bosons, one has to replace $(1 - f_R)$ by $(1 + f_R)$ for every bosonic particle R.

However, in the next Section (3.2.4)), we argue that the phenomenon of neutrino oscillations should be taken into account in the present picture, and discuss the modification of the Boltzmann equations.

3.2.4 Inclusion of neutrino oscillations

The active neutrinos of different flavours ν_e, ν_μ, ν_τ are related to the mass eigenstate basis ν_1, ν_2, ν_3 via a non-diagonal Pontecorvo-Maki-Nakagava-Sakata (PMNS) matrix V, $|\nu_\alpha\rangle = \sum V_{\alpha i}|\nu_i\rangle$ (see Eq. (2.6)). Exact treatment of active neutrino oscillation in the early Universe is a difficult task (see e.g. [174, 175, 176]) Characteristic timescale of oscillation between i and j mass eigen-states for a neutrino with energy E is [177]

$$\tau_{ij} = \frac{4\pi E}{|m_i^2 - m_j^2|} \approx 8.3 \times 10^{-6}\mathrm{s}\ \frac{E}{\mathrm{MeV}}\ \frac{10^{-3}\,\mathrm{eV}^2}{|m_i^2 - m_j^2|} \tag{3.10}$$

Average energy of relativistic Fermi particles in equilibrium is $\langle E \rangle = 3.15T$ [173]. Applying this relation to active neutrinos and using their measured mass differences [123] $m_2^2 - m_1^2 \approx 7.6 \times 10^{-5}\,\mathrm{eV}^2$, $|m_3^2 - m_1^2| \approx 2.5 \times 10^{-3}\,\mathrm{eV}^2$, we obtain

$$\tau_{12} \approx 1.0 \times 10^{-3}\,\mathrm{sec}\frac{T}{3\,\mathrm{MeV}}\ , \quad \tau_{13} \approx 3.1 \times 10^{-5}\,\mathrm{sec}\frac{T}{3\,\mathrm{MeV}}\ , \tag{3.11}$$

provided that influence of the surrounding environment on neutrino propagation is neglected. One sees therefore that around the moment when active neutrino decouples, $T \simeq 3$ MeV, typical oscillation timescales are much smaller than the Hubble expansion time given by Eq. (3.2)

$$\tau_H = \sqrt{\frac{15}{4\pi^3 g_* G_N T^4}} \simeq 0.16\,\mathrm{sec}\left(\frac{3\,\mathrm{MeV}}{T}\right)^2 \ . \tag{3.12}$$

Here we have plugged $g_* \approx 11$ (at $T \sim$ MeV) [173] is the so-called number of relativistic species that enters energy-temperature relation $\rho = \frac{\pi^2 g_* T^4}{30}$. Therefore, active neutrinos oscillate many times between the subsequent reactions involving them. In quantitative terms it means that probabilities $P_{\alpha\beta}$ to transform from flavour α to flavour β are oscillating functions of time. In realistic situation neutrinos do not have a definite momentum but are created in wave packets that are superpositions of states which have definite momentum. Since oscillation periods are momentum-dependent according to Eq. (3.10), each state in the superposition will have his own period. Therefore after sufficiently many periods the initial phases characterizing superposition will change, and there is no reason for the phase changes to be correlated with each other anymore. So the decoherence of states is what happens. This phenomenon can be described effectively by averaging transition probabilities $P_{\alpha\beta}$ over time. Resulting expressions are [177]

$$P_{ee} = 1 - \frac{1}{2}(\sin^2 2\theta_{13} + \cos^4\theta_{13}\sin^2 2\theta_{12}) \tag{3.13a}$$

$$P_{e\mu} = P_{\mu e} = \frac{1}{2}\cos^2\theta_{13}\sin^2 2\theta_{12} \tag{3.13b}$$

$$P_{e\tau} = P_{\tau e} = \sin^2\theta_{13}\cos^2\theta_{13}\left(2 - \frac{1}{2}\sin^2 2\theta_{12}\right) \tag{3.13c}$$

$$P_{\mu\mu} = 1 - \frac{1}{2}\sin^2 2\theta_{12} \tag{3.13d}$$

$$P_{\mu\tau} = P_{\tau\mu} = \frac{1}{2}\sin^2\theta_{13}\sin^2 2\theta_{12} \tag{3.13e}$$

$$P_{\tau\tau} = 1 - \sin^2\theta_{13}\left(2\cos^2\theta_{13} + \frac{1}{2}\sin^2\theta_{13}\sin^2 2\theta_{12}\right) \tag{3.13f}$$

To understand what happens with a neutrino, consider example of the electron neutrino created in electron-positron annihilation. At the production time this particle has probability 1 to oscillate into ν_e and zero for other final state. After long enough time for many oscillations to happen and before the time when a collision with other particle becomes quite probable, the decoherence comes into play. So now we may find the ν_e with probability P_{ee}, ν_μ with probability $P_{e\mu}$ and ν_τ with $P_{e\tau}$. The production rate of the initial specimen per unit time is proportional to collision integral I_e, according to the Boltzmann equation (3.7). But the actual number of produced electron neutrinos is reduced by factor P_{ee}. And even if we imagine hypothetical situation when muon neutrino does not interact with plasma, this particle will be anyway produced effectively in oscillations, at rate $P_{e\mu}I_e$. Generalization to other neutrino flavours leads us to conclusion that the Boltzmann equation (3.7) becomes modified,

$$\frac{df_\alpha}{dt} = \sum P_{\alpha\beta}I_\beta. \tag{3.14}$$

For the actual computations we use the following experimental best-fit values: $\sin^2\theta_{12} = 0.31$, $\sin^2\theta_{23} = 0.52$ from [123], and $\sin^2 2\theta_{13} = 0.09$ from the Daya Bay [10]. The latter number is close to the result $\sin^2 2\theta_{13} = 0.11$ measured in another recent experiment, RENO [9].

However, in dense medium oscillations proceed differently due to considerable effects of the plasma on properties of a single particle. The oscillations of active neutrinos into active neutrinos can be described similarly to what was done for active-sterile oscillations in Sec. 1.3.1. Namely, the effective Hamiltonian of the system of three neutrinos is described by the addition of medium potential ΔH_M to the Hamiltonian H_V of the system in vacuum [178]

$$H_M = H_\mathrm{V} + \Delta H_M, \quad H_\mathrm{V} = \frac{1}{2E}V^*\mathrm{diag}(m_1^2, m_2^2, m_3^2)V^\dagger\ , \tag{3.15}$$

where E is the neutrino energy. Diagonalization of the total propagation Hamiltonian H_M gives effective active neutrino masses and mixings.

The medium potential comprises effects of neutrino interactions. Since neutrinos take part only in charged- and neutral-current interactions, matter potential has two terms ΔH_{CC} and ΔH_{NC}, respectively. All neutrinos couple to neutral currents identically, so ΔH_{NC} is proportional to unit matrix. Therefore this term just shifts the energy of all neutrinos by the same amount, and does not affect oscillations. In contrast, the charged-current term is present only for ν_e. The reason is that due to high concentration of electrons in plasma, ν_e couples effectively to charged currents, while at temperatures below the muon's mass there is no significant contribution of muons and tau-leptons to realize charged-current coupling of other neutrino flavours.

Explicitly the matter potential is [177]

$$\Delta H_{CC} = -\frac{14\sqrt{2}G_F}{45M_W^2}\; E\; T^4 \;\mathrm{diag}(1,0,0) \tag{3.16}$$

in the flavour neutrino basis $(\nu_e, \nu_\mu, \nu_\tau)$. M_W is the mass of the W-boson.

3.2.5 The impact of sterile neutrinos

As already mentioned, sterile neutrinos interact much more feebly than active neutrinos do. Nevertheless, at some high temperature sterile neutrinos may enter thermal equilibrium. As we have discussed in Sec. 1.3, in the νMSM model, sterile neutrinos come into equilibrium at temperature T_+ (typically $T_+ = 10 \div 100$ GeV) and freeze-out at temperatures $T_- \sim 0.5 - 5$ GeV [109]. Afterwards, sterile neutrinos decay into active neutrinos and other particles. The energies of the decay products may be very different from the typical energies of plasma particles. For particles that equilibrate quickly (such as electrons or photons), this "injection" results in the fast redistribution of the energy between all particles in equilibrium and effectively the process looks like a temperature increase (more precisely, it just slows down the cooling of the Universe). But for particles that either are not in equilibrium or are about to fall out of it, such as active neutrinos at few MeV, the "injection" *modifies* the form of their spectra. The other mass-induced effect is that sterile neutrinos may switch from the relativistic regime (when their average momentum is larger than mass) that is established at large temperatures, to the non-relativistic one, due to the gravitational redshift.

For the quantitative description of sterile neutrino dynamics we utilize the Boltzmann equation similar to (3.7), replacing active neutrino everywhere therein by sterile neutrino

$$\frac{df_S}{dt} = I_S \tag{3.17}$$

Reactions contributing to the right-hand side together with their probabilities are listed in Tables 3.2– 3.3 on page 80. In these Tables, averaging over helicities of incoming particles and summation over those of outgoing products is assumed. The reactions are considered for two cases. In the first one sterile neutrino is a right-chiral Majorana neutrino that has 2 helicity degrees of freedom. That is actually the case in our problem, where we have two neutrinos of this kind. The other case corresponds to sterile neutrino of Dirac nature. Dirac fermions have both right- and left-chiral components, hence yielding 4 degrees of freedom in total. Expressions listed in Tables 3.2, 3.3 are applicable for both cases of the neutrino nature. Moreover, to complete the list of possible tree-level reactions, one has to consider charge-conjugated channels and take into account that Dirac particle is distinct from its antiparticle, while Majorana neutrino is not. The resulting expressions coincide with [165, 156].

Process $(1+2 \to 3+4)$	S	$SG_F^{-2}\,\lvert\mathcal{M}\rvert^2$
$N+\nu_\beta \to \nu_\alpha+\nu_\beta$	1	$32\vartheta_\alpha^2(p_1\cdot p_2)(p_3\cdot p_4)$
$N+\bar\nu_\beta \to \nu_\alpha+\bar\nu_\beta$	1	$32\vartheta_\alpha^2(p_1\cdot p_4)(p_2\cdot p_3)$
$N+\nu_\alpha \to \nu_\alpha+\nu_\alpha$	1/2	$64\vartheta_\alpha^2(p_1\cdot p_2)(p_3\cdot p_4)$
$N+\bar\nu_\alpha \to \nu_\alpha+\bar\nu_\alpha$	1	$128\vartheta_\alpha^2(p_1\cdot p_4)(p_2\cdot p_3)$
$N+\bar\nu_\alpha \to \nu_\beta+\bar\nu_\beta$	1	$32\vartheta_\alpha^2(p_1\cdot p_4)(p_2\cdot p_3)$
$N+\bar\nu_e \to e^++e^-$	1	$128\vartheta_e^2[g_L^2(p_1\cdot p_4)(p_2\cdot p_3)+$ $g_R^2(p_1\cdot p_3)(p_2\cdot p_4)+g_Lg_Rm_e^2(p_1\cdot p_2)]$
$N+e^- \to \nu_e+e^-$	1	$128\vartheta_e^2[g_L^2(p_1\cdot p_2)(p_3\cdot p_4)+$ $g_R^2(p_1\cdot p_4)(p_2\cdot p_3)-g_Lg_Rm_e^2(p_1\cdot p_3)]$
$N+e^+ \to \nu_e+e^+$	1	$128\vartheta_e^2[g_L^2(p_1\cdot p_4)(p_2\cdot p_3)+$ $g_R^2(p_1\cdot p_2)(p_3\cdot p_4)-g_Lg_Rm_e^2(p_1\cdot p_3)]$
$N+\bar\nu_{\mu(\tau)} \to e^++e^-$	1	$128\vartheta_{\mu(\tau)}^2[\tilde g_L^2(p_1\cdot p_4)(p_2\cdot p_3)+$ $g_R^2(p_1\cdot p_3)(p_2\cdot p_4)+\tilde g_Lg_Rm_e^2(p_1\cdot p_2)]$
$N+e^- \to \nu_{\mu(\tau)}+e^-$	1	$128\vartheta_{\mu(\tau)}^2[\tilde g_L^2(p_1\cdot p_2)(p_3\cdot p_4)+$ $g_R^2(p_1\cdot p_4)(p_2\cdot p_3)-\tilde g_Lg_Rm_e^2(p_1\cdot p_3)]$
$N+e^+ \to \nu_{\mu(\tau)}+e^+$	1	$128\vartheta_{\mu(\tau)}^2[\tilde g_L^2(p_1\cdot p_4)(p_2\cdot p_3)+$ $g_R^2(p_1\cdot p_2)(p_3\cdot p_4)-\tilde g_Lg_Rm_e^2(p_1\cdot p_3)]$

Table 3.2: Squared matrix elements for *scatterings* of sterile neutrinos ν_S. Here S is the symmetrization factor; $\alpha, \beta = e, \mu, \tau$; $\alpha \neq \beta$. ϑ_α is the mixing angle of sterile neutrino with ν_α. The results are applicable for one right-chiral Majorana neutrino as well as for one Dirac neutrino, for details see text.

Note that we neglect the processes involving baryonic particles. However, they become important for temperatures near the QCD crossover temperature $T_{QCD} \simeq 200$ MeV, when the density of these particles is not negligible anymore.

Process $(1 \to 2+3+4)$	S	$SG_F^{-2}\left\|\mathcal{M}\right\|^2$
$\nu_S \to \nu_\alpha + \nu_\beta + \bar{\nu}_\beta$	1	$32\ \vartheta_\alpha^2 (p_1 \cdot p_4)(p_2 \cdot p_3)$
$\nu_S \to \nu_\alpha + \nu_\alpha + \bar{\nu}_\alpha$	1/2	$64\ \vartheta_\alpha^2 (p_1 \cdot p_4)(p_2 \cdot p_3)$
$\nu_S \to \nu_e + e^+ + e^-$	1	$128\ \vartheta_e^2 [g_L^2 (p_1 \cdot p_3)(p_2 \cdot p_4) + g_R^2 (p_1 \cdot p_4)(p_2 \cdot p_3) + g_L g_R m_e^2 (p_1 \cdot p_2)]$
$\nu_S \to \nu_{\mu(\tau)} + e^+ + e^-$	1	$128\ \vartheta_{\mu(\tau)}^2 [\tilde{g}_L^2 (p_1 \cdot p_3)(p_2 \cdot p_4) + g_R^2 (p_1 \cdot p_4)(p_2 \cdot p_3) + \tilde{g}_L g_R m_e^2 (p_1 \cdot p_2)]$

Table 3.3: Squared matrix elements for *decays* of sterile neutrinos ν_S. Here S is the symmetrization factor; $\alpha, \beta = e, \mu, \tau$; $\alpha \neq \beta$. ϑ_α is the mixing angle of sterile neutrino with ν_α. The results are both for Majorana and Dirac neutrinos, for details see text.

More scattering channels of sterile neutrino would appear and their proper account is involved. However it seems to be reasonable to assert that the only modification the account will bring is to *lower* the decoupling temperature of sterile neutrinos.

Oscillations between active and sterile neutrinos do not change significantly with respect to vacuum, therefore the Boltzmann equation in its original form (3.17) is still valid, contrary to what we have found out for active neutrinos. Indeed, using the approach of Sec. 1.3.1, one finds that their effective mixing angles in medium θ differ from that in vacuum θ_0 as

$$\frac{\theta - \theta_0}{\theta_0} \sim \frac{G_F T^5}{M_W^2 M_S^2} \sim 10^{-11} \times \left(\frac{T}{100\,\text{MeV}}\right)^6 \left(\frac{10\,\text{MeV}}{M_S}\right)^2 \tag{3.18}$$

for the small mixing angles θ_0 which we consider here. Therefore the active-sterile mixing angle is not altered.

When sterile neutrino is heavier than muon, the former particle can appear in the decay $N \to \mu^- + e^+ + \bar{\nu}_e$. However, the branching fraction of this decay mode does not even reach a percent for masses of sterile neutrino we consider (see e.g. [108]). Therefore we can neglect influence of both muons and other particles, appearing in the decay.

As a result we have six equations (3.2), (3.3), (3.14), and (3.17) describing primordial plasma at temperatures of interest. These equations contain six unknowns – scale factor $a(t)$, temperature $T(t)$ and four neutrino distribution functions, f_{ν_α} and f_S. The system of equations is therefore closed and we have solved it numerically at the STEP I.

3.2.6 Course of nuclear reactions

Outcome of the nuclear reaction chains is found numerically. For the Standard BBN model one of the earlier attempts was made with the code written by L.

Kawano [179, 180]. However, the program in its original form is inappropriate for the account of the BSM physics, and we modified it for the present analysis. Two technical remarks are in order here. First, we used the 1992 version of the program [180] as a starting point, and not the 1988 one, [179]. Therefore, the integration time steps were taken small enough, so that the integration procedure did not introduce an error that was compensated as a shift in the resulting value of the Y_p,[6] the so-called "Kernan correction" [181]. Second, the code did not take into account the Coulomb and the nucleon finite-mass corrections to weak interaction rates, as well as radiative and finite-temperature effects.[7] We do not calculate directly these effects, but assume their net result to be in the form of the additive correction, which we took to be $\Delta Y_p = -0.0003$ [185]. The tests described in Sec. 3.3.1 demonstrate an agreement of thus modified "Kawano code" with the results of the other code, PArthENoPE [186], that takes a proper account of these effects.

Presence of sterile neutrinos alters the standard dynamics of the temperature and the expansion rate as well as the rates of weak interactions involving neutrons and protons. These quantities are known from the STEP I, so we have implemented the import of these data. Together with the change of ΔY_p indicated above, it has lead to the code, that became an essential tool of STEP II in our approach. The computations of nuclide evolution start from temperatures of several MeV, when the chemical equilibrium ceases to hold, up to temperatures $T_{\rm Fin}$.

3.2.7 Adopted values of abundances of the light nuclei

The observables of the BBN are concentrations, or abundances, of light nuclides dispersed in the cosmos. The most relevant abundance in our problem is that of ^{4}He, as it is sensitive to the expansion rate of the Universe at MeV temperatures and neutrino distribution functions. The presence of sterile neutrinos in plasma typically increases the concentration of ^{4}He, described by Y_p. Accurate calculations carried out in the Standard Model [186] predict the values

$$Y_p^{\rm SBBN} = 0.2480 \qquad (\tau_n = 885.7 \text{ sec}) \tag{3.19}$$

$$Y_p^{\rm SBBN} = 0.2465 \qquad (\tau_n = 878.5 \text{ sec}) \tag{3.20}$$

depending on the lifetime of neutron, τ_n, see below.

There are two main methods of experimental determination of primordial Helium abundance. The first one is related to the studies of low-metallicity astrophysical environments and extrapolating them to zero metallicity case. The Y_p measurements are known to be dominated by systematic uncertainties. Therefore we adopt the Y_p values from the two most recent studies, Refs. [166, 187] that

---

[6] We denote by Y_p the *mass fraction* of the ^{4}He, that is a fraction of the total baryon mass stored in the form of Helium-4.

[7] For the accurate account of these corrections, see e.g. [155, 182, 183, 184].

have slightly different implications. For recent discussion of various systematic uncertainties in ^{4}He determination, see [188].

In Ref. [166] the value $Y_p = 0.2565 \pm 0.0010(\text{stat.}) \pm 0.0050(\text{syst.})$ was obtained. Therefore, the 2σ intervals that we adopt in our studies are[8]

$$Y_p = 0.2495 - 0.2635 \quad (\text{Ref. [166]}, 2\sigma \text{ interval}) \tag{3.21}$$

One notices that this result is more than 2σ away from the Standard Model BBN predicted value of Y_p, Eq. (3.19).

Using a subsample of the same data of [166], a different group had independently determined Y_p [187]. From their studies we adopt[9] $Y_p = 0.2574 \pm 0.0036(\text{stat.}) \pm 0.0050(\text{syst.})$. As a result,

$$Y_p = 0.2452 - 0.2696 \quad (\text{Ref. [187]}, 2\sigma \text{ interval}) \tag{3.22}$$

(this values of Y_p coincide with the Standard BBN one, (3.19), at about 1σ level).[10]

Second method of determination of Helium abundance is based on the CMB measurements. This method is believed to determine truly pristine value of Y_p, not prone to the systematics of astrophysical methods. However currently its uncertainties are still much larger than of the first method. The present measurements put it at

$$Y_p = 0.22 - 0.40, \quad N_{\text{eff}} = 3 \quad (\text{Refs. [190, 106]}, 2\sigma \text{ interval}) \tag{3.23}$$

again consistent with the Standard Model BBN at 1.5σ. Here N_{eff} is the so-called effective number of neutrino species

$$N_{\text{eff}} = \frac{120}{7\pi^2} \frac{\rho_{\nu_e} + \rho_{\nu_\mu} + \rho_{\nu_\tau}}{T^4}, \tag{3.24}$$

proportional to the ratio of the total energy, deposited into the active neutrino species to that of photons. Notice, that the bound (3.23) is based on assumption that before the onset of the recombination epoch the effective number of neutrino species is close to its SM value $N_{\text{eff}} \approx 3$. As we will see later, sterile neutrinos can significantly distort N_{eff}. For the values of N_{eff} strongly deviating from 3 the CMB bounds on Y_p gets modified. For example, the analysis carried out in [190] reveals that

$$Y_p = 0.10 - 0.33, \quad N_{\text{eff}} = 6 \quad (\text{Ref. [190]}, 2\sigma \text{ interval}). \tag{3.25}$$

The similar conclusion is reached if one employs the data of [191].

---

[8] We add the systematic errors linearly

[9] We use the average value over metallicities, $\langle Y_p \rangle$ (Eq. (8.2) of [187]) and leave the systematic error from [166].

[10] A study of [189], based on the independent dataset, provides the value $Y_p = 0.2477 \pm 0.0029$. Its upper bound becomes very close to that of (3.22) if one employs an additional systematic uncertainty at the level $\Delta Y_{\text{syst}} = 0.010$ (twice the value of systematic uncertainty of [166]).

Code	Y_p for τ_n from PDG [167]	Y_p for τ_n from [168]
(Modified) Kawano code [180]	0.2472	0.2457
PArthENoPE code [186]	0.2480	0.2465
Difference	-0.0008	-0.0008

Table 3.4: Values of Helium abundance Y_p in the Standard Model BBN (SBBN) and their dependence on the neutron lifetime, τ_n.

The other element produced during the BBN is the Deuterium, and recent observations determine its abundance to be

$$D/H = (2.2 - 3.5) \times 10^{-5} \quad \text{(Ref. [155]}, 3\sigma \text{ interval).} \tag{3.26}$$

This value is sensitive both to the baryon-to-photon ratio and to N_{eff}. In our analysis we adjust the value of baryon-to-photon ratio η at the beginning of the computation so that by $T_{\text{Fin}} \sim 10\,\text{keV}$ it is equal to the value given by cosmic microwave background measurements [106].

Finally, we mention another important uncertainty originating from the particle physics. There are two different measurements of neutron lifetime τ_n that are at tension with each other. Particle Data Group [167] provides $\tau_n = 885.7 \pm 0.8\text{sec}$, while measurements performed by Serebrov et al. [168] result in $\tau_n = 878.5 \pm 0.8\,\text{sec}$. We employ both results and explore the differences they lead to in what follows.

3.3 Tests of the numerical approach

The Section below summarizes the comparison of the present analysis with the previous ones that analyzed the influence of the MeV particles on primordial nucleosynthesis. Throughout this Section, we normalize scale factor by imposing condition $aT = 1$ at the initial moment. Conformal momentum is $y = pa$ with the same normalization of the scale factor. In the figures that contain both the solid and the dashed curves, the former correspond to the results obtained with our code, and the latter – to the original results of the other papers.

3.3.1 Standard Model BBN

First we considered the nucleosynthesis in Universe filled with the Standard Model particles only. We compute the actual *non-equilibrium* form of the active neutrino spectra during their decoupling. The results of the present study are compared with those of [165, 164, 192]. In [165, 164] neutrino oscillations were neglected, while in [192] the effect was taken into account. Fig. 3.1 shows the evolution of the quantity aT as a function of temperature. It is identical to the Fig. 1 in Ref. [165].

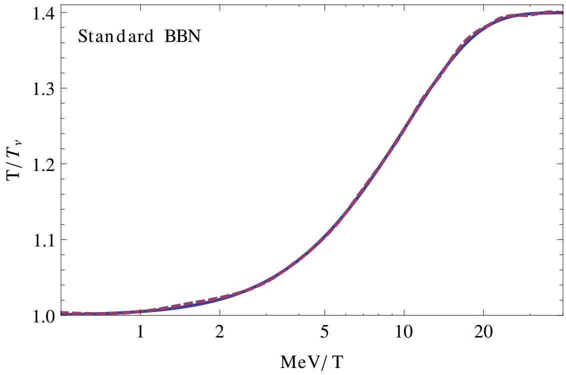

Figure 3.1: T/T_ν as a function of inverse temperature T^{-1}. The **solid** line is produced by the code of the present study, the **dashed** – the result of [165].

Figures 3.2,3.3 show how distorted neutrino spectra f_{ν_α} are, compared to the thermal distribution $f^{eq} = (e^y + 1)^{-1}$. One can see good agreement between the results. We believe that the difference, that is present nevertheless, arises solely due to our one-step time integration method of the stiff kinetic equations, that is not as accurate as the method employed in Refs. [164, 192].

We turned off flavour oscillations and compared asymptotic values of ratio aT at low temperatures together with the effective number of neutrino species, N_{eff}. For the former quantity, Refs. [164, 192] present values 1.3991 and 1.3990, respectively. On the other hand, we derived 1.3996. For the number of neutrino species in absence of neutrino oscillations, the same Refs. [164, 192] provide numbers 3.034 and 3.035, respectively, while we get 3.028.[11]

The resulting Y_p is summarized in Table 3.4 for different values of neutron lifetime τ_n. We also provide a comparison of the modified version of the Kawano code [180] that we adopted for computing nuclear reactions with a newer code, PArthENoPE [186]. By comparing the results of PArthENoPE and the modified KAWANO code, we find the former to be larger by 0.0008 than the latter. We use the shift $\Delta Y_p = -0.0008$ as a correction in our subsequent results.

3.3.2 Test of energy conservation

If all weak reactions involving electrons and positrons are turned off, neutrinos decouple from the rest of plasma. Then the energy conservation law (3.3) holds *separately* for the neutrino component and for the remaining particles. In approx-

---

[11] Ref. [192] takes into account both the effects of neutrino oscillations and QED corrections, the latter changes the result significantly. As a result we could not compare the effect of *neutrino oscillations only*.

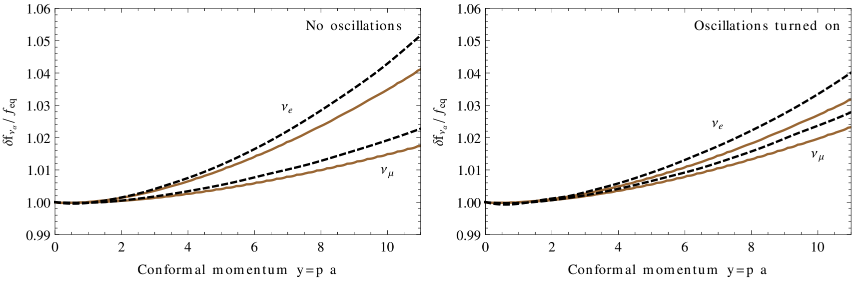

Figure 3.2: Relative distortions of neutrino spectra before the onset of BBN. **Left:** neutrino flavour oscillations are neglected, **right:** the oscillations are taken into account, with the parameter choice $\theta_{13} = 0$, $\sin^2\theta_{23} = 0.5$, $\sin^2\theta_{12} = 0.3$ used in [192]. In both panels, the pair of upper curves shows the distortion of the electron neutrino, the lower – of ν_μ. In each pair, the solid curve is the result of the present study, and the dashed is from Fig. 2 of [192].

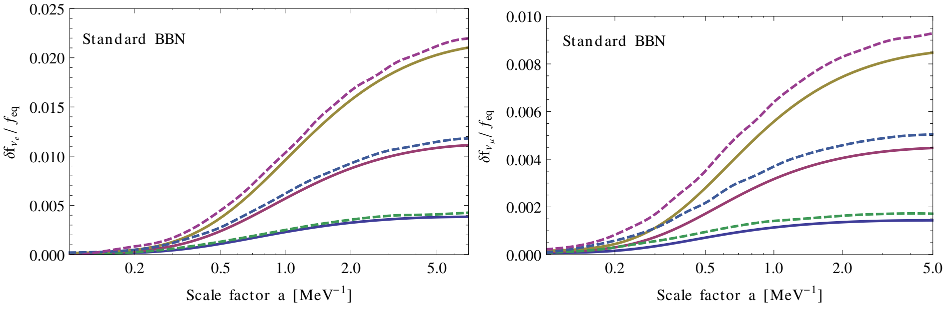

Figure 3.3: **Left:** Relative distortion of ν_e spectra $\delta f_{\nu_e}/f_{\rm eq}$ for conformal momenta $y = 3, 5, 7$ (from bottom to up). **Right:** The same, but for muon neutrino. In each pair of curves the solid one corresponds to the present study and the dashed one is from [165].

imation of zero mass of electron we obtain

$$\frac{d(aT)}{dt} = 0 \tag{3.27}$$

similar to Eq. (3.29). As a corollary, product aT is conserved. On the other hand, our code solves the equation (3.3) involving *all* medium components simultaneously. And it turns out that the relation (3.27) is not a trivial consequence of the numerical computation. Therefore the check of the conservation serves as a test of the code. We considered separately scattering and decay processes involving neutrinos and observed conservation of aT with precision of order 0.2%.

3.3.3 Heavy sterile Dirac neutrino

Next we have tested model with *one* sterile *Dirac* neutrino N with mass $M_s = 33.9$ MeV, mixed with ν_τ [156]. This neutrino was assumed to be in thermal equilibrium with plasma at $T \gtrsim 50$ MeV. To simplify the problem, the authors of [156] used the *Boltzmann equilibrium* statistics for active species in collision integral for a sterile neutrino.

Being in equilibrium the sterile neutrino spectrum becomes more and more non-relativistic with time due to the redshift. Therefore the ratio $\rho_s/M_s n_s$ of the energy density ρ_s to the mass times number density n_s should approach 1 at lower temperatures. We have recomputed the evolution of the system using our code, without the Boltzmann approximation. Fig. 3.4 shows the comparison of the results with those of [156] for sterile neutrino lifetime $\tau_s = 0.3$ sec. Both results coincide till $T \approx 5$ MeV and after that moment ratio $\rho_s/M_s n_s$ of [156] stops decreasing, while the numerical result we obtained shows the expected behaviour — the ratio continues to decrease, approaching 1.

3.3.4 Massive ν_τ

Next we considered a model with the massive tau neutrino [159, 161]. Fig. 3.5 presents relative deviation of the energy densities of massless neutrinos $\delta\rho_\nu/\rho_{\mathrm{eq}}$ produced by our code and plotted in [159]. $\rho_{\mathrm{eq}} = \frac{7\pi^2 T^4}{120}$ is the equilibrium energy density of one neutrino specie, and $\delta\rho_\nu = \rho_\nu - \rho_\nu^{eq}$. In Fig. 3.5 distortion of electron neutrino spectrum $y^2 \delta f_{\nu_e}/f_{eq}$ is depicted. Here one observes good agreement between the results.

3.3.5 Late reheating model

To test the treatment of MeV decaying particles, we considered the low-reheating models with the reheating temperature of several MeV [162, 163]. In [162] heavy non-relativistic particles were considered, that dominated the energy density of the Universe once and then decayed into electrons, positrons or photons (so that decay products are quickly thermalized). The most important output is the effective

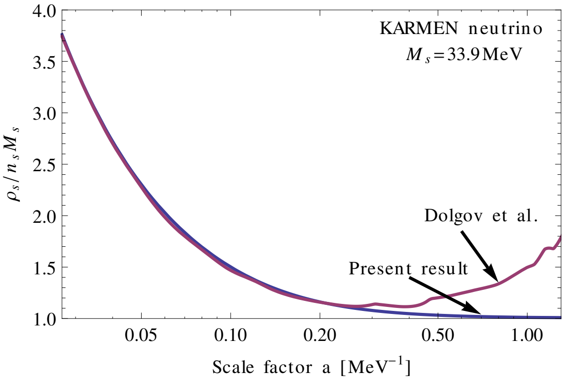

Figure 3.4: Ratio ρ_s/n_sM_s as a function of scale factor for $M_s = 33.9\,\text{MeV}$ sterile neutrino. The upper curve is the result of Ref. [156], the lower curve is the present analysis.

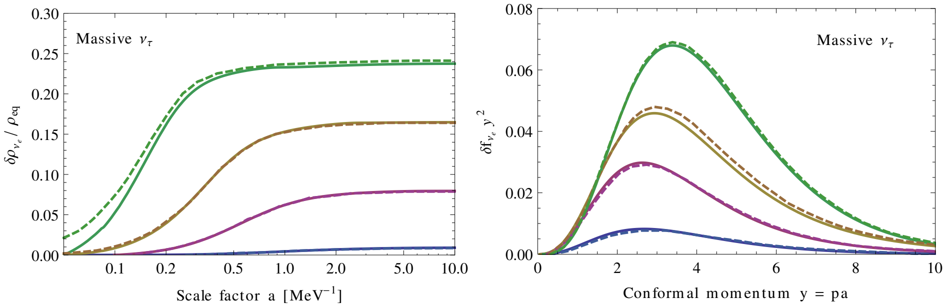

Figure 3.5: **Left:** Relative deviation from its equilibrium value of ν_e energy density $\delta\rho_{\nu_e}/\rho_{\text{eq}}$ in a model where tau neutrino is massive. **Right:** Spectrum distortion $y^2\delta f_{\nu_e}/f_{\text{eq}}$ for the same model. In both panels $M_{\nu_\tau} = 0, 3, 7, 20$ MeV from bottom to top, the solid curves depict the numerical results of the present analysis, and the dashed – the results of [159].

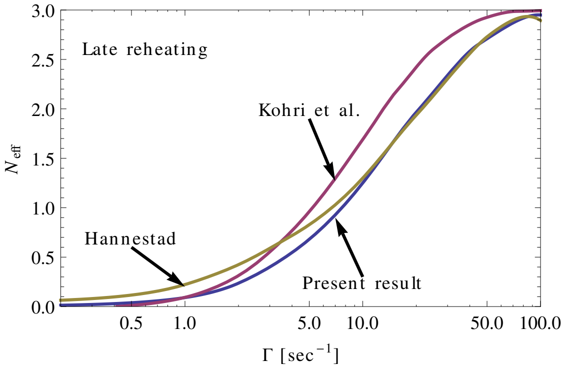

Figure 3.6: Effective number of neutrino species $N_{\rm eff}$ depending on decay width of heavy non-relativistic particles. Comparison of the results of the present study and Refs. [162, 163].

number of active neutrino species $N_{\rm eff}$ (defined in Eq. (3.24)). Dependence of this quantity on decay width of heavy particle is presented in Fig. 3.6. We have noticed some difference between the results of cited papers and those of our code. We believe that this is due to the different approximations made. For example, in both works [162, 163] the scattering processes involving only neutrinos were not taken into account, approximation of Boltzmann statistics was used throughout and electron mass was neglected. We checked that the account of finite electron mass gives a gain of 5% to the $N_{\rm eff}$ for $\tau = 0.1$s, while the account of scatterings involving only neutrinos gives rise of 1%.

3.3.6 Instant thermalization of decay products

Next we considered a model with two heavy Majorana sterile neutrinos, similar to the νMSM . However, we assumed that for any mass of sterile neutrino it can decay *only* via channels listed in Table 3.3. It is not a natural assumption, because usually sterile neutrinos heavier than pion decay dominantly into states containing mesons [108]. Also we approximated sterile neutrino spectrum as a non-relativistic one, while all the other particles are relativistic and in equilibrium all the time. In this case the system may be adequately described by the kinetic equation

$$\frac{d\rho_s}{dt} + 3\frac{\dot{a}}{a}\rho_s = -\Gamma_s\rho_s \tag{3.28}$$

together with the Friedmann equations (3.2–3.3). The latter of these equations can be rewritten as

$$\frac{d(aT)}{dt} = \frac{30a\Gamma_s\rho_s}{43\pi^2T^3} \tag{3.29}$$

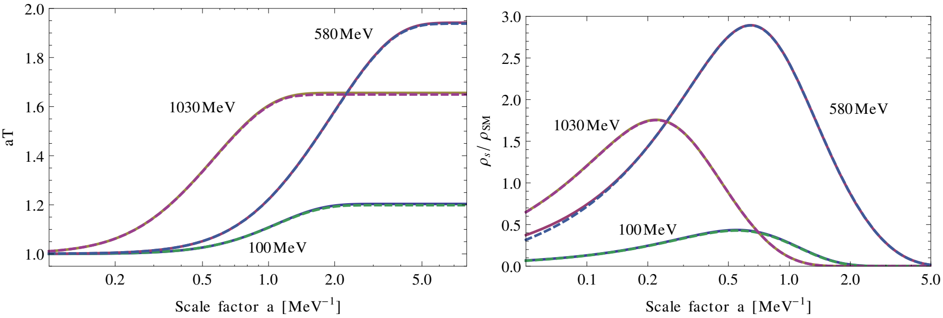

Figure 3.7: **Left:** Evolution of aT for the model of Sec. 3.3.6. **Right:** ρ_s/ρ_{SM}. We consider three parameter sets: sterile neutrino mass $M_s = 580$ MeV with lifetime $\tau = 1$sec; $M_s = 1030$ MeV with $\tau = 0.1$sec; $M_s = 100$MeV, $\tau = 0.5$sec. The solid line depicts the numerical result of the present analysis, dashed – the semianalytical calculation.

Γ_s is the decay width of sterile neutrino, ρ_s is the energy density of sterile neutrinos, and we have used expression for the energy and pressure densities of relativistic species $\rho_{\rm rel} = 3p_{\rm rel} = 43\pi^2 T^4/120$.

In Figs. 3.7 the evolution of quantities aT and $\rho_s/\rho_{\rm rel}$ is compared between the results of our code and the semi-analytic integration of Eqs. (3.28)–(3.29) for three different sets of masses and lifetimes. One can see very good agreement between these results, maximum relative deviation is 1%.

3.4 Results

In this Section we present the main results of this Chapter: the bounds on sterile neutrino lifetime as a function of their masses and mixing patterns, as well as the bounds on the mixing angles. As discussed above, there are several systematic uncertainties in the determination of the ^{4}He abundance and therefore the results will depend on the adopted values of Y_p (together with the neutron lifetime, τ_n). We summarize these systematic effects below.

We start with comparing the upper bounds on sterile neutrino lifetime for different values of Y_p (see Section 3.2.7). The Fig. 3.8a shows that the bounds from the two recent works [166, 187] are quite similar (the difference is of the order of 30%). The bound, based on [189] would give a result, similar to [187] as discussed above.

For the CMB bound in Fig. 3.8a, we present only the results for masses $M_s > 40$ MeV where $N_{\rm eff}$ does not deviate significantly from 3. Fig. 3.9 indicates that for smaller masses the number of effective neutrino species increases significantly. It in turn affects the CMB helium bounds (c.f. Eqs. (3.23) and (3.24)). The accurate

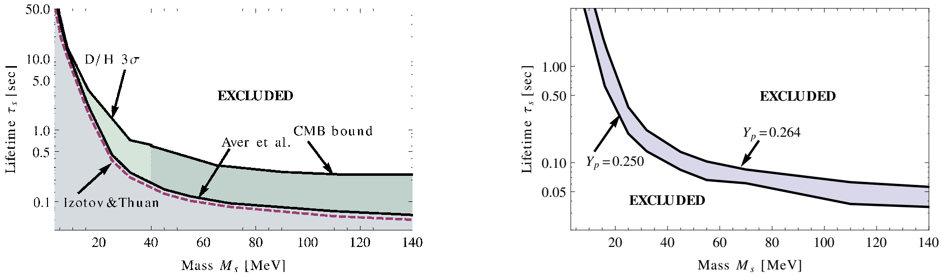

(a) 2σ upper bounds on sterile neutrino lifetime, based on different measurements of Y_p: Ref. [166] ("Izotov & Thuan"); Ref. [187] ("Aver et al."); Refs. [190, 106] ("CMB bound")

(b) Upper *and lower* bounds on sterile neutrino lifetime, based on the measurements of [166]. The upper curve is the same as the dashed curve in the left panel.

Figure 3.8: Bounds (at 2σ level) on sterile neutrino lifetime as a function of their mass for various measurements of Y_p (summarized in Section 3.2.7). All results are for mixing of sterile neutrino with electron flavour only (the dependence on the particular mixing pattern is very weak, see below). For the CMB bound, we present only the result for masses $M_s > 40$ MeV where $N_{\text{eff}} \approx 3$. For smaller masses we plot instead bounds based on 3σ Deuterium upper bound (3.26). For details, see Sec. 3.4 and Fig. 3.9.

account of this effect goes beyond the scope of the present analysis and we choose instead to plot stronger deuterium-based bounds (those of Fig. 3.9) in Fig. 3.8a for $M_s \lesssim 40$ MeV.

The lower bound on Y_p from the recent work of [166] is above the Standard BBN value (3.19) at $\sim 2\sigma$ level (see however [188]). The presence of sterile neutrinos in plasma of course relaxes this tension and therefore at 2σ the adopted values of Y_p (Eq. 3.21) provide both upper and *lower* bounds on sterile neutrino lifetime. This is shown in Fig. 3.8, right panel. At 3σ level the measurements of [166] are consistent with Standard BBN and the lower bound disappears.

Fig. 3.9 shows the changes in Deuterium abundance and in the effective number of neutrino species, caused by sterile neutrinos (with parameters corresponding to the upper bound based on [166]). For these values of parameters the abundance lies within the 3σ boundaries (3.26). And for the highest effective number of neutrinos reached, $N_{\text{eff}} = 6$, D/H is close to the 3σ upper bound. Notice that the same relation between N_{eff} and D/H is observed in the model without new particles but with the effective number of neutrinos different from 3. The effective number of neutrino species does not define the Helium abundance though. Otherwise the same Y_p bound [166] would predict *only one particular* value of N_{eff}, which is not case, as the inspection of Fig. 3.9 shows.

The influence of another systematic uncertainty (the lifetime of neutron, τ_n) is

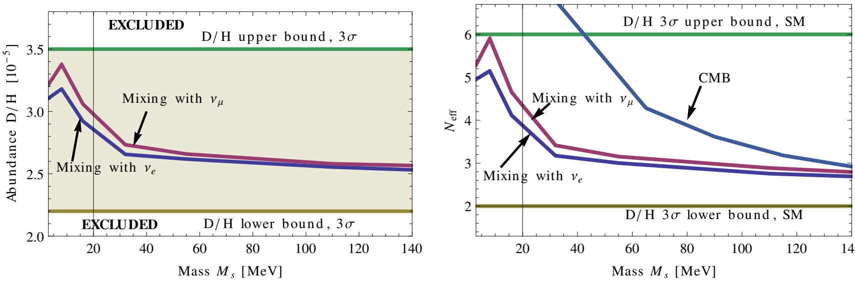

Figure 3.9: **Left:** Deuterium abundance, with the shaded region corresponding to the *allowed* 3σ range, based on [155]. **Right:** Effective number of neutrino species (the ratio of the effective neutrino temperature to the photon temperature at $T \sim$ few keV) as a result of decay of sterile neutrino. The horizontal "SM" lines indicate $N_{\rm eff}$ that corresponds to the boundary of the 3σ range [155], in the SM with the number of relativistic species deviating from $N_{\rm eff} \approx 3$. In both panels, parameters of sterile neutrinos correspond to the upper bound on Y_p from [166] (see Eq. (3.21)), except of the "CMB" line that corresponds to the upper bound from [190, 106] (see Eq. (3.23)).

negligible. Indeed, the relative difference between sterile neutrino lifetimes were found to be of the order of 5% for two choices of τ_n – from [168] and from [167] (taking the same Y_p bound from [187]).

Next we investigate the dependence of the resulting bounds on the mixing patterns of sterile neutrinos. Naively, one would expect that sterile neutrinos mixing "only with ν_e" and "only with ν_μ" should have different effect of Y_p. However, it is the energy "injection" rate (i.e. the overall decay rate of sterile neutrinos) that is *more important* for the dynamics of plasma before the onset of nucleosynthesis. This quantity depends on the lifetime τ_s and the mass M_s of the neutrino. Mixing patterns affect mostly the concentration of particular decay products, but not the injection rate. In addition, the neutrino oscillations (fast at the BBN epoch) make the difference between flavours less pronounced (see Sec. 3.2.4). As a result, mixing patterns give essentially the same results with the difference at the level of tens of per cent (see Figs. 3.10, 3.11).

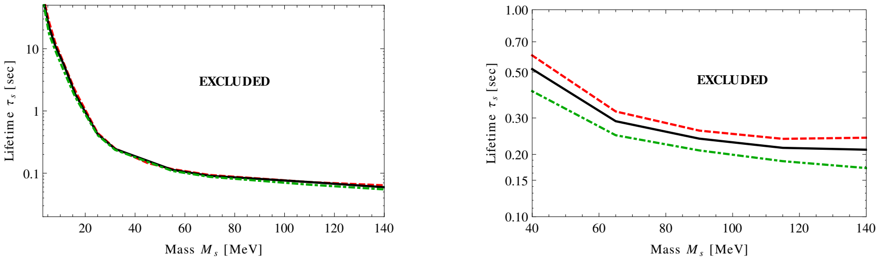

(a) Bounds based on astrophysical measurements of Y_p of [187]

(b) Bounds from CMB (notice different y-axis range!).

Figure 3.10: Upper bound for sterile neutrino lifetime for different mixing patterns: mixing with ν_e-only (red dashed line), ν_μ-only (green dashed-dotted line) and equal mixing with ν_e and ν_μ flavours (black solid line). All bounds are derived for the lifetime of neutron τ_n adopted from [167]. The effect of different mixing patterns is at the level $\sim 10-50\%$ and can only be seen in the right panel because of the different y axis. In the right panel, only the masses $M_s > 40$ MeV are presented. For details, see Sec. 3.4 and Fig. 3.9.

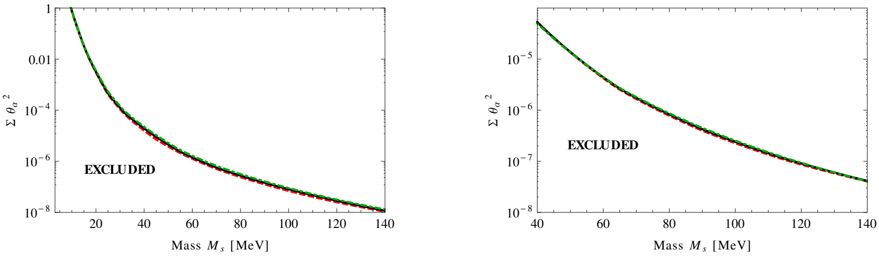

(a) Bounds based on astrophysical measurements of Y_p of [187]

(b) Bounds from CMB

Figure 3.11: *Lower* bound on mixing angles of sterile neutrinos for different mixing patterns: mixing with ν_e-only (red dashed line), ν_μ-only (green dashed-dotted line) and equal mixing with ν_e and ν_μ flavours (black solid line). Both types of bounds are derived by assuming lifetime of the neutron τ_n from [167]. In the right panel, only the masses $M_s > 40$ MeV are presented. For details, see Sec. 3.4 and Fig. 3.9.

3.5 Discussion

In this Chapter we have considered the influence of decaying particles with the masses few MeV –140 MeV on the primordial abundance of light elements (D and ^{4}He). Such particles appear in many cosmological scenarios [109, 147, 193,

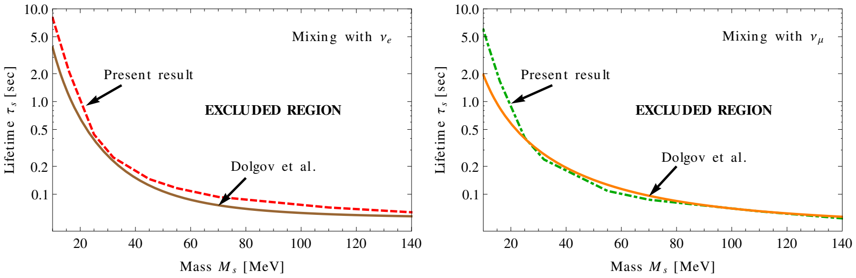

Figure 3.12: Comparison with the previous results of [156, 157]

159, 160, 161, 162, 163, 194, 195, 196]. Particularly, we concentrated on the properties of sterile neutrinos and derived constraints on their lifetime imposed by the present measurements of primordial Helium and Deuterium abundances.

We analyzed the case of two Majorana sterile neutrinos with 4 degrees of freedom in total (if sterile neutrinos were kept in thermal equilibrium it would be equivalent to two addtional falvours of active neutrinos). Since the plasma evolution is mostly affected by the overall decay rate of sterile neutrinos, the lifetime bounds that we obtained are essentially independent of the particular mixing patterns, as Figs. 3.10,3.11 demonstrate.

In the paper [157] a similar model was considered with one *Dirac* sterile neutrino. Dirac sterile neutrino has the same 4 degrees of freedom and influences primordial plasma in the same way (if it has the same spectrum, lifetime and mixing pattern). However, in [157] effect of active-neutrino oscillations was not taken into account, and some simplifying approximations like Boltzmann statistics were employed. To provide the corresponding analysis we wrote a code that solves more accurate set of Boltzmann equations describing kinetics of neutrino, than what were used in [157]. We compare the results of our analysis with the previous bounds [156, 157] in Fig. 3.12. We see that our results are broadly consistent with the previous works. The differences for a given mixing pattern of sterile neutrinos can be as large as a factor of 2.5 for some masses.

The presence of sterile neutrinos in the plasma affects the effective number of neutrino degrees of freedom, N_{eff}. Right panel of Fig. 3.9 shows that N_{eff} between 2.7 and 6 are possible for different mixing angles and masses, which could explain a larger than 3 values of N_{eff}, reported recently in several CMB observations (see e.g. [190, 197, 191], but also [198]).

Decaying sterile neutrinos with the masses $100 - 500$ MeV and lifetimes from seconds to minutes and their influence on N_{eff} and entropy production have been recently considered in [193] (see also [199]) where it was demonstrated that they can lead to $N_{\text{eff}} \neq 3$ and can therefore be probed with the CMB measurements. The results of the present analysis demonstrate that in the region $100 - 140$ MeV where we overlap with the parameter space, studied in [193], the primordial nu-

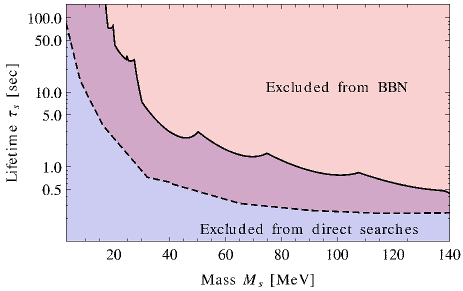

Figure 3.13: Experimental 3σ *lower* bounds on the lifetime of sterile neutrinos [200] (solid line), combined with the *upper* bounds from the present analysis (dashed line), corresponding to the *weakest* bound in Fig. 3.8a. The accelerator bounds are for two Majorana sterile neutrinos solely responsible for neutrino oscillations. **Left:** normal hierarchy, **right:** inverted hierarchy. Combination of BBN bounds with direct experimental searches demonstrates that sterile neutrinos with the masses in 1-140 MeV range, solely responsible for neutrino oscillations are ruled out. See Secs. 3.4,3.5 for details.

cleosynthesis restricts the lifetime of sterile neutrinos to be well below 1 sec (see Fig. 3.8, left panel).

Finally, it is interesting to compare the upper bound on sterile neutrino lifetime, derived in this Chapter with the *lower bounds* that come from direct experimental searches for two Majorana sterile neutrinos, which are solely responsible for the observed pattern of neutrino oscillations via the see-saw mechanism (see Chap. 2). The appropriate comparison is presented in Fig. 3.13.

If two Majorana sterile neutrinos describe neutrino oscillations, no allowed values of sterile neutrino lifetimes for 1 MeV $\lesssim M_s < 140$ MeV exist, which satisfy the BBN bounds, for either type of neutrino mass hierarchy.

(i.e. the upper bound is *smaller* than the lower bound, see the purple double-shaded region in Fig. 3.13).

Notice, that if the astrophysical bounds on Helium [166, 187] were used for $M_s \gtrsim 40$ MeV in Fig. 3.13, instead of the CMB bound, the resulting lifetime bounds would become stronger (by as much as a factor of 4) in this mass range. *We stress that for this conclusion it is essential* that MeV sterile neutrinos are responsible for neutrino oscillations. For example, a model in which sterile neutrinos couple to ν_τ *only* (and therefore do not contribute to the mixing between active neutrino flavours), *is allowed* even if one confronts the strongest BBN bounds (based on the astrophysical Helium measurements) with the direct accelerator bounds, see Fig. 3.14 for details.

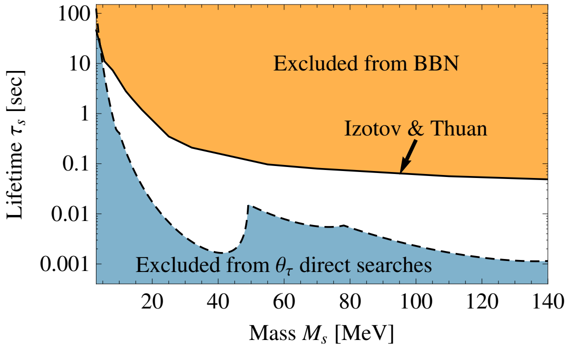

Figure 3.14: Comparison of direct accelerator constraints and BBN bounds, based on the Helium-4 measurements of [166] in the model where sterile neutrinos mix with ν_τ *only*. Unlike the case, presented in Fig. 3.13 there is an allowed region of parameter space for most of the masses below 140 MeV.

Chapter 4

Sterile neutrinos between baryogenesis and nucleosynthesis

4.1 Leptogenesis and chiral magnetic effect

Let us consider first the production of lepton asymmetry by sterile neutrinos at $T \gtrsim 100$ GeV, when sphalerons still operate, so that the lepton asymmetry is transformed partially into the baryon asymmetry. Then, we deal with "restored" (or "unbroken") electroweak phase, where the ground state of the plasma is invariant under the electroweak $SU_L(2) \times U_Y(1)$ group, and massive gauge bosons $W^{\pm}$ and Z become massless, like photon.[1]

From the form of the Yukawa interaction (1.3), we see that sterile neutrinos interact directly only with left particles. Therefore, during the leptogenesis, lepton asymmetry is produced first in the sector of left particles. Afterwards, in reactions with the gauge bosons, the number of left- and right-chiral particles is conserved, since the interaction of fermions with gauge bosons

$$\Delta\mathcal{L}_{\text{gauge}} = \bar{L}\gamma^{\mu}(g_W V_{\mu} + g_L B_{\mu})L + g_R \bar{R}\gamma^{\mu} B_{\mu} R \tag{4.1}$$

does not mix different chiralities. Here L and R are the left-handed fermion doublets and right handed singlets, respectively, g_W is the weak coupling constant, g_{L} and g_{R} are the hypercharge couplings of left- and right-chiral particles, which are different, $g_{\text{L}} \neq g_{\text{R}}$. V_{μ} is the $SU_L(2)$ gauge field, B_{μ} is the $U_Y(1)$ field. (Since $SU_L(2)$ transformations are characterized by three parameters, V_{μ} actually includes three independent fields.) At lower temperatures, when the electroweak

---

[1] Actually, all the SM particles become massless in this phase. Only sterile neutrinos remain massive.

symmetry is broken (in the "broken" phase), the interaction $\Delta\mathcal{L}_{\text{gauge}}$ becomes

$$\Delta\mathcal{L}_{\text{gauge}} = \frac{g_W}{\sqrt{2}} W_\mu \bar{e}_{\text{L}}\gamma^\mu \nu_{\text{L}} + Z_\mu (g_\nu \bar{\nu}_{\text{L}}\gamma^\mu \nu_{\text{L}} + g_{eL}\bar{e}_{\text{L}}\gamma^\mu e_{\text{L}} + g_{eR}\bar{e}_{\text{R}}\gamma^\mu e_{\text{R}}) - eA_\mu(\bar{e}_{\text{L}}\gamma^\mu e_{\text{L}} + \bar{e}_{\text{R}}\gamma^\mu e_{\text{R}}), \tag{4.2}$$

where W_μ, Z_μ and A_μ are the fields of W-, Z-bosons and photon, respectively. (These fields are linear combinations of the fields V_μ and B_μ above.) This interaction does not mix chiralities, as well as in the unbroken phase. However, since sterile neutrinos interact with both W and Z, and Z-bosons couple to both types of chiralities, the leptogenesis in the broken phase produces *both* left and right particles. But it is important that due to parity violation, the numbers of these particles are different even in the broken phase (chiral asymmetry is generated).

According to what was said above, one may expect that once we produce chiral asymmetry, it remains conserved. However, as we have pointed out in Sec. 1.3.5, there exist scattering processes, which change chirality (the chirality-flipping processes). Indeed, in the SM, there exists Yukawa interaction

$$\Delta\mathcal{L}_{\text{Yukawa}} = y_f \bar{L} H R \tag{4.3}$$

which becomes

$$\Delta\mathcal{L}_{\text{Yukawa}} = m\bar{e}_{\text{L}} e_{\text{R}} + y_f \bar{e}_{\text{L}} e_{\text{R}} h, \tag{4.4}$$

after the spontaneous breaking of electroweak symmetry, and the first term on the right-hand side is the Dirac mass term. (This generation of Dirac mass is similar to case of neutrinos, see Sec. 1.2.1). Here y_f is the Yukawa constant, which is proportional to the fermion mass m, h is the field of the Higgs boson. Presence of the Yukawa interaction in the unbroken phase indicates that left fermion can transform into right fermion by emitting (or absorbing) the Higgs particle. However, for the lightest massive electrically charged fermion (electron), the Yukawa constant is relatively small, so the chirality-flipping processes with right-chiral fermions have rates $\Gamma_f \sim y_f^2 T$, which are much smaller than the rate of (chirality-conserving) interactions of fermions with gauge bosons, $\Gamma_{\text{SM}} \sim g_W^2 T$.

In the broken phase, there are two mechanisms of chirality flip. First mechanism is similar to the restored phase, where the Higgs particle can be emitted/absorbed by a left-chiral electron, and the electron will become right-chiral. However, this mechanism requires high enough density of the Higgs bosons, which is exponentially suppressed for small temperatures, since the Higgs boson becomes massive and quite heavy in the broken phase (recall that the Higgs boson mass in vacuum is $m_h \approx 125\,\text{GeV}$). The second mechanism is related to appearence of fermion mass: massive electrons do not have a definite chirality. The rate of the chirality-flipping processes in this case is $\Gamma_f \sim e^2 m^2/T$.

Using the estimates for the chirality-flipping rates given above, one concludes $\Gamma_f \gg H(T)$ ($H(T)$ is the Hubble rate) at $T < 80\,\text{TeV}$ [95] in both broken and unbroken phases, so during the leptogenesis, chirality-flipping processes are kept in thermal equilibrium. However, if sterile neutrinos inject significant chiral asymmetry very fast, on the timescale smaller than Γ_f^{-1}, then before the chirality-flipping processes start to operate, the Chiral Magnetic Effect becomes important (see Sec. 1.3.8).[2] As we have noticed in Sec. 1.3.5, magnetic fields start to grow exponentially with time (system becomes unstable against creation of magnetic fields), so apart from the equations describing non-equilibrium dynamics of fermions, one has to consider Maxwell equations. According to Eq. (1.48), although only the magnetic fields with large coherence scale start to grow, this scale is finite, and as a result, plasma becomes inhomogeneous. It means that the *chiral asymmetry*, which is coupled to magnetic fields, *becomes inhomogeneous* as well. Another feature is that the scale of inhomogeneities is much smaller than the cosmological horizon $1/H(T)$, so the magnetic fields are *sub-horizon*.

Electric currents flowing in presence of magnetic fields lead to the Lorentz force, which acts on plasma. As a result, macroscopic motions are excited, and one expects that the system is described by some kind of magnetohydrodynamics. And we know, that such hydrodynamical effect as turbulence, appears, and it should be consistently taken into account in the analysis of the νMSM model. However, before one carries out such a study, all of its individual ingridients must be understood well. In particular, one may notice, that in the derivation of the Chiral Magnetic Current in Sec. 1.3.5, fermion mass m was neglected. How does the picture change if we take into account m? Answering this question turns out to be non-trivial and it will be the main subject of this Chapter.

4.2 Chiral Magnetic Effect and non-zero fermion mass

The Chiral Magnetic Current

$$\boldsymbol{j} = -\frac{e^2}{4\pi^2}(\mu_{\rm L} - \mu_{\rm R})\boldsymbol{B} \tag{4.5}$$

was discovered some 35 years ago in [201], although the importance of this work has not been immediately recognized. The paper [201] had zero citations for the first 18 years, while in the last 5 years it accumulated 100+ citations. The result (4.5) has been independently rediscovered by a number of authors [202, 203, 204, 93, 94, 205, 206, 207], for a recent review and historical introduction, see [208].

Our everyday intuition considers an electric current as a non-equilibrium process, that requires energy to be pumped into a system and whose flow generates

---

[2] However, as we have noticed in Sec. 1.3.3, above the temperature of the sphaleron freeze-out, lepton asymmetry in the νMSM is of order of baryon asymmetry, therefore the chiral asymmetry is small and is not expected to give rise to significant Chiral Magnetic Effect. When the Universe cools down below $T \simeq 100$ GeV, the sterile neutrinos generate much larger lepton asymmetry, until they come into equilibrium at $T = T_+$ (see Sec. 1.3.3).

entropy. However, as we saw in the derivation in Sec. 1.3.6, the chiral magnetic current flows in the system in the state of thermal equilibrium and is *dissipationless* – it does not generate entropy [206, 209] (unlike for example the Ohmic current, $\boldsymbol{j} = \sigma \boldsymbol{E}$), and the system with this current flowing has time-reversal symmetry [209]. The presence of the current (4.5) in the Maxwell equations has important consequences in the heavy ion collisions [210, 211], in the early Universe [212, 213], in the astrophysical systems [214, 215, 216, 217] and magnetohydrodynamics of relativistic plasmas [218, 219, 220], Weyl semi-metals [221, 222], see [208, 223] for review.

The quantum-mechanical derivation of the chiral magnetic current, which was presented in Sec. 1.3.6 (following the work [90]), is applicable only to the case of *static and homogeneous* magnetic field (although the strength of this field formally can be arbitrarily large). In order to find the current for the magnetic field with arbitrary time and spatial dependence, one may use the field-theoretical methods instead, and look for the parity-odd part of the effective action of the gauge field (1.35). The field-theoretical approach was applied in the same paper [90], and the result for the electric current was the same as in the quantum-mechanical method, in the limit of static and homogeneous magnetic field.

As it was noted in [202], the parity-odd polarization operator (1.36), which enters the effective action of the gauge field (Fig. 4.1a) reduces to the triangular graph of Fig. 4.1b with $\Delta\mu = \mu_{\rm L} - \mu_{\rm R}$.

The original derivation of the Chiral Magnetic Current [90] was obtained for *massless* fermions. By turning on non-zero fermion mass m, we see that sending $m \to 0$ while keeping the wave-number $|\boldsymbol{q}|$ finite means that we are interested in the *short-ranged* gauge fields, i.e. that we are considering a gradient expansion of the parity-odd polarization tensor $\Pi_2(\boldsymbol{q})$ in powers of $|\boldsymbol{q}|/m \gg 1$. While this expansion is possible, it is difficult to imagine physically relevant situations when on the one hand $m \ll |\boldsymbol{q}|$, and on the other hand, we are still in the infrared region $|\boldsymbol{q}| \ll e^2(\mu_{\rm L} - \mu_{\rm R})$ (recall (1.49)), where the Chiral Magnetic Effect dominates the dynamics of the magnetic field.

In this Chapter we are exploring the question: does the expression (4.5) hold for the electrodynamics of long-range magnetic fields (i.e. for $|\boldsymbol{q}| \ll m$) or, alternatively, can the long-wavelength Chern-Simons term appear in the effective action for the electromagnetic fields in the electron-positron plasmas.

In order to produce the chiral magnetic effect, one has to create chiral asymmetry in the plasma. There are two distinct ways to do this in the system of charged *massive* particles:

(I) One could consider a plasma with different populations of left- and right-helical states.

(II) One can introduce a parity-odd part to the dispersion relation of the charged particles.

As we have noted above, for the case *(I)* the chirality flipping processes due to

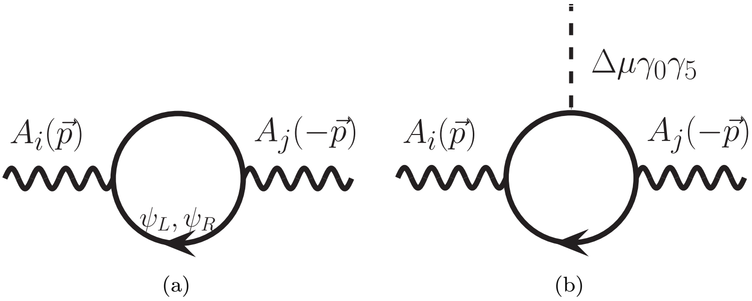

Figure 4.1: Parity-odd part of the polarization operator of the gauge fields in plasma (a) is related to the triangular anomaly with 1 axial and two vector (or 1 vector and two axial) vertices (b).

the finite fermion mass drive the chiral imbalance ($\mu_{\mathrm{L}} - \mu_{\mathrm{R}}$) to 0. Thus the chiral asymmetry can exist only for the *finite time* and the whole system should be treated as a *non-equilibrium* one (see e.g. [213, 218]) and one cannot use methods of equilibrium quantum field theory, like the imaginary-time (Matsubara) technique. Indeed, these methods operate with chemical potentials, that are defined for *conserved* quantum numbers. We discuss the case *(I)* in the Section 4.3.

In the case *(II)* chiral imbalance is due to dispersion relations of the fermions modified by an axial self-energy, $\Sigma_A = b_0\gamma^0\gamma^5$. Indeed, in absence of fermion mass, the effect of self-energy is very similar to the effect of chemical potentials $\mu_{\mathrm{L}} = b_0$, $\mu_{\mathrm{R}} = -b_0$. The key difference is that the self-energy actually modifies the energy spectrum of individual fermions, while chemical potentials define the initial state of the system. Therefore, equilibrium description can be used in the case *(II)*. When masses of the fermions are taken into account, the similarity between the two cases gets destroyed, even if the temperature of the system is high. The modification of dispersion relation can originate from the medium effects (e.g. as a result of weak interactions in the hot dense plasma with non-zero lepton or baryon number (see [178, 98]) or have "fundamental" origin, like in CPT-violating theories considered in [224].

The model with axial self-energy at finite temperatures is studied in Sec. 4.4, and we argue that the current similar to (4.5) *may not* appear actually, although a naive calculation indicates the opposite.

In the νMSM , both scenarios *(I)* and*(II)* are expected to be realized, since leptogenesis populates plasma with different numbers of left and right leptons, and presence of lepton asymmetry itself produces parity-violating self-energy of fermions ($b_0 \neq 0$) [51, 98] (see below and Chap. 5).

4.3 Asymmetric population of left/right helical states

We start by considering the non-equilibrium case *(I)* – massive electrically charged fermions – and show explicitly that Eq. (4.5) remains true in the leading $(m/T)^2$ order, if there exists asymmetry between the number of relativistic particles with left and right helicities. The resulting polarization operator is given by the expression (4.10) below. We will discuss the properties and origin of this result that will allow us to analyse a more intricate case *(II)* below (Section 4.4).

In case of free massless fermions, the state of definite chirality would also have definite *helicity* – projection of the spin of the particle on the direction of its momentum, $\boldsymbol{p}$. However, unlike the chirality operator, γ^5, the helicity operator,

$$h \equiv -\frac{\boldsymbol{p}\cdot\boldsymbol{\gamma}}{|\boldsymbol{p}|}\gamma^0\gamma^5 \ , \tag{4.6}$$

also commutes with the *massive* Dirac Hamiltonian:

$$\mathcal{H}_{\text{Dirac}} = \gamma^0(\boldsymbol{\gamma}\cdot\boldsymbol{p} + m) \tag{4.7}$$

Therefore, in presence of mass, states with definite energy are not characterized by definite chirality, but can be characterized by definite helicity instead.

Although during the leptogenesis, fermions are produced with definite chirality, afterwards, due to oscillations between different chiralities, and due to the scattering processes like $e^-\gamma \to e^-\gamma$ and $e^-e^+ \to \gamma\gamma$, these states will transform into the eigenstates of the massive Dirac Hamiltonian: the states with definite helicity.

Below, we consider two different approaches to find the chiral magnetic current, which give however the same answer. The first approach is described in Sec. 4.3.1, and there we study (quasi-)equilibrium distribution of fermions, whose energy levels are modified in presence of constant homogeneous magnetic field. The result is non-perturbative in magnetic field (i.e. it can be applicable to strong magnetic fields). In the second approach, which is described in Sec. 4.4.2, we consider (time-dependent and inhomogeneous) electromagnetic field as a perturbation, and find the linear response of the system to this perturbation.

4.3.1 Plasma in homogeneous magnetic field

First, we extend the approach of Section 1.3.6, which was used for calculation of the Chiral Magnetic Current for the massless fermions in the *static and homogeneous magnetic field*, by considering non-zero mass m. Instead of repeating the derivation, we point out the essential differences between cases of massive and massless fermions. Presence of mass leads to mixing of left and right chiralities even in absence of magnetic field, hence there will be no separate left and right Landau levels. In particular, the zeroth Landau levels ($n = 0$) of left and right chirality will combine into one, and the momentum p^z along the magnetic field will not be bounded by (1.32) anymore, instead it will run in the full range $-\infty < p^z < \infty$. At the same time, all the particles at this level will remain polarized opposite to the direction of the magnetic field, therefore the sign of p^z will describe the fermion *helicity*: if $p^z > 0$, then the spin is opposite to momentum, the fermion is left-helical; if $p^z < 0$, the fermion is right-helical. The dispersion relation (1.29) is replaced by

$$\varepsilon_n(p^z) = \sqrt{(p^z)^2 + 2|eB|n + m^2}, \tag{4.8}$$

In the massive case, the equilibrium Fermi distributions (1.27) correspond to left- and right-*helical* particles, respectively (in order to distinguish the massive and massless cases, in the massive case we replace μ_{L} by $\mu_\downarrow$, and μ_{R} by $\mu_\uparrow$). $\mu_\downarrow \neq \mu_\uparrow$ implies that in this state, left and right helicities are populated asymmetrically. As we have discussed above, this state is *quasi*-equilibrium.

Using the statistical formula (1.33), we find once again that the contributions to the electric current from the $n \neq 0$ Landau levels are cancelled, and the remaining contribution

$$\boldsymbol{j} = -\frac{e^2}{4\pi^2}(\mu_\downarrow - \mu_\uparrow)\boldsymbol{B}\left(1 + \mathcal{O}\left(\frac{m^2}{T^2}\right)\right) \tag{4.9}$$

comes from the zeroth levels. This expression coincides with Eq. (4.5) for massless particles, after the identification $\mu_{\mathrm{L}} \leftrightarrow \mu_\downarrow$, $\mu_{\mathrm{R}} \leftrightarrow \mu_\uparrow$, up to the corrections suppressed by fermion mass. Therefore, the Chern-Simons coefficient is

$$\Pi_{\mathrm{CS}} = \frac{e^2}{4\pi^2}(\mu_\downarrow - \mu_\uparrow)\left(1 + \mathcal{O}\left(\frac{m^2}{T^2}\right)\right). \tag{4.10}$$

We note once again, that the described quantum-mechanical method with Landau levels is applicable only to the static and homogeneous magnetic field. Below, we consider an alternative approach, which can be extended to time-dependent and inhomogeneous fields.

4.3.2 Plasma in inhomogeneous magnetic field

Let us turn off the magnetic field for a moment. The density matrix, which describes the state with asymmetry of left and right helicities can be written as a product of electrons' and positrons' density matrices

$$\varrho = \varrho_{\mathrm{el}} \otimes \varrho_{\mathrm{pos}} \tag{4.11}$$

where

$$\begin{aligned}\varrho_{\mathrm{el}} = \prod_{\boldsymbol{p}} &\left[\Big(1 - n_{\mathrm{F}}(E_{\boldsymbol{p}} - \mu_\downarrow)\Big)\left|0_\downarrow\right\rangle\left\langle 0_\downarrow\right| + n_{\mathrm{F}}(E_{\boldsymbol{p}} - \mu_\downarrow)\left|e^-_\downarrow\right\rangle\left\langle e^-_\downarrow\right|\right] \\ \otimes &\left[\Big(1 - n_{\mathrm{F}}(E_{\boldsymbol{p}} - \mu_\uparrow)\Big)\left|0_\uparrow\right\rangle\left\langle 0_\uparrow\right| + n_{\mathrm{F}}(E_{\boldsymbol{p}} - \mu_\uparrow)\left|e^-_\uparrow\right\rangle\left\langle e^-_\uparrow\right|\right].\end{aligned} \tag{4.12}$$

Here $E_{\boldsymbol{p}} = \sqrt{\boldsymbol{p}^2 + m^2}$ is the energy of the states $|e^-\rangle$ with *definite helicity* (4.6):[3]

$$h\left|e^-_\downarrow\right\rangle = -\left|e^-_\downarrow\right\rangle \quad ; \quad h\left|e^-_\uparrow\right\rangle = +\left|e^-_\uparrow\right\rangle \tag{4.13}$$

The positron density matrix ϱ_{pos} has a similar form, but $\mu_\downarrow, \mu_\uparrow$ are replaced by $-\mu_\uparrow, -\mu_\downarrow$ respectively. Here the function $n_{\text{F}}(x)$ is the Fermi-Dirac distribution, so that

$$n_{\text{F}}(E_{\boldsymbol{p}} - \mu_\downarrow) = \frac{1}{\exp\left(\frac{\sqrt{\boldsymbol{p}^2+m^2}-\mu_\downarrow}{T}\right)+1} \tag{4.14}$$

Clearly the distribution (4.14) looks like a chiral distribution function under the identification $\mu_{\text{L}} \leftrightarrow \mu_\downarrow$ and $\mu_{\text{R}} \leftrightarrow \mu_\uparrow$. Since the helicity operator commutes with the Hamiltonian (4.7), the state (4.11) is an equilibrium state in the absence of particle interactions. Indeed, neither spin, nor momentum of a fermion can change if no interactions are present in the Hamiltonian.

Let us now perturb the system by turning on electromagnetic field:

$$\mathcal{H} = \mathcal{H}_{\text{Dirac}} + \Delta\mathcal{H}_A\,, \tag{4.15}$$

where

$$\Delta\mathcal{H}_A = e\int d^3\boldsymbol{x}\, A_\mu(t,\boldsymbol{x})\hat{\jmath}^\mu(\boldsymbol{x}), \quad \hat{\jmath}^\mu(\boldsymbol{x}) =: \bar{\psi}(\boldsymbol{x})\gamma^\mu\psi(\boldsymbol{x}) :\,. \tag{4.16}$$

We use here the normal-ordered current, which is denoted by **:** ... **:**.

It can be demonstrated, that in the first order in perturbation $\Delta\mathcal{H}_A$ the external gauge potential $A_j(\boldsymbol{q})$ causes the current

$$\langle \boldsymbol{j}^i\rangle_{\mu_\downarrow,\mu_\uparrow} = i\int\frac{d^3\boldsymbol{r}}{(2\pi)^3}\Big[n_{\text{F}}(e_\downarrow)\mathcal{M}^{ij}(e_\downarrow)+n_{\text{F}}(e_\uparrow)\mathcal{M}^{ij}(e_\uparrow)+(e\leftrightarrow e^+)\Big]A_j(\boldsymbol{q}) \tag{4.17}$$

where $\mathcal{M}_{\mu\nu}(e^-_\downarrow)$ is the matrix element of the Compton scattering of negative-helicity electrons, $e^-_\downarrow\gamma \to e^-_\downarrow\gamma$ (see Fig. 4.2, right panel)[4]

$$\mathcal{M}^{ij}(e_\downarrow) = +ie^2\bar{u}_\downarrow(r)[\gamma^i S(r+q)\gamma^j + \gamma^j S(r-q)\gamma^i]u_\downarrow(r), \tag{4.18}$$

Here $u_\downarrow(r)$ are the Dirac spinors, $(\not{r}-m)u_\downarrow(r) = 0$, which characterize the electron state with negative helicity, $h(\boldsymbol{r})u_\downarrow(\boldsymbol{r}) = -u_\downarrow(\boldsymbol{r})$; $S(p) = i(\not{p}-m)^{-1}$ is the Dirac propagator. *It should be stressed* that the expression (4.17) is exact in

---

[3] If we think about the momentum of electron pointing *up* then the symbols ↑ and ↓ denote the states with positive (negative) projection of spins on momentum.

[4] The scattering is in the forward regime here, i.e. the helicities and momenta of incoming and outgoing particles are equal.

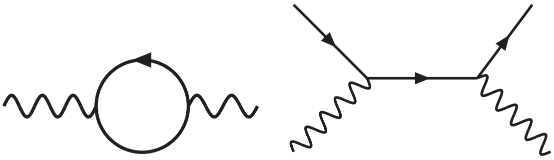

Figure 4.2: **Left**: The 1-loop contribution to the polarization tensor of electromagnetic field. **Right**: The Compton scattering amplitude at tree level, which leads to the 1-loop contribution after statistical averaging (the other amplitude should be taken into account as well, which results from the exchange of photon lines). In both digrams, wavy lines correspond to photons, solid lines correspond to charged fermions.

the first order in e^2. In Eq. (4.17) the helicity-flipping parts of the Compton scattering amplitude does not appear. Computing the expression (4.17) leads to the following current, proportional to the difference of $\mu_\downarrow - \mu_\uparrow$:

$$\langle \boldsymbol{j} \rangle_{\mu_\downarrow,\mu_\uparrow} = -\frac{e^2}{4\pi}(\mu_\downarrow - \mu_\uparrow)\boldsymbol{B}\left(1 + \mathcal{O}\left(\frac{m^2}{T^2}\right) + \mathcal{O}\left(\frac{\boldsymbol{q}^2}{T^2}\right)\right). \tag{4.19}$$

This answer is identical to Eq. (4.9).

4.4 Axial self-energy of the fermions

The previous Section discusses the situation when the parity-even system (electrons coupled to electromagnetic field) is placed into the parity-odd thermal state. Here we consider the case *(II)*. Namely, we modify the dispersion relation for left- and right-chiral particles so that the system has fundamental violation of parity. The system is put in a state of thermal equilibrium at finite temperature T (and no chemical potentials). Namely, the Lagrangian of the system is

$$\mathcal{L}_A = \bar{\psi}(i\partial\!\!\!/ - m - \Sigma_A)\psi, \tag{4.20}$$

$$\Sigma_A = b_0\gamma^0\gamma^5. \tag{4.21}$$

Such a system can appear if one considers fermions propagating in the hot plasma with non-zero lepton (baryon) number. In that case the self-energy part of the fermions acquires a parity odd self-energy Σ_A due to the one-loop weak corrections (see e.g. [178, 98]). A system with Lagrangian (4.20) at zero temperatures/densities has been also considered in [224, 225] (see also [226]), where the parameter b_0 was treated as a fundamental CPT-violating term, and the phenomenological consequences of its presence in the Lagrangian were discussed. In this Section we will not concentrate on the origin of b_0 and will perform the analysis of the system (4.20)–(4.21). The difference between “fundamental” and “plasma-induced” parity-odd self-energy (4.21) will be discussed in the Section 4.4.3 below.

The corresponding Hamiltonian of the system is given by

$$\mathcal{H}_A = \gamma^0 \big(\boldsymbol{\gamma} \cdot \boldsymbol{p} + m\big) + b_0 \gamma^5 \tag{4.22}$$

The dispersion relation of the fermions with the Lagrangian (4.20) is given by (see Appendix 4.A for details):

$$E_{\boldsymbol{p},\pm} = \sqrt{(|\boldsymbol{p}| \pm b_0)^2 + m^2} \quad \text{(particles)} \tag{4.23}$$

(and for anti-particles, the minus sign appears in front of the square root). It turns out that the operator of helicity (4.6) commutes with the Hamiltonian (4.22) and therefore *each particle with the energy* $E_{\boldsymbol{p},\pm}$ *has definite helicity:*[5]

$$h\,|E_{\boldsymbol{p},\pm}\rangle = \pm\,|E_{\boldsymbol{p},\pm}\rangle\,, \qquad E_{\boldsymbol{p},\pm} > 0 \tag{4.24}$$

The state of thermal equilibrium is described by $n_{\rm F}(E_{\boldsymbol{p},\pm})$. In the limit $m \ll |\boldsymbol{p}|$ and $|\boldsymbol{p}| \gg b_0$, the Fermi-Dirac distribution of fermions (4.23) reduces to

$$n_{\rm F}(E_{\boldsymbol{p},\pm}) \approx \frac{1}{\exp\left(\frac{|\boldsymbol{p}| \pm b_0}{T}\right) + 1}, \tag{4.25}$$

which looks like a Fermi-Dirac distribution for massless particles with chiral chemical potentials $\mu_{\rm L} = b_0$ and $\mu_{\rm R} = -b_0$. Clearly, one arrives to the same conclusion when putting $m = 0$ in the Hamiltonian (4.20) and considering the term (4.21) as the axial chemical potential term. Therefore, we expect that the model (4.20) at finite temperature emulates the chiral imbalance.

4.4.1 Homogeneous magnetic field

We have calculated the chiral magnetic current using the quantum-mechanical approach of [90], for massless particles with chiral asymmetry in Sec. 1.3.6, and for the asymmetrically populated state of massive fermions in Sec. 4.3. Here we want to extend this approach to the case of massive fermions with axial self-energy.

Lowest Landau level

In presence of electromagnetic field A_μ, the Dirac equation corresponding to the Lagrangian (4.20)–(4.21) is given by

$$(i\partial\!\!\!/ - m - eA\!\!\!/ - b_0 \gamma_0 \gamma^5)\psi = 0 \tag{4.26}$$

We will solve this equation for the static and homogeneous magnetic field, aligned in the z-direction, $\boldsymbol{B} = (0, 0, B)$ (we choose $eB < 0$, as before), and we choose

---

[5] Note the difference with the Dirac fermions, where a wave-function with a definite momentum $\boldsymbol{r}$ has fixed energy $\sqrt{\boldsymbol{r}^2 + m^2}$, but can have *both* helicities.

the Landau gauge, $A^\mu = (0, 0, xB, 0)$. Let us choose the ansatz $\psi = \exp(ip^z z + ip^y y)\chi F(x)$, where χ is a 4-component spinor, which does not depend on coordinates, and $F(x)$ is a scalar function of x only. The Dirac equation becomes

$$(\omega\gamma^0 - p^z\gamma^z - b_0\gamma_0\gamma^5 - m)F\chi + (-i\partial_x\gamma^x + p^y\gamma^y - exB\gamma^y)F\chi = 0 \quad (4.27)$$

To find the solution of the Eq. (4.27) we take the function $F(x)$ to be

$$F(x) = \exp\Big[-\frac{|eB|}{2}\left(x - \frac{p^y}{eB}\right)^2\Big] \quad (4.28)$$

so that

$$(-i\partial_x\gamma^x + p^y\gamma^y - exB\gamma^y)F\chi = 0 \quad (4.29)$$

where a spinor χ has a form $\chi = (0, \xi_1, 0, \xi_2)$. The solution of Eq. (4.27) is then reduces to

$$\begin{pmatrix} -m & \omega + p^z - b_0 \\ \omega - p^z + b_0 & -m \end{pmatrix}\begin{pmatrix} \xi_1 \\ \xi_2 \end{pmatrix} = 0. \quad (4.30)$$

As a result, we find the dispersion relation for the lowest Landau level

$$\omega = \pm\sqrt{(p_z - b_0)^2 + m^2} \quad (4.31)$$

as well as the normalized via $\chi^\dagger\chi = 1$ solution:

$$\xi_1 = \sqrt{\frac{\omega + p_z - b_0}{2\omega}}, \quad \xi_2 = \frac{m}{\sqrt{2\omega(\omega + p_z - b_0)}}, \quad (4.32)$$

In all of these expressions, the limit $b_0 \to 0$ corresponds to the case of usual Dirac fermions (with no axial self-energy).

Expectation value of the electric current

We now find the quantum mechanical expectation value of the operator of the electric current $j^z = e\hat{\bar{\psi}}\gamma^z\hat{\psi}$ in thermal equilibrium:[6]

$$\langle j^z\rangle_{\text{thermal}} = e\times\frac{|eB|}{2\pi}\int\limits_{-\infty}^{\infty}\frac{dp^z}{2\pi}n_{\text{F}}(\omega)\bar{\chi}\gamma^z\chi + \text{anti-particles}, \qquad \omega = \sqrt{(p^z - b_0)^2 + m^2} > 0 \quad (4.33)$$

---

[6] Below we consider only the contribution from the lowest Landau level, $n = 0$. The contributions of the $n \neq 0$ levels cancel each other, in the same manner as it happens in Sec. 4.3.1.

The prefactor $|eB|/2\pi$ is the transversal density of states, which is the number of localized Landau orbits per unit area in the $x0y$ plane, exactly as in the standard Landau levels' picture (cf. Sec. (1.3.6)). Since we have chosen $eB < 0$, $|eB| = -eB$. Observing that

$$\bar{\chi}\gamma^z\chi = \frac{p^z - b_0}{\sqrt{(p^z - b_0)^2 + m^2}} \tag{4.34}$$

we find that the expectation value of the current vanishes,

$$\langle j^z \rangle_{\text{thermal}} = 0 \tag{4.35}$$

Indeed, after the shift $p^z - b_0 \to p^{z'}$ the integral (4.33) becomes an integral of an odd function of $p^{z'}$ in the symmetric limits.

Let us now take into account the contribution of the filled Dirac sea, which is present even at zero temperature (in vacuum). Formally:

$$\langle j^z \rangle_{\text{vac}} = e \times \left(-\frac{eB}{2\pi} \right) \int\limits_{-\infty}^{\infty} \frac{dp^z}{2\pi} \frac{p^z - b_0}{\sqrt{(p^z - b_0)^2 + m^2}}, \tag{4.36}$$

which involves integral over all states with negative energy, $\omega < 0$ (the filled Dirac sea). The expression (4.36) is divergent at $p^z \to \pm\infty$. To make it finite, we notice that we are actually interested in the *change* of $\langle j^z \rangle$ that results from turning on the b_0 from $b_0 = 0$ at $t = -\infty$ to $b_0 \neq 0$. The resulting variation of the matrix element is

$$\left. \frac{\delta(\bar{\chi}\gamma^z\chi)}{\delta b_0} \right|_{\omega<0} = \frac{m^2}{|\omega|^3} \tag{4.37}$$

This variation is finite and therefore leads to

$$\frac{\delta \langle j^z \rangle_{\text{vac}}}{\delta b_0} = -\frac{e^2}{2\pi^2} B \tag{4.38}$$

which is the current that one could obtain from variation of the Chern-Simons term (1.37) with respect to A_z. Noting that in the massless case, $\mu_{\text{L}} = b_0$ and $\mu_{\text{R}} = -b_0$, we find that after the integration over b_0, the current $\langle j^z \rangle_{\text{vac}}$ coincides with the expression for the massless fermions, Eq. 4.5.

4.4.2 Inhomogeneous magnetic field

In this Section, we apply the imaginary-time (Matsubara) formalism to consider the theory (4.20)– (4.21) at finite temperature T. We compute the parity-odd part of the polarization tensor $\Pi_2^{ij}(i\omega_n = 0, \boldsymbol{q})$ at zero Matsubara frequency and check whether $\Pi_{\text{CS}} \neq 0$. The relevant diagram is the left diagram in Fig. 4.2. The polarization tensor is given by the formula

$$\Pi^{\mu\nu}(q) = ie^2 T \int \frac{d^3\boldsymbol{p}}{(2\pi)^3} \sum_{p^0 = i\omega_n} \text{Tr}\,[\gamma^\mu S_A(p) \gamma^\nu S_A(p-q)], \tag{4.39}$$

where $i\omega_n = i\pi(2n+1)T$ are fermionic imaginary frequencies (n is an integer),

$$S_A(p) = \frac{i}{\not{p} - m - \Sigma_A} = -i \frac{\left(\omega_n^2 + \boldsymbol{p}^{\,2} + m^2 + b_0^2 + 2b_0\gamma_0\gamma^5(\boldsymbol{\gamma}\cdot\boldsymbol{p})\right)\left(\not{p} + m - b_0\gamma_0\gamma^5\right)}{\left(\omega_n^2 + \boldsymbol{p}^{\,2} + m^2 + b_0^2\right)^2 - 4b_0^2\boldsymbol{p}^{\,2}} \tag{4.40}$$

is the fermion propagator, which explicitly takes into account the axial self-energy (4.21) and $\not{p} = i\omega_n\gamma_0 - \boldsymbol{\gamma}\cdot\boldsymbol{p}$ so that $p^2 = -(\omega_n^2 + \boldsymbol{p}^2)$. In the second equality (4.40) we identified explicitly the poles in the propagator. One can easily see that the poles of the denominator of (4.40) for $\omega_n = iE$ are precisely in the positions (4.23). For $m = 0$ the expression (4.40) splits into

$$S_A\Big|_{m=0} = iP_{\text{L}} \frac{1}{(i\omega_n + b_0)\gamma^0 - \boldsymbol{\gamma}\cdot\boldsymbol{p}} + iP_{\text{R}} \frac{1}{(i\omega_n - b_0)\gamma^0 - \boldsymbol{\gamma}\cdot\boldsymbol{p}} \tag{4.41}$$

— sum of two propagators of chiral fermions with chiral chemical potentials $\mu_{\text{L}} = b_0$ and $\mu_{\text{R}} = -b_0$.

In order to evaluate the expression, it is important to specify the order of integration over 3-momentum $\boldsymbol{p}$ and summation over frequencies p_0, as will become clear below.

We will be interested in the spatial, parity odd part of the expression (4.39) in the limit

$$m \ll T \quad ; \quad b_0 \ll T \quad ; \quad |\boldsymbol{q}| \ll T \tag{4.42}$$

and we keep *arbitrary* the ratios m/b_0 and $|\boldsymbol{q}|/m$.

Let us expand the expression (4.39) in powers of b_0/T. The zeroth-order term does not give parity-violating terms, since in absence of Σ_A there is no source of the violation of P-symmetry in (4.20). Therefore, we extract the first order in b_0 (see Fig. 4.3). Each of the terms is potentially ultraviolet-divergent (the naive counting of degree of divergence indicates *linear divergence*). The well-known ambiguity in defining linearly divergent integrals (see e.g. [227], Section on $\pi^0 \to \gamma\gamma$ decay) lead the authors of [226] to argue that the parity-odd contribution to the polarization operator (4.39) is zero in this case. However, the parity-odd part of the integral in (4.39) is always convergent (cf. the discussion in [224, 225], and the discussion below) if one takes into account that the integrand of the polarization tensor involves two fermion propagators, the expansion produces two different terms (Fig. 4.3). We do the computation of the sum of two triangular diagrams, keeping the original momentum routing in both terms, and do not make any shifts of the integration variable therein. The linear expansion of the result in $\boldsymbol{q}$ produces

$$\Pi_2^{ij} = 4e^2 b_0 q_k \epsilon^{ijk} T \int \frac{d^3\boldsymbol{p}}{(2\pi)^3} \sum_{p^0 = i\omega_n} \frac{3p_0^2 + \boldsymbol{p}^2 - 3m^2}{(p^2 - m^2)^3} \tag{4.43}$$

Computation of the Chern-Simons coefficient in Matsubara formalism

A number of important technical issues arises when one computes the integral (4.43) and we comment on them below. The integral in (4.43) has explicit splitting into one-dimensional and three-dimensional integrations (due to the breaking of the Lorentz invariance by the presence of plasma). Superficially this integral is logarithmically divergent (in the sum of two triangular graphs of Fig. 4.3, the linearly divergent terms are cancelled).

The sum over frequencies ω_n can be done explicitly and the resulting integral over $d^3\boldsymbol{p}$ is convergent and *non-vanishing.* If one starts however with the integration over momentum $\boldsymbol{p}$, one can easily see that

$$\int \frac{4\pi \boldsymbol{p}^2 d\boldsymbol{p}}{(2\pi)^3} \frac{-3\omega_n^2 + \boldsymbol{p}^2 - 3m^2}{(-\omega_n^2 - \boldsymbol{p}^2 - m^2)^3} = 0 \quad \forall\, \omega_n, m \tag{4.44}$$

Although both answers are convergent, we understand that the reason for it is the manipulation with the order of summation and integration for superficially divergent integrals. This is a rare example, when every regularization gives convergent answer, but the answers are different (see the discussion in [224, 225]).

How should we choose the correct regularization prescription? Fortunately, we know the answer in the massless case. Repeating the computations of the Section 4.4.2 for the propagator (4.41) we find that the integral (4.44) would also be zero in a purely massless case. Using the summation before the integration, on the other hand recovers the known result (4.5) (with the identification $b_0 = (\mu_\mathrm{L} - \mu_\mathrm{R})/2$.

Finally, performing first the summation over the Matsubara frequencies:

$$T \sum_n \frac{-3\omega_n^2 + \boldsymbol{p}^2 - 3m^2}{(-\omega_n^2 - \boldsymbol{p}^2 - m^2)^3} \tag{4.45}$$

and then the integration over $d^3\boldsymbol{p}$ we arrive to the following expression for the polarization operator in the system with axial self-energy (4.20)(4.21)

$$\Pi_2^{ij} = -i\frac{e^2}{2\pi^2} b_0 \epsilon^{ijk} q^k \quad (|\boldsymbol{q}| \ll m, \quad m \ll T). \tag{4.46}$$

This expression, again, looks like Eq. (4.5) under the identification $b_0 \leftrightarrow (\mu_\mathrm{L} - \mu_\mathrm{R})/2$ and it is valid for the finite fermion mass (with the relative corrections due to the mass of the order $(m/T)^2$).

We discuss the result (4.46) in the next Section.

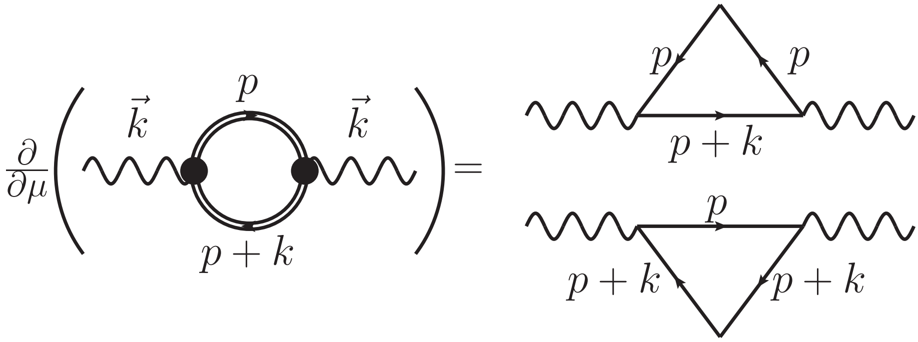

Figure 4.3: Differentiating Π_2 with respect to μ and putting $\mu = 0$ gives the following prescription of the loop momentum routing in triangular graphs as shown schematically on the Figure. Here the double line is the full propagator (4.40), while the propagators in the triangular graphs are free massive propagators without chemical potential. Please, note that this prescription for routing coincides with that of [225, 224].

4.4.3 Thermal and vacuum contributions to the parity-odd terms

The Matsubara formalism of the previous Section is technically simple, but makes the result (4.46) obscure. Why this expression is not suppressed by the mass and what is the difference with the previous example (Section 4.3.2) – we will clarify this in the current Section.

By definition, the thermal average $\langle\mathcal{O}\rangle_T$ is defined as a trace over the full system of states, *including* the vacuum state:

$$\langle \boldsymbol{j}\rangle_T = \langle 0|\, \boldsymbol{j}\, |0\rangle + \sum_{n,E_n\neq 0} \langle n|\, \boldsymbol{j}\, |n\rangle\, e^{-E_n/T} \tag{4.47}$$

where the system $\{|0\rangle, |n\rangle\}$ is a basis in the Hilbert space.

The Matsubara formalism computes the left hand side of the Eq. (4.47) for the current $\boldsymbol{j}$. The computation of the previous Section does not show what contributions are due to $|0\rangle$ or $\{|n\rangle\}$ states. The separation into the *vacuum part* $\langle 0|\,\mathcal{O}\,|0\rangle$ and *thermal contribution* (the sum over $E_n \neq 0$) in Eq. (4.47) can be done, using the following formal representation of the $\sum_n$ over Matsubara frequencies (see [228]):

$$T\sum_n f(\omega_n) = \frac{1}{2}\oint_{\mathcal{C}} \frac{d\omega}{2\pi i} f(\omega)\tan(\frac{\omega}{2T}) \tag{4.48}$$

where the contour $\mathcal{C}$ is shown as a solid line in Fig. 4.4. We can rewrite the r.h.s.

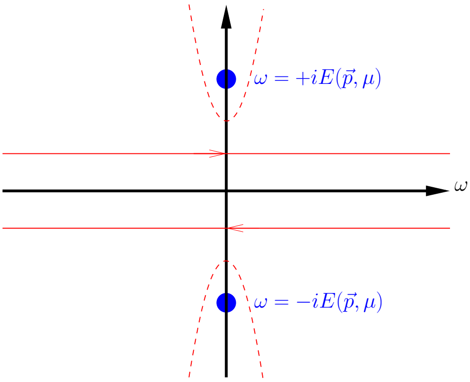

Figure 4.4: Choice of contours that allows to reduce the sum over Matsubara frequencies to the sum over filled states. The contour $\mathcal{C}$ in the integral (4.48) (red solid line) gets deformed into the dashed contour that feels only poles in the dispersion relation.

of (4.48) as a sum over the residues. The residues are computed in the "physical poles" – poles of the propagator (4.40).

Let us perform this computation in the simplest case of (4.45). The function $f(\omega)$ is in this case

$$f(\omega) = \frac{-3\omega^2 + \boldsymbol{p}^2 - 3m^2}{(-\omega^2 - \boldsymbol{p}^2 - m^2)^3} \tag{4.49}$$

The poles of this function are in $\omega = \pm\sqrt{\boldsymbol{p}^2 + m^2}$ and the residues of the expression (4.48) can be computed:

$$T\sum_n f(\omega_n) = \frac{3m^2}{4E_{\boldsymbol{p}}^5} + \frac{(\boldsymbol{p}^2E_{\boldsymbol{p}}^2 - 3m^2T^2 - 3m^2E_{\boldsymbol{p}}T)n_{\mathrm{F}}(E_{\boldsymbol{p}})}{2E_{\boldsymbol{p}}^5T^2} + (\dots)n_{\mathrm{F}}^2(E_{\boldsymbol{p}}) + (\dots)n_{\mathrm{F}}^3(E_{\boldsymbol{p}}) \tag{4.50}$$

The sum (4.50) contains several terms independent of temperature and a series of terms with the powers of Fermi-Dirac distribution functions, $n_{\mathrm{F}}(E_{\boldsymbol{p}})$. This result is generic: any Matsubara sum splits into the "vacuum" part that does not depend on temperature and is equivalent to the vacuum QFT expression, integrated over ω *and* into sum over thermal states (weighted by the Fermi-Dirac distributions). In our case there is the only first term in (4.50), that is temperature-independent.[7] The integration of the r.h.s. of Eq. (4.50) over $d^3\boldsymbol{p}$ reveals that the integral of all terms, containing $n_{\mathrm{F}}(E_{\boldsymbol{p}})$ is zero, while the integral

---

[7] If we did not expand the original expression in b_0/T, the thermal contributions would include Fermi-Dirac distributions evaluated for both $E_{\boldsymbol{p},\pm}$ given by (4.23).

over the first term is non-zero and leads to

$$\Pi_{\text{CS}} = \frac{e^2 b_0}{2\pi^2} \qquad \text{(Fermions with axial self-energy, zero-temperature contribution)} \tag{4.51}$$

Thus, even at *zero temperature*, the parity-odd part of the polarization tensor, Π_2, or, equivalently, the current (4.5) with $\mu_L - \mu_R \leftrightarrow 2b_0$ exists in the system (4.20)–(4.21) for arbitrarily small $|\boldsymbol{q}|$ (i.e. in the limit $|\boldsymbol{q}| \ll m$).

What we have discovered here is actually a known result [224]. The photon polarization tensor in the model with axial self-energy was previously studied in Ref. [224] that considered the CPT-violating fermion self-energy at a fundamental level. There it was shown that indeed the Chern-Simons term (1.37) is generated in such an electrodynamics in the absence of medium. In the subsequent discussion [226, 225] authors argued that the resulting expression depends on the regularization prescription.

Pure massless case

It is instructive to repeat the previous computation in the model (4.20)–(4.21) but with $m = 0$. Performing the sum as in (4.50), we will find an expression

$$T \sum_n f_{m=0}(\omega_n) = \frac{1}{2pT^2} \Big(2n_{\text{F}}^3(p) - 3n_{\text{F}}^2(p) + n_{\text{F}}(p) \Big) \tag{4.52}$$

Notice that *all terms* in the r.h.s. of Eq. (4.52) are temperature-dependent, and there is no analog of the first term from the sum (4.50). However, it *does not mean* that the vacuum contribution to Π_{CS} vanishes! Indeed, integrating the expression (4.52) over $d^3\boldsymbol{p}$ we get the same answer as (4.51): $\Pi_{\text{CS}} = \frac{e^2 b_0}{2\pi^2}$, which is temperature-independent! The reason is that no matter how small T is, the dominant part of the integral comes from the region $p \lesssim T$, where $n_{\text{F}} \sim 1$, and we deal with the integral $\sim \int_0^T p^2 dp/pT^2 \sim 1$, which does not vanish in the limit $T \to 0$. Therefore, the answer $\Pi_{\text{CS}} = \frac{e^2 b_0}{2\pi^2}$ comes from vacuum, and does not receive finite-temperature corrections, like in the previous calculation with $m \neq 0$! The difference with the case $m \neq 0$ comes from the fact that the energies of massive fermions are bounded by m from below, therefore the Fermi distribution for any momentum p is suppressed at least as $\exp(-m/T)$ in the limit $T \ll m$. On the other hand, massless fermions do not receive such a suppression, and there exists range of low momenta ($p \lesssim T$) where the distribution function is unsuppressed.

$$\Pi_{\text{CS}} = \frac{e^2 b_0}{2\pi^2}, \quad \text{(vacuum contribution)}, \tag{4.53}$$

$$\Pi_{\text{CS}} = 0, \quad \text{(thermal contribution)} \tag{4.54}$$

Why this happens can be understood from another perspective. For massless fermions, one can find Π_{CS} without expansion in b_0, by recalling that in this case the fermionic propagator splits into the sum of left- and right-chiral propagators (4.41). Therefore, the polarization tensor splits into sum of two integrals, and the expansion in linear order in q together with the frequency summation will give

$$\Pi_{\text{CS}} \propto \int\limits_0^\infty dp(n_{\text{F}}(p-b_0) - n_{\text{F}}(p+b_0)) \sim b_0. \tag{4.55}$$

Although the integrand is proportional to the Fermi distribution, it does not vanish in absence of medium. Indeed, the absence of medium corresponds to the limit $T \to 0$ while keeping b_0 fixed (since b_0 is a vacuum property of fermion, which remains non-zero after the removal of medium). In this limit, $n_{\text{F}}(p \pm b_0) \to \theta(-(p \pm b_0))$, where $\theta(x)$ is the Heaviside step function, which gives non-zero Π_{CS}. Once we add the medium back by turning on temperature, we see that the coefficient Π_{CS} does not change.

Short wave-length regime

Finally, let us analyse the same system in the limit $m \ll |\boldsymbol{q}| \ll T$. One can expect that this limit is similar to the case of massless fermions.

Note that the result (4.46) is applicable only in linear order in $\boldsymbol{q}/m$. As an additional step, we have evaluated the polarization tensor *without* expansion in external momentum. In the limit $|\boldsymbol{q}| \gg m$ the numerical evaluation of the parity-odd part of (4.39) gives

$$\Pi_{\text{CS}} = \mathcal{O}\left(\frac{m^2}{q}\right) \quad (m \ll |\boldsymbol{q}| \ll T, \quad \text{medium contribution}). \tag{4.56}$$

$$\Pi_{\text{CS}} = \frac{e^2}{2\pi^2} b_0 \quad (m \ll |\boldsymbol{q}| \ll T, \quad \text{vacuum contribution}), \tag{4.57}$$

This result coincides with the massless case, which is considered above, as it was expected. Note, that Eqs. (4.46) and (4.57) have identical form, although the relation between photon wavenumber and electron mass are different, and in both cases the dominant contribution comes from vacuum, while the medium corrections are suppressed.

4.5 Gauge invariance and Chern-Simons term

Medium corrections to the effective action of electromagnetic field are caused by the interactions of the probe electromagnetic field (photon) with plasma. In particular, we have seen that in the case *(I)*, the effective action is expressed through the forward scattering amplitude $\mathcal{M}^{\mu\nu}$ of photon by electron, Eq. (4.17).

Using the expansion (4.70) of the fermion propagator with axial self-energy (4.40) in terms of the eigenfunctions χ of the Hamiltonian (4.22), and evaluating the sum over frequencies according to Eq. (4.48), one can see that the thermal part of the polarization tensor (4.39) for the case *(II)* takes the form

$$\Pi^{\mu\nu}(q) = \int d^3r \sum_{s=\pm} \left[n_{\rm F}(E_{\boldsymbol{r}s}) \mathcal{M}_A^{\mu\nu} + \text{anti-particles} \right], \tag{4.58}$$

where

$$\mathcal{M}_A^{\mu\nu} = ie^2 \bar{\chi}_s(\boldsymbol{r}) [\gamma^\mu S_A(r+q)\gamma^\nu + \gamma^\nu S_A(r-q)\gamma^\mu] \bar{\chi}_s(\boldsymbol{r}) \tag{4.59}$$

is the forward scattering amplitude of fermions dressed with axial self-energy. The polarization tensor (4.58) is expressed via the scattering amplitude in the way that is very similar to the case *(I)* (Eq. (4.17)).

Although in both cases *(I)* and *(II)* only the *forward* amplitude is involved in the expression for the polarization tensor (or electric current), one can consider the scattering amplitude in a more general kinematic regime, when the initial photon with momentum q scatters into a state with a *different* momentum q'. As a consequence of the gauge invariance this amplitude is transversal:

$$q_\mu \mathcal{M}^{\mu\nu}(q,q') = 0, \quad q'_\nu \mathcal{M}^{\mu\nu}(q,q') = 0. \tag{4.60}$$

From these two independent relations, one may argue that the amplitude is at least second-order in photon momenta, $\mathcal{M}(q,q') \propto \mathcal{O}\big(q^2, (q')^2, (q\cdot q')\big)$ (the argument essentially repeats that of [229]) and therefore, after thermal averaging in Eq. (4.17) it is not expected to give $\mathcal{O}(q)$ term. However, the amplitude is explicitly *non-analytic* in q and q'. Indeed, in the case $q = q' = 0$ the expression (4.17) is actually singular, since the intermediate electrons become on-shell. Therefore, the transversality of the amplitude does not imply absence of $\Pi_{\rm CS}$. The important relation between the analyticity, gauge invariance and presence of the Chern-Simons term will be actively used in Chapter 5.

4.6 Discussion

In this Chapter, we have considered the Chiral Magnetic Current for massive fermions, for two different scenarios, which are both realized in the νMSM . In the first scenario, the left- and right-helical fermions are populated asymmetrically in plasma, and the timescales that we consider are large enough for each sort of the helical particles to come into quasi-thermal equilibrium individually. At the same time, we choose this timescale to be small enough so that the disbalance in populations does not relax to zero due to chirality-flipping reactions. For this setup, we conclude that there exists electric current proportional to magnetic field in the limit $q \ll m$ of wavenumbers q that are much smaller than the fermion mass m. The current (4.19) has the same form as in the case of massless particles.

The result (4.19) is valid to the order $\mathcal{O}(e^2)$ and exact in T. Higher-order corrections $\mathcal{O}(e^{2+n})$ will lead in particular to the helicity-flipping contributions that will drive the asymmetry in populations to zero. These processes determine the timescale of helicity-flipping and thus the timescale on which Eq. (4.19) is valid. In the context of the νMSM , one has to compare the rate of helicity-flipping reactions with the rate of the development of instability against the growth of large-scale magnetic fields.

In the second scenario, we do not introduce chemical potentials, but modify instead the dispersion relation of Dirac fermions, by adding the axial self-energy. This modification breaks down the parity symmetry, and in the state of exact thermal equilibrium, the distribution functions of relativistic particles coincide with the Fermi distribution of massless fermions with chiral chemical potential. Although one would expect that the electric current is the same as in the scenario with asymmetric population, the relation between the two cases turns out to be more subtle. We employ the standard and straightforward method for systems in thermal equilibrium – the Matsubara (imaginary-time) formalism. Although in the long-wavelength limit $q \ll m$ this method gives the same Chiral Magnetic Current, as in the case of asymmetric population, we point out that the dominant contribution to the current is temperature-independent, while the medium correction to this contribution is suppressed. The temperature-independent part is present in vacuum, and evaluation by standard zero-temperature methods reveals that the contribution is ultraviolet divergent (with logarithmic degree of divergence). Thus, the current in second scenario depends on regularization, and becomes ambiguous. Matsubara formalism only provides a particular regularization prescription, which is no better than the other prescriptions.

As we have noticed before, the parity-violating correction to the Lagrangian (axial self-energy) appears effectively as a result of weak interactions in plasma. The mentioned ultraviolet ambiguity for the vacuum term is a feature of models with local 4-fermion interaction, but in a realistic renormalizable theory (like the Standard Model) there is an intermediate boson (W-boson or Z-boson), which makes the 4-fermion interaction non-local, and results in *well-defined* vacuum terms. In Chapter 5, we consider the fate of the Chern-Simons term induced by parity-violating interactions of a renormalizable theory.

Appendices

4.A Quantum mechanics of fermions with axial self-energy

Below we provide necessary details about the single-particle quantum mechanics of fermion with axial self-energy, central for the Sections 4.4 of this work. There results are fairly straightforward, however, to our knowledge they have not been worked out in necessary details in monographs and research papers. Therefore, we present this Appendix for completeness.

Starting from the Hamiltonian (4.22),

$$\mathcal{H}_A = \gamma^0 \boldsymbol{\gamma}(-i\boldsymbol{\nabla}) + m\gamma^0 + b_0\gamma^5 \,, \tag{4.61}$$

we search for the plane wave solutions with the 3-dimensional wavevector $\boldsymbol{r}$, pointing along z-axis, $\boldsymbol{p} = (0,0,p)$, $p > 0$. Then the eigenstates of the Hamiltonian are

$$\chi_- \propto \begin{pmatrix} 0 \\ m \\ 0 \\ E_{\boldsymbol{p},-} - (p - b_0) \end{pmatrix} e^{ipz}, \quad \mathcal{H}\chi_- = E_{\boldsymbol{r},-}\chi_-, \tag{4.62}$$

$$\chi_+ \propto \begin{pmatrix} m \\ 0 \\ E_{\boldsymbol{p},+} + (p + b_0) \\ 0 \end{pmatrix} e^{ipz}, \quad \mathcal{H}\chi_+ = E_{\boldsymbol{p},+}\chi_+, \tag{4.63}$$

$$\psi_- \propto \begin{pmatrix} 0 \\ E_{\boldsymbol{p},-} - (p - b_0) \\ 0 \\ -m \end{pmatrix} e^{ipz}, \quad \mathcal{H}\psi_- = -E_{\boldsymbol{p},-}\psi_-, \tag{4.64}$$

$$\psi_+ \propto \begin{pmatrix} -m \\ 0 \\ E_{\boldsymbol{p},+} - (p + b_0) \\ 0 \end{pmatrix} e^{ipz}, \quad \mathcal{H}\psi_+ = -E_{\boldsymbol{p},+}\psi_+ \tag{4.65}$$

$$E_{\boldsymbol{p},-} = \sqrt{(p-b_0)^2+m^2}, \quad E_{\boldsymbol{p},+} = \sqrt{(p+b_0)^2+m^2} \tag{4.66}$$

We have two positive-energy branches of solutions (χ_+ and χ_-) and two negative-energy branches (ψ_+ and ψ_-), which are divided by the energy gap $2m$. In order to make physical sense of this model, let us fill all the negative-energy levels, and call this state vacuum (so the vacuum is actually the filled Dirac sea). Then the interpetation of the positive-energy branches remains unchanged: χ_- is an electron with energy $E_{p,-}$ and momentum $\boldsymbol{p}$, χ_+ is an electron with energy $E_{p,+}$ and momentum $\boldsymbol{p}$.

The values of helicities for these states can be recovered from the observation that the spin operator for electrons is the same as for usual Dirac particles,

$$\hat{\boldsymbol{s}} = \frac{1}{2}\begin{pmatrix} \boldsymbol{\sigma} & 0 \\ 0 & \boldsymbol{\sigma} \end{pmatrix}, \tag{4.67}$$

so that the helicity operator has the form (4.6). As a result, χ_- corresponds to negative helicity, and χ_+ – to positive helicity. That these states can have definite energy and definite helicity at the same time, can be understood from the commutation property

$$[\hat{\mathcal{H}}_A(\boldsymbol{p}), \hat{h}(\boldsymbol{p})] = 0 \tag{4.68}$$

which is valid for non-zero b_0, as well as for the case of Dirac fermions (when $b_0 = 0$).

The state with an unoccupied negative-energy level in the filled Dirac sea is a hole, and corresponds to positive-energy and positive-charged particle (all of the other quantum numbers, like spin projection on z axis, should be flipped). The spinor of this state is the charge-conjugation of ψ_- (ψ_+), the energy is $E_{\boldsymbol{p},-}$ ($E_{\boldsymbol{p},+}$) the momentum is $-\boldsymbol{p}$, and the helicities is negative (positive).

Assuming $b_0 \ll m$, one can note that for $p \gg m$, left-chiral components of ψ_1 and ψ_4 dominate over their right-chiral components, and vice versa for ψ_2 and ψ_3. In this relativistic regime, we can expand the energy in powers of b_0/p, and find that

$$E_{\boldsymbol{p},-} \approx \sqrt{\boldsymbol{p}^2+m^2} - b_0, \quad E_{\boldsymbol{p},+} \approx \sqrt{\boldsymbol{p}^2+m^2} + b_0. \quad (p \gg m) \tag{4.69}$$

It means that the energies of left-helical electrons and positrons are shifted by b_0 downwards, while the energies of right-helical electrons and positrons are shifted by b_0 upwards, with respect to the case of pure Dirac fermions. however, for the mid- and non-relativistic particles, the expansion (4.69) is not valid.

Finally, we want to notice that the fermionic propagator (4.40) can be expanded in the wavefunctions as

$$S_A(\omega, \boldsymbol{p}) = \frac{i}{\not{p} - m - \Sigma_A} = i\sum_{s=\pm}\left(\frac{\chi_s(\boldsymbol{p})\bar{\chi}_s(\boldsymbol{p})}{\omega - E_{\boldsymbol{p},s}} + \frac{\psi_s^C(-\boldsymbol{p})\bar{\psi}_s^C(-\boldsymbol{p})}{\omega + E_{\boldsymbol{p},s}}\right), \tag{4.70}$$

where $\psi^C \equiv i\gamma^2\psi^*$ is the charge-conjugated spinor.

Chapter 5

Chiral Magnetic Effect from parity-violating interactions

5.1 Chern-Simons term as a result of particle interactions

As we have seen before, the presence of chiral asymmetry in a medium of relativistic particles can have drastic consequences for the dynamics of primordial plasma. Namely, the medium can become *unstable* towards the spontaneous generation of long wavelength magnetic fields [202, 91, 92]. However, all the electrically charged particles are massive in the Standard Model and therefore the notion of *chirality* can be only approximate for them. Any asymmetry in numbers of left- and right-chiral particles, created in equilibrium will be quickly erased due to the chirality-flipping reactions, driven by the finite fermion mass m. As we have argued in Chap. 4, although in the regime $m \ll T$, the rate of chirality-flipping reactions Γ_f is strongly suppressed with respect to chirality-preserving reactions, this rate Γ_f is still extremely high, which means that the chirality gets quickly erased on the timescale of the lifetime of the Universe, $t \sim H^{-1}$, at temperatures below ~ 80 TeV [95]. However, if sterile neutrinos inject large chiral asymmetry very fast, at $t \ll \Gamma_f^{-1}$, then the Chiral Magnetic Current is developed, which is proportional to this asymmetry. According to Sec. 1.3.5, it means that the parity-odd term (Chern-Simons term) is produced in the free energy of electromagnetic field (1.35).

Recently, however, it has been argued, that due to the parity-violating nature of weak interactions, the chiral asymmetry is produced effectively, in the states with large lepton asymmetry [98]. Below we discuss this mechanism in more detail.

In our discussion of the Chiral Magnetic Effect above (case *(I)* from Chap. 4), we have considered the particles as non-interacting entities. However, for the case of *dense* medium, each individual particle becomes dressed by presence of the background of all the other particles, so that its properties are modified as compared to vacuum (see similar discussion in Sec. 1.3.1 about neutrinos in the early Universe). If we consider an electron, for definiteness, and take into account the dressing due to his dominant interaction, the electromagnetic interaction, we find that the left and right electrons are dressed in the same way. Indeed, electromagnetic interactions themselves obey P-symmetry, the state of plasma is also P-symmetric in absence of chiral asymmetry, so the properties of the two types of particles, which are related to each other by the transformation under parity, are identical.

On the other hand, electrons participate as well in weak interactions, which violate parity. In analogy to neutrinos in the dense medium, electrons in medium are described by the effective Dirac equation

$$(i\partial_\mu \gamma^\mu - \Sigma_A - m)e(x) = 0, \tag{5.1}$$

where Σ_A is the medium self-energy correction of electron (similar to Eq. (1.12) for neutrinos) [51, 230, 98]

$$\Sigma_A \sim G_F L \gamma^0 \gamma^5, \tag{5.2}$$

where L is the density of lepton number.[1]

In order to understand Eq. (5.2) better, one can note that on the one hand, the expression (5.2) violates the combined symmetry CP (which corresponds to subsequent application of charge C and P transformations). On the other hand, according to the SM, weak interactions of leptons preserve CP, the state $L = 0$ is symmetric under CP, therefore, in absence of lepton asymmetry, Σ_A vanishes.[2]

The modified Dirac equation (5.1) with axial self-energy (5.2) has been already analyzed in Chap. 4 (it was called case *(II)*, and the parameter b_0 therein is $b_0 \sim G_F L$). And we have seen, that left and right electrons with given momentum are described by *different* energies in medium, so that their occupation numbers differ even in the state of thermal equilibrium, when the chirality-flipping processes have lead to $\mu_\mathrm{L} - \mu_\mathrm{R} \to 0$. As a result, we have found that indeed, the *effective* chiral asymmetry is developed. Our conclusion was that in this setup, the Chern-Simons term may be induced,

$$\Delta\mathcal{L}_\mathrm{CS} \sim G_F L \int d^3x \boldsymbol{A} \cdot \boldsymbol{B}. \tag{5.3}$$

---

[1] Here we write only the parity-odd part of the self-energy induced by weak interaction. But there exists parity-even part, which renormalizes left and right particles in the same way (similarly to the case of electrodynamics considered above), and is not relevant for our further discussion.

[2] CP violation happens in weak interactions of *quarks*, which leads to oscillations of K^0 mesons into $\overline{K^0}$, and similar oscillations of B^0 mesons into $\overline{B^0}$. However, according to the experimental data, the relative magnitude of this violation is very small.

At the same time, in the discussion of the case *(II)* in Chap. 4 we have implicitly assumed that the only way the medium renormalizes the properties of particles is through appearence of the self-energy (5.2). Another assumption was that this self-energy does not depend on particle momentum, which is true as long as 4-fermion Fermi interaction is taken to be local. Below, we take into account the medium effects *systematically*, in the framework of a theory with two Abelian gauge fields ($U(1)\times U(1)$ theory). One gauge field ("vector" gauge field) is massless and couples the same way to left- and right-chiral particles, the other field ("chiral" gauge field) is heavy, and couples asymmetrically to left and right chiralities. This model is a simplified version of the Standard Model, which captures its essential features: presence of massless "electromagnetic" field which does not distinguish electric charges of different fermion chiralities, and the intrinsic parity-violation, induced by coupling of fermions to W and Z bosons. At the same time, the $U(1)\times U(1)$ model is simpler, since it does not involve Yang-Mills interactions of the electroweak bosons, and has only two gauge bosons instead of four. In the $U(1)\times U(1)$ theory, the parity-violating 4-fermion coupling appears as a result of exchange of the heavy chiral field, and is therefore *non-local*.

In Sec. 5.2 we describe the $U(1)\times U(1)$ in more detail, and classify the medium contributions to the parity-odd part of the polarization tensor. The two different classes are studied in Sections 5.3 and 5.4, respectively. We conclude that the sum of diagrams inside each of the classes vanishes separately, so that no Chern-Simons term is induced in the state of thermal equilibrium ($\mu_{\rm L} = \mu_{\rm R}$), even in presence of non-zero lepton asymmetry.

5.2 Theory with $U(1)_{\mathbf{vector}} \times U(1)_{\mathbf{axial}}$ gauge group

We consider a model based on $U(1)\times U(1)$ gauge symmetry, where one of the gauge fields is massless (we will call it γ or "photon") and has vector-like couplings e_f with fermions, the other gauge field is massive (we will call it Z-boson) and has different couplings with left and right fermions, g_{Lf} and g_{Rf}, respectively. Difference in couplings provides explicit violation of P-symmetry at the level of particle interactions, and the Lagrangian is[3]

$$\mathcal{L} = \sum_f \bar\psi \left[i\gamma^\mu \left(\partial_\mu + ieA_\mu - i(g_L P_L + g_R P_R)Z_\mu\right) - m\right]\psi - \frac{1}{4}F_{\mu\nu}F^{\mu\nu} - \frac{1}{4}Z_{\mu\nu}Z^{\mu\nu} + \frac{1}{2}M_Z^2 Z_\mu Z^\mu, \tag{5.4}$$

where $F_{\mu\nu} = \partial_\mu A_\nu - \partial_\nu A_\mu$, $Z_{\mu\nu} = \partial_\mu Z_\nu - \partial_\nu Z_\mu$ are the strength tensors of the massless and massive gauge fields, respectively. For simplicity of notation, we have

---

[3] More general form includes the mixing term $Z_{\mu\nu}F^{\mu\nu}$, which leads to appearence of the $Z\gamma$ vertex in perturbation theory. However, we choose the value of this vertex to be zero for momentum $q = 0$, which enters the vertex. But a non-zero vertex contribution is nevertheless generated in the effective action for the other momenta, due to loop corrections (for example, by creation of a virtual fermion-antifermion pair).

dropped the flavour index f in fermionic fields, couplings and masses. Projectors $P_L = (1-\gamma^5)/2$, $P_R = (1+\gamma^5)/2$ extract states with definite chiralities. In order for this theory to be self-consistent, we choose the gauge charges such that all the gauge anomalies cancel.

Note that the theory (5.4) is not unitary by itself. For example, the tree-level process $f_L^- Z \to f_R^- Z$ violates unitarity of the S-matrix at high energies, provided that the coupling are indeed chiral, $g_{Lf} \neq g_{Rf}$. We overcome this difficulty by introducing an (Abelian) Higgs field, which provides finite mass to Z-boson after the spontaneous symmetry breaking. The resulting model is renormalizable. On the other hand, the additional neutral scalar particle h, which appears after the symmetry breaking, is not relevant to what is discussed below in our work, therefore we omit this degree of freedom. For convenience, we choose also a non-unitary gauge, $\xi = 1$. As a result, intermediate Goldstone bosons appear in our analysis, however, they do not contribute to the parity-odd part of the polarization tensor.

We consider fermionic masses m_f, which are much smaller than the temperature T, and temperature by itself is much smaller than the mass of Z-boson, $m_f \ll T \ll M_Z$ (we will call the fermions “leptons”, and the lightest one we will call “electron”). According to the logic given above, we are interested in the situation where the difference of chemical potentials for different chiralities has relaxed to zero, so that left and right fermions share common chemical potential μ (which can be, nevertheless, different for different flavours f).

What is then the expected order of magnitude of the parity-odd polarization tensor? On the one hand, Π_2 is expected to involve at least two electromagnetic vertices, $ff\gamma$, since we have two electromagnetic fields in the effective action (1.35). On the other hand, violation of parity appears due to the exchange of an intermediate Z-boson, which means, that at least two vertices ffZ are present as well. As a result $\Pi_2 \propto e^2 g^2$, where g is either g_L or g_R. There are several classes of contributions, in this order of perturbation theory.

One class is given by two-loop *vacuum* diagrams with one or two fermion loops and one intermediate Z-boson. However, this class does not give parity-odd contributions to the polarization tensor (in the considered $\mathcal{O}(q)$ approximation), since any of such terms would contradict the Lorentz invariance. Therefore, the relevant contribution may be expected to appear only from presence of medium. It is worth noting at this point, that the density of real Z-bosons is suppressed by the Boltzmann factor $\exp(-M_Z/T)$, which is negligibly small, according to our assumption $T \ll M_Z$. On the other hand, real fermions in plasma are relativistic, $m \ll T$, and do not experience such a dramatic Boltzmann suppression. As a conclusion, we will consider only virtual Z-bosons, while fermions can be either virtual, or real.

The class with one initial and one final real fermion can be interpreted as Compton scattering process, in analogy with quantum electrodynamics. The typical diagrams are given in Figs. 5.1, 5.2, and each of them involves one (vacuum) loop integration, the same as one has in absence of medium. Therefore, this class

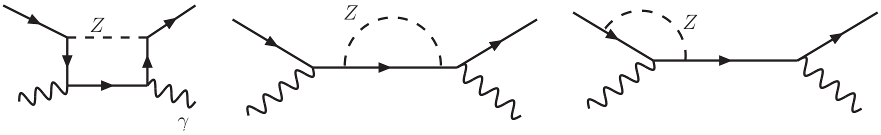

Figure 5.1: The first subclass of parity-violating vacuum 1-loop diagrams of the $f\gamma \to f\gamma$ scattering. The wavy line corresponds to photon, the line with arrow corresponds to the fermion f, the dashed line corresponds to the massive boson. Here one must include also diagrams with permutations of the $ff\gamma$ and ffZ vertices.

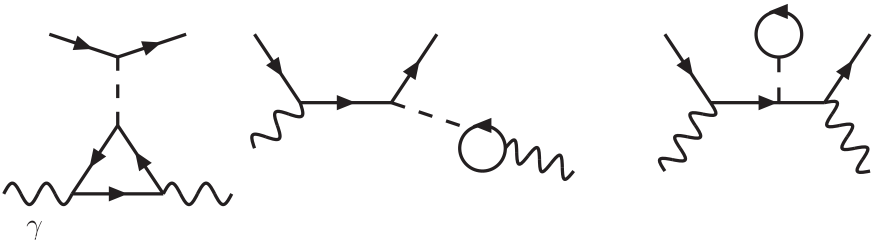

Figure 5.2: The second subclass of vacuum 1-loop diagrams of the $f\gamma \to f\gamma$ scattering in the $U(1) \times U(1)$ model.

will be referred to as "vacuum 1-loop corrections", and is discussed in detail in Sec. 5.3. The conclusion is that the sum of all these corrections is zero in the first order in photon momentum, owing to the electromagnetic gauge invariance, the analyticity of each term in the sum with respect to photon momentum, and the cancellation of chiral anomalies.

There is another class, with *two* initial fermions, and two outgoing fermions, and some of its representatives are given in Fig. 5.3. The diagrams inside this class, however are singular in the limit of the vanishing photon momentum q, and require special resummation. Unlike the diagrams from Fig. 5.1, the resulting resummed diagrams are non-analytic in q, and therefore the argument of gauge invariance does not imply that they are $\mathcal{O}(q^2)$, so it is possible that $\Pi_2 \neq 0$. However, we show that the total contribution of diagrams from Fig. 5.3 gives $\Pi_2 = 0$.

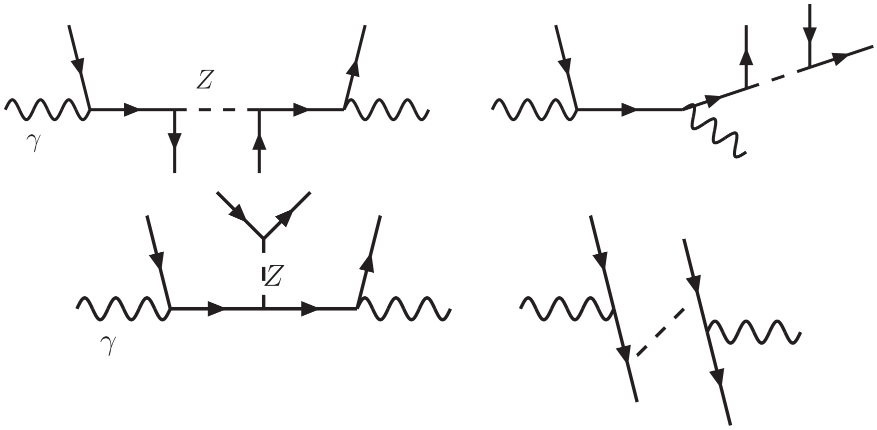

Figure 5.3: Some of the processes of the parity-violating $ff\gamma \to ff\gamma$ scattering.

5.3 1-loop vacuum corrections to Compton scattering

In this Section, we describe the contributions to Π_2 from class of diagrams with one initial real fermion, and one final real fermion. It is argued that separately these contributions are non-vanishing, but their total sum is zero.

Some of the considered diagrams are depicted in Figs. 5.1 and 5.2. (One also has to include the charged-conjugated processes, $\bar{f}\gamma \to \bar{f}\gamma$.) For a given diagram, the partial contribution to polarization tensor is

$$\Pi^{ij} = + \int \frac{d^3r}{(2\pi)^3} n_F(\epsilon_r - \mu) \sum_s i\mathcal{M}^{ij}, \tag{5.5}$$

where $n_F(x) = (\exp(\beta x) + 1)^{-1}$ is the Fermi distribution, $\epsilon_r = \sqrt{\boldsymbol{r}^2 + m^2}$ is the fermion energy, μ is the chemical potential, s is one of two possible polarization states of fermion, $\mathcal{M}^{ij}$ is the quantum-mechanical scattering amplitude. More precisely, $\mathcal{M}^{ij}$ is the amputated amplitude, which is derived from the actual amplitude $\mathcal{M}$ by removing the polarization vectors ϵ of photons, so that $\mathcal{M} = \mathcal{M}^{\mu\nu}\epsilon_\mu\epsilon_\nu$. Everywhere in what follows, when amplitude is mentioned, we actually mean this kind of amputated amplitude.

The diagrams in Fig. 5.1 do not split into disconnected parts after cutting the Z-boson line. It is natural to call the first diagram the “box” diagram, the second - as the fermion propagator renormalization (or as vacuum self-energy), the third - as the vertex renormalization. The propagator renormalization can be expressed in terms of the vacuum self-energy $\Sigma_{\text{vac}}(p)$, while the vertex renormalization - in terms of the vacuum vertex correction $\Gamma^\mu(p, p')$. For example, the second and the third diagrams from Fig. 5.1 are, respectively,

$$\mathcal{M}^{\mu\nu}_{\Sigma} = +ie^2\bar{u}(p')\gamma^\nu S(p+q)\Sigma_{\rm vac}(p+q)S(p+q)\gamma^\mu u(p), \tag{5.6}$$
$$\mathcal{M}^{\mu\nu}_{\rm vert} = -e\ \bar{u}(p')\gamma^\nu S(p+q)\Gamma^\mu(p+q,p)u(p). \tag{5.7}$$

Here we have considered more general kinematic situation of scattering, when the photon momentum may change, $q \neq q'$, while for evaluation of Π_2^{ij} we need only $q = q'$. Using the explicit expressions for $\Sigma_{\rm vac}$ and Γ^μ, one finds that each of the amplitudes is *analytic* in photon momenta q, q'.

On the other hand, the Ward identities hold

$$(p-p')_\mu\Gamma^\mu(p,p') = e[\Sigma_{\rm vac}(p') - \Sigma_{\rm vac}(p)], \tag{5.8}$$

$$q_\mu {\rm Box}^{\mu\nu}(p,p';q,q') = e[\Gamma^\nu(p-q',p) - \Gamma^\nu(p',p'+q')], \tag{5.9}$$

where ${\rm Box}^{\mu\nu}$ is the sum of box amplitudes, in which not only the polarization vectors of photon are removed, but the spinors $u(p)$, $u(p')$ of the external fermions are absent as well. (We have checked these identities explicitly.) As a result, the total amplitude of the box, self-energy and vertex-renormalization channels satisfies the transversality property[4]

$$q_\mu\mathcal{M}^{\mu\nu}(q,q') = q'_\nu\mathcal{M}^{\mu\nu}(q,q') = 0 \tag{5.10}$$

These two properties imply, that longitudinal photons are neither emitted, nor absorbed. Note, however, that each of the amplitudes separately, for example $\mathcal{M}_\Sigma$, does not satisfy the transversality property. Together with the property of analyticity, we find as a corollary, that the total amplitude is at least second-order in photon momentum, $\mathcal{M}^{\mu\nu} = \mathcal{O}(q^\alpha q^\beta)$, for the forward regime of Compton scattering, when one puts $q = q'$. Therefore, these channels do not produce $\mathcal{O}(q)$ term in the polarization tensor (5.5).

At this point, one may ask, if the similar agrument is applicable to the result Vilenkin et al. Indeed, the expression, which is derived therein, can be obtained by plugging the *tree-level* Compton scattering amplitude in (5.5). However, although this tree-level amplitude is gauge-invariant, it is explicitly *non-analytic* in photon momentum (actually, the amplitude is singular at vanishing momentum q). Therefore, the property of gauge invariance does not forbid the presence of $\mathcal{O}(q)$ term in polarization tensor, in that model.

Contrary to the diagrams in Fig. 5.1, each of the diagrams in Fig. 5.2 *does* split into two disconnected parts after cutting the Z-boson line. The first diagram in that Figure involves the vacuum triangle diagram, more precisely the sum of

---

[4] In the on-shell renormalization, which we use, there are two distinct box diagrams, two self-energy diagrams, and four vertex-renormalization diagrams for the scattering $f\gamma \to f\gamma$. The same number of diagrams appears for the charge-conjugated process $\bar{f}\gamma \to \bar{f}\gamma$.

the triangle diagrams with the different possible fermion species, which run in the loop. As it was mentioned above, we consider the model, where the gauge charges are chosen in a way to prevent chiral gauge anomalies, therefore the sum of such triangles vanishes identically.

The second diagram in Fig. 5.2 is not analytic. This diagram comprises the 1-loop correction $\Pi^{\alpha\beta}_{Z\gamma}$ to the $Z\gamma$ kinetic mixing, and this correction does not involve the parity-odd part, while the parity-even part of this mixing is proportional to $q^\alpha q^\beta - q^2 g^{\alpha\beta}$. On the other hand, if remove this vacuum 1-loop bubble from the diagram and make thermal averaging of the remaining expression, the resulting parity-odd part will become first order in photon momentum q. (This situation repeats in Sec. 5.4.2, where it is described in more detail.) If one restores the removed piece, the resulting polarization tensor will be at least cubic in q, and hence it does not contribute to Π_2.

The third diagram in Fig. 5.2 can be thought of as diagram with self-energy insertion. However, contrary to the diagram with self-energy, which was considered before, the new diagram vanishes. The reason is that the tadpole contribution to self-energy is momentum-independent and therefore vanishes after renormalization.

5.4 $ff\gamma \to ff\gamma$ diagrams

In this Section, we consider the contribution to Π_2 from diagrams with two initial and two outgoing real fermions. Some of the diagrams from this class are drawn in Fig. 5.3. We conclude, that the total contribution from this class vanishes.

In analogy with Sec. 5.3, the contributions to polarization tensor from Fig. 5.3 can be expressed in terms of *tree-level* scattering amplitudes $\mathcal{M}^{ij}$. But, contrary to the previously considered case, now the *double* thermal averaging of the amplitude should be performed,[5]

$$\Pi^{ij} = +\int \frac{d^3r}{(2\pi)^3} n_F(\epsilon_r) \int \frac{d^3p}{(2\pi)^3} n_F(\epsilon_p) \sum_{s,s'} i\mathcal{M}^{ij}. \tag{5.11}$$

Here $\boldsymbol{r}, s$ are the common momentum and polarization of one pair of incoming and outgoing fermions, and $\boldsymbol{p}, s'$ are the common momentum and polarization of the remaining pair. Therefore, in order to find the partial contribution to the polarization tensor, one has to specify which initial fermions are paired with which outgoing fermions. For each given diagram, it is possible to do in two different ways. For the top-left diagram in Fig. 5.3, one of the choices leads to the factorization of the amplitude in two matrix elements with *independent* momenta

---

[5] Since we consider processes like $e^-e^-\gamma \to e^-e^-\gamma$, where identical fermions are present in the initial and final states, one has to be careful with the definition of amplitude $\mathcal{M}^{ij}$, since it may acquire additional sign, which may be not taken into account in naive application of Feynman rules.

$$\mathcal{M}_1^{ij} = +\frac{e^2}{M_Z^2}\ \left[\bar{u}(r)\gamma^i S(r+q)\gamma_\alpha \hat{g} u(r)\right]\left[\bar{u}(p)\gamma^\alpha \hat{g} S(p+q)\gamma^j u(p)\right], \qquad (5.12)$$

while the other choice does not seem to admit such a factorization[6]

$$\mathcal{M}_2^{ij} = -\frac{e^2}{M_Z^2}\ \left[\bar{u}(p)\gamma^i S(p+q)\gamma_\alpha \hat{g} u(r)\right]\ \left[\bar{u}(r)\gamma^\alpha \hat{g} S(p+q)\gamma^j u(p)\right], \qquad (5.13)$$

at the first sight. (Note that only the leading-order term in momentum was kept in the propagator of Z-boson.) However, it is possible to do a factorization for the latter amplitude as well. Indeed, since we are actually interested in the parity-violating part of the amplitude, the mixed terms, which are proportional to $g_L g_R$, and which come from the chiral coupling $\hat{g} = g_L P_L + g_R P_R$, will not contribute. This can be understood from the observation that if one performs the parity transformation, P_L changes into P_R and vice versa, so that the sum of the mixed terms remains unchanged. Only the terms, which involve g_L^2 or g_R^2, are relevant. For them one may apply the identity

$$(\gamma^\alpha P_L)_{\lambda\rho}(\gamma_\alpha P_L)_{\lambda'\rho'} = -(\gamma^\alpha P_L)_{\lambda\rho'}(\gamma_\alpha P_L)_{\lambda'\rho}, \qquad (5.14)$$

which is commonly used in derivation of the Fierz identities, and a similar identity, where one replaces the left chiral projectors P_L with the right chiral projectors P_R. As a result, the parity-odd part of the amplitude becomes factorized

$$\begin{aligned}\mathcal{M}_2^{ij} = &+\frac{g_L^2 e^2}{M_Z^2}\left[\bar{u}(r)\gamma^\alpha P_L u(r)\right]\ \left[\bar{u}(p)\gamma^i S(p+q)\gamma_\alpha P_L S(p+q)\gamma^j u(p)\right] + \\ &+ (g_L, P_L \to g_R, P_R) \quad \text{(Parity-odd part)}\end{aligned} \qquad (5.15)$$

Graphically, the application of Eq. (5.14) is equivalent to a repairing of the four fermion lines, which are attached to the Z-boson line. The same factorization is applicable to the other diagrams from Fig. 5.3. As a result, all these diagrams become splitted into two subclasses. In the first one, one of the two factors involves both electromagnetic vertices (that is, it involves both γ^i and γ^j), and this subclass is described in Sec. 5.4.1. In the second subclass, each of the factors involves only one electromagnetic vertex, and this subclass is described in Sec. 5.4.2.

It is worth noting that if we consider scattering with change of photon momentum, $q \neq q'$, the transversality property, $q_\mu \mathcal{M}_{\mu\nu}(q,q') = q'_\nu \mathcal{M}_{\mu\nu}(q,q') = 0$, holds for sum of the amplitudes of both subclasses. However, $\mathcal{M}_{\mu\nu}$ is not analytic in q, q', since at $q \to 0$, $q' \to 0$ all the intermediate fermion momenta become on-shell, therefore the denominators of the corresponding propagators become zero. As a result, the gauge invariance does not imply the absence of Π_2.

---

[6] In this amplitude, the additional sign "-" appears, which is related to the issue of identical fermions, mentioned above.

5.4.1 Self-energy diagrams

Some of the amplitudes from the first subclass of the $ee\gamma \to ee\gamma$ scattering are ill-defined. Indeed, if one considers the top-right diagram from Fig. 5.3, after the application of the Fierz-like identity (5.14), one receives the term

$$\mathcal{M}_3^{ij} = +\frac{e^2 g_L^2}{M_Z^2}[\bar{u}(r)\gamma^\alpha P_L u(r)][\bar{u}(p)\gamma_\alpha P_L S(p)\gamma^j S(p-q)\gamma^i u(p)] - (g_L, P_L \to g_R, P_R), \tag{5.16}$$

which involves the fermion propagator $S(p)$ at on-shell momentum, $p^2 = m^2$. It makes the whole amplitude singular, and requires more careful treatment, which is provided below.

Before we proceed, it is convenient to perform one out of the two thermal averagings of the amplitude in (5.11). Namely, we average over possible 3-momenta of the factor, which does not involve the electromagnetic vertices. As a result, this factor can be replaced by the expression

$$i\Sigma_{\text{med}} = b_\mu \gamma^\mu \gamma^5, \tag{5.17}$$

This expression is the medium contribution to the parity-piolating part of the self-energy of fermion. The spatial components of the vector b_μ vanish in the rest frame of plasma, while the temporal component, $b_0 \propto (g_L^2 - g_R^2)\Delta n_e / M_Z^2$, is finite and involves asymmetry in numbers of electrons and positrons, $\Delta n_e = \mu T^2/3$.

Note, that there is an infinite class of the diagrams, which also are ill-defined. In analogy with the discussion above, they all can be effectively reduced to diagrams with insertion of more self-energy corrections Σ_{med} in the fermionic lines (both internal and external). However, explicit resummation of these diagrams is possible, and is equivalent to the replacement of the "vacuum" Dirac propagators with $S_A(p) = i/(\not{p} - m - i\Sigma_{\text{med}})$, Dirac wavefunctions u, v by the eigenfunctions $\chi_\pm$ of the modified Hamiltonian, and the modification of the dispersion relation, which enters the remaining Fermi distribution in (5.11).The net result is described by

$$\Pi_2^{ij} = +\int \frac{d^3 r}{(2\pi)^3} \sum_s n_F(E_{rs} - \mu)\; i\mathcal{M}_{\text{eff}}^{ij} \tag{5.18}$$

where

$$\mathcal{M}_{\text{eff}}^{ij} = +ie^2\left[\bar{\chi}_+(r)\gamma^i S_A(r+q)\gamma^j \chi_+(r) + \bar{\chi}_+(r)\gamma^j S_A(r-q)\gamma^i \chi_+(r)\right] \tag{5.19}$$

is the effective amplitude of process $f\gamma \to f\gamma$. One has also to include in (5.18) the contribution of the charge-conjugated process, $\bar{f}\gamma \to \bar{f}\gamma$. Note the similarity of Eq. (5.18) with Eq. (5.5).

In order to compute (5.18), one can proceed with the straightforward quantum-mechanical approach, but it seems to be more convenient to make a connection with the imaginary-time (Matsubara) formalism. One can check that if one performs first the summation over the imaginary frequencies $i\omega_n = i\pi T(2n+1)$ (n is integer) in the expression

$$ie^2 \int \frac{d^3p}{(2\pi)^3} T \sum_{p^0 = i\omega_n + \mu} \mathrm{Tr}\,[\gamma^\mu S_A(p)\gamma^\nu S_A(p-q)], \tag{5.20}$$

and subtracts in the resulting integrand the term, which is the limit of this integrand at $T=0$, $\mu=0$, then the result coincides with (5.18). This expression was considered in Chap. 4, and we saw that it vanishes.

5.4.2 $Z\gamma$ mixing diagrams

In this Section, we consider partial contribution to the polarization tensor, which comes from the subclass of amplitudes that can be written as a product of two factors, where each of the factors involves *one* electromagnetic vertex. The conclusion is that this contribution gives vanishing Π_2.

One example of the amplitude under consideration was given in Eq. (5.12). Note that each of the two factors therein is proportional to the amplitude of $f\gamma \to fZ$ scattering. The thermal averaging in (5.11) gives a product of $\Pi^{\mu\alpha}(Z\gamma)\Pi^{\alpha\nu}(Z\gamma)$, where

$$\Pi^{\alpha\beta}(Z\gamma) = -e\int \frac{d^3r}{(2\pi)^3} \sum_s n_{\text{F}}(\epsilon_r - \mu)\bar{u}(r)\gamma^\alpha \hat{g} S(r+q)\gamma^\beta u(r) + (\text{cross terms}) \tag{5.21}$$

is the medium correction to the $Z\gamma$ mixing tensor, which comes from exchange of fermions (The sum is over possible electron helicities $s=\pm$). Application of the method of Sec. 5.4.1, which was based on connection with the imaginary-time technique, to calculation of this mixing tensor gives

$$\Pi^{\alpha\beta}(Z\gamma) \propto \mu\epsilon^{0\alpha\beta\gamma}q_\gamma \quad (\text{Parity-odd part}) \tag{5.22}$$

for the parity-odd part. The parity-even expression is basically the same as the thermal polarization tensor of *photon* in QED, only the prefactor e^2 in the QED expression must be replaced by eg. In the limit $q^0 \ll |\boldsymbol{q}|$ that we consider, the polarization tensor in QED is equal to $\Pi^{\alpha\beta}(QED) = e^2T^2\delta_0^\mu\delta_0^\nu/3 + \mathcal{O}(q_0^2/\boldsymbol{q}^2)$ (for a single fermion flavour that runs in the loop) [231]. Therefore, the expansion of $\Pi^{ij}(Z\gamma)$ in $\boldsymbol{q}$ starts from the linear term, and the contraction of two mixing tensors $\Pi(Z\gamma)$ does not comprise any $\mathcal{O}(q)$ terms, so that $\Pi_2 = 0$ for the considered subclass of diagrams.

5.5 Discussion

In this Chapter, we have studied the question whether Chiral Magnetic Effect can result from particle interactions, for plasma that is initially in the state of thermal equilibrium. We have analyzed a particular model with two gauge fields, where one of the fields is massless and plays a role of electromagnetic field, while the other is massive and mediates the parity-violating interaction of fermions. Our results demonstrate that the Chiral Magnetic Effect is *absent* in such a system. This situation is non-trivial, and becomes possible due to cancellation of several types of contributions to the Chiral Magnetic Current. The key ingridients here are gauge invariance and analyticity of scattering amplitudes.

This model with two gauge fields should be contrasted with the model with *local* Fermi interaction of four fermions, where no massive gauge field is present, and where the value of the Chiral Magnetic Current is ambiguous due to ultraviolet divergences as it was discussed in Chap. 4. On the other hand, the model with two gauge fields is renormalizable, therefore all the ultraviolet divergences can be unambiguously removed, and the physical observables like currents become well-defined.

Finally, we want to relate the analysis of this Chapter to the realistic case of the Standard Model, where instead of two gauge fields one deals with *four* fields (the electromagnetic field plus fields of the massive gauge bosons Z, $W^{\pm}$), and where the fermion flavours are not conserved in particle reactions, in general. Although in the case of the Standard Model, there are more different classes of contributions to the Chiral Magnetic Current, preliminary inspection shows that they cancel each other in the sum, similarly to how the cancellation happens in the $U(1) \times U(1)$ model. Therefore, we expect that the Chiral Magnetic Effect is absent in thermal equilibrium, and may appear only for out-of-equilibrium states.

Bibliography

[1] S. Weinberg, *A Model of Leptons*, *Phys. Rev. Lett.* **19** (1967) 1264–1266.

[2] S. L. Glashow, *Partial Symmetries of Weak Interactions*, *Nucl. Phys.* **22** (1961) 579–588.

[3] A. Salam, *Weak and Electromagnetic Interactions*, *Conf. Proc.* **C680519** (1968) 367–377.

[4] H. D. Politzer, *Reliable Perturbative Results for Strong Interactions?*, *Phys. Rev. Lett.* **30** (1973) 1346–1349.

[5] D. J. Gross and F. Wilczek, *Ultraviolet Behavior of Nonabelian Gauge Theories*, *Phys. Rev. Lett.* **30** (1973) 1343–1346.

[6] B. T. Cleveland, T. Daily, R. Davis, Jr., J. R. Distel, K. Lande, C. K. Lee, P. S. Wildenhain, and J. Ullman, *Measurement of the solar electron neutrino flux with the Homestake chlorine detector*, *Astrophys. J.* **496** (1998) 505–526.

[7] **Super-Kamiokande** Collaboration, Y. Fukuda et al., *Evidence for oscillation of atmospheric neutrinos*, *Phys. Rev. Lett.* **81** (1998) 1562–1567, [`hep-ex/9807003`].

[8] **KamLAND** Collaboration, K. Eguchi et al., *First results from KamLAND: Evidence for reactor anti-neutrino disappearance*, *Phys. Rev. Lett.* **90** (2003) 021802, [`hep-ex/0212021`].

[9] **RENO collaboration** Collaboration, J. Ahn et al., *Observation of Reactor Electron Antineutrino Disappearance in the RENO Experiment*, `arXiv:1204.0626`.

[10] **DAYA-BAY Collaboration** Collaboration, F. An et al., *Observation of electron-antineutrino disappearance at Daya Bay*, `arXiv:1203.1669`.

[11] **MINOS** Collaboration, D. G. Michael et al., *Observation of muon neutrino disappearance with the MINOS detectors and the NuMI neutrino beam*, *Phys. Rev. Lett.* **97** (2006) 191801, [`hep-ex/0607088`].

[12] **T2K** Collaboration, K. Abe et al., *Indication of Electron Neutrino Appearance from an Accelerator-produced Off-axis Muon Neutrino Beam*, *Phys.Rev.Lett.* **107** (2011) 041801, [arXiv:1106.2822].

[13] **MINOS** Collaboration, P. Adamson et al., *Improved search for muon-neutrino to electron-neutrino oscillations in MINOS*, *Phys.Rev.Lett.* **107** (2011) 181802, [arXiv:1108.0015].

[14] M. C. Gonzalez-Garcia, M. Maltoni, and T. Schwetz, *Updated fit to three neutrino mixing: status of leptonic CP violation*, *JHEP* **11** (2014) 052, [arXiv:1409.5439].

[15] **Particle Data Group** Collaboration, K. A. Olive et al., *Review of Particle Physics*, *Chin. Phys.* **C38** (2014) 090001.

[16] Z. Maki, M. Nakagawa, and S. Sakata, *Remarks on the unified model of elementary particles*, *Prog. Theor. Phys.* **28** (1962) 870–880.

[17] B. Pontecorvo, *Mesonium and anti-mesonium*, *Sov. Phys. JETP* **6** (1957) 429. [Zh. Eksp. Teor. Fiz.33,549(1957)].

[18] B. Pontecorvo, *Neutrino Experiments and the Problem of Conservation of Leptonic Charge*, *Sov. Phys. JETP* **26** (1968) 984–988. [Zh. Eksp. Teor. Fiz.53,1717(1967)].

[19] S. Weinberg, *Baryon and Lepton Nonconserving Processes*, *Phys. Rev. Lett.* **43** (1979) 1566–1570.

[20] **Planck** Collaboration, P. A. R. Ade et al., *Planck 2015 results. XIII. Cosmological parameters*, arXiv:1502.01589.

[21] **Troitsk** Collaboration, V. N. Aseev et al., *An upper limit on electron antineutrino mass from Troitsk experiment*, *Phys. Rev.* **D84** (2011) 112003, [arXiv:1108.5034].

[22] M. G. Walker, *Dark Matter in the Milky Way's Dwarf Spheroidal Satellites*, arXiv:1205.0311.

[23] M. Roos, *Astrophysical and cosmological probes of dark matter*, *J. Mod. Phys.* **3** (2012) 1152, [arXiv:1208.3662].

[24] R. Massey, T. Kitching, and J. Richard, *The dark matter of gravitational lensing*, *Rept. Prog. Phys.* **73** (2010) 086901, [arXiv:1001.1739].

[25] **DSDD** Collaboration, E. Rozo et al., *Cosmological Constraints from the SDSS maxBCG Cluster Catalog*, *Astrophys. J.* **708** (2010) 645–660, [arXiv:0902.3702].

[26] B. A. Reid et al., *Cosmological Constraints from the Clustering of the Sloan Digital Sky Survey DR7 Luminous Red Galaxies*, *Mon. Not. Roy. Astron. Soc.* **404** (2010) 60–85, [`arXiv:0907.1659`].

[27] C. S. Frenk and S. D. M. White, *Dark matter and cosmic structure*, *Annalen Phys.* **524** (2012) 507–534, [`arXiv:1210.0544`].

[28] G. Bertone, D. Hooper, and J. Silk, *Particle dark matter: Evidence, candidates and constraints*, *Phys. Rept.* **405** (2005) 279–390, [`hep-ph/0404175`].

[29] M. Drees and G. Gerbier, *Mini-Review of Dark Matter: 2012*, `arXiv:1204.2373`.

[30] S. Tremaine and J. E. Gunn, *Dynamical Role of Light Neutral Leptons in Cosmology*, *Phys. Rev. Lett.* **42** (1979) 407–410.

[31] A. Boyarsky, O. Ruchayskiy, and D. Iakubovskyi, *A Lower bound on the mass of Dark Matter particles*, *JCAP* **0903** (2009) 005, [`arXiv:0808.3902`].

[32] M. Davis, G. Efstathiou, C. S. Frenk, and S. D. M. White, *The Evolution of Large Scale Structure in a Universe Dominated by Cold Dark Matter*, *Astrophys. J.* **292** (1985) 371–394.

[33] J. Lesgourgues and S. Pastor, *Massive neutrinos and cosmology*, *Phys. Rept.* **429** (2006) 307–379, [`astro-ph/0603494`].

[34] **Planck** Collaboration, P. A. R. Ade et al., *Planck 2013 results. XVI. Cosmological parameters*, *Astron. Astrophys.* **571** (2014) A16, [`arXiv:1303.5076`].

[35] A. H. Guth, *The Inflationary Universe: A Possible Solution to the Horizon and Flatness Problems*, *Phys. Rev.* **D23** (1981) 347–356.

[36] A. D. Linde, *A New Inflationary Universe Scenario: A Possible Solution of the Horizon, Flatness, Homogeneity, Isotropy and Primordial Monopole Problems*, *Phys. Lett.* **B108** (1982) 389–393.

[37] A. A. Starobinsky, *A New Type of Isotropic Cosmological Models Without Singularity*, *Phys. Lett.* **B91** (1980) 99–102.

[38] **Planck** Collaboration, P. A. R. Ade et al., *Planck 2015 results. XX. Constraints on inflation*, `arXiv:1502.02114`.

[39] R. H. Brandenberger, *Inflationary cosmology: Progress and problems*, in *IPM School on Cosmology 1999: Large Scale Structure Formation Tehran, Iran, January 23-February 4, 1999*, 1999. `hep-ph/9910410`.

[40] K. Kajantie, M. Laine, K. Rummukainen, and M. E. Shaposhnikov, *Is there a hot electroweak phase transition at m(H) larger or equal to m(W)?*, *Phys. Rev. Lett.* **77** (1996) 2887–2890, [hep-ph/9605288].

[41] K. Rummukainen, M. Tsypin, K. Kajantie, M. Laine, and M. E. Shaposhnikov, *The Universality class of the electroweak theory*, *Nucl. Phys.* **B532** (1998) 283–314, [hep-lat/9805013].

[42] F. Csikor, Z. Fodor, and J. Heitger, *Endpoint of the hot electroweak phase transition*, *Phys. Rev. Lett.* **82** (1999) 21–24, [hep-ph/9809291].

[43] **OPAL, DELPHI, LEP Working Group for Higgs boson searches, ALEPH, L3** Collaboration, R. Barate et al., *Search for the standard model Higgs boson at LEP*, *Phys. Lett.* **B565** (2003) 61–75, [hep-ex/0306033].

[44] **ATLAS** Collaboration, G. Aad et al., *Observation of a new particle in the search for the Standard Model Higgs boson with the ATLAS detector at the LHC*, *Phys. Lett.* **B716** (2012) 1–29, [arXiv:1207.7214].

[45] **CMS** Collaboration, S. Chatrchyan et al., *Observation of a new boson at a mass of 125 GeV with the CMS experiment at the LHC*, *Phys. Lett.* **B716** (2012) 30–61, [arXiv:1207.7235].

[46] P. Minkowski, *mu → e gamma at a rate of one out of 1-billion muon decays?*, *Phys. Lett.* **B67** (1977) 421.

[47] P. Ramond, *The Family Group in Grand Unified Theories*, .

[48] R. N. Mohapatra and G. Senjanovic, *Neutrino mass and spontaneous parity nonconservation*, *Phys. Rev. Lett.* **44** (1980) 912.

[49] T. Yanagida, *Horizontal gauge symmetry and masses of neutrinos*, *Prog. Theor. Phys.* **64** (1980) 1103.

[50] T. Asaka, S. Blanchet, and M. Shaposhnikov, *The nuMSM, dark matter and neutrino masses*, *Phys. Lett.* **B631** (2005) 151–156, [hep-ph/0503065].

[51] D. Notzold and G. Raffelt, *Neutrino Dispersion at Finite Temperature and Density*, *Nucl.Phys.* **B307** (1988) 924.

[52] F. Iocco, G. Mangano, G. Miele, O. Pisanti, and P. D. Serpico, *Primordial Nucleosynthesis: from precision cosmology to fundamental physics*, *Phys. Rept.* **472** (2009) 1–76, [arXiv:0809.0631].

[53] G. Steigman, *Primordial Nucleosynthesis in the Precision Cosmology Era*, *Ann.Rev.Nucl.Part.Sci.* **57** (2007) 463–491.

[54] M. Pospelov and J. Pradler, *Big Bang Nucleosynthesis as a Probe of New Physics*, *Ann.Rev.Nucl.Part.Sci.* **60** (2010) 539–568.

[55] S. Dodelson and L. M. Widrow, *Sterile-neutrinos as dark matter*, *Phys. Rev. Lett.* **72** (1994) 17–20, [hep-ph/9303287].

[56] X.-D. Shi and G. M. Fuller, *A New dark matter candidate: Nonthermal sterile neutrinos*, *Phys. Rev. Lett.* **82** (1999) 2832–2835, [astro-ph/9810076].

[57] A. D. Dolgov and S. H. Hansen, *Massive sterile neutrinos as warm dark matter*, *Astropart. Phys.* **16** (2002) 339–344, [hep-ph/0009083].

[58] M. Laine and M. Shaposhnikov, *Sterile neutrino dark matter as a consequence of nuMSM-induced lepton asymmetry*, *JCAP* **0806** (2008) 031, [arXiv:0804.4543].

[59] K. N. Abazajian, *Resonantly Produced 7 keV Sterile Neutrino Dark Matter Models and the Properties of Milky Way Satellites*, *Phys. Rev. Lett.* **112** (2014), no. 16 161303, [arXiv:1403.0954].

[60] J. Ghiglieri and M. Laine, *Improved determination of sterile neutrino dark matter spectrum*, arXiv:1506.06752.

[61] T. Venumadhav, F.-Y. Cyr-Racine, K. N. Abazajian, and C. M. Hirata, *Sterile neutrino dark matter: A tale of weak interactions in the strong coupling epoch*, arXiv:1507.06655.

[62] A. Boyarsky, O. Ruchayskiy, and M. Shaposhnikov, *The Role of sterile neutrinos in cosmology and astrophysics*, *Ann. Rev. Nucl. Part. Sci.* **59** (2009) 191–214, [arXiv:0901.0011].

[63] A. Boyarsky, A. Neronov, O. Ruchayskiy, and M. Shaposhnikov, *The Masses of active neutrinos in the nuMSM from X-ray astronomy*, *JETP Lett.* **83** (2006) 133–135, [hep-ph/0601098].

[64] P. B. Pal and L. Wolfenstein, *Radiative Decays of Massive Neutrinos*, *Phys. Rev.* **D25** (1982) 766.

[65] K. Abazajian, G. M. Fuller, and W. H. Tucker, *Direct detection of warm dark matter in the X-ray*, *Astrophys. J.* **562** (2001) 593–604, [astro-ph/0106002].

[66] J. W. den Herder et al., *The Search for decaying Dark Matter*, arXiv:0906.1788.

[67] E. Bulbul, M. Markevitch, A. Foster, R. K. Smith, M. Loewenstein, and S. W. Randall, *Detection of An Unidentified Emission Line in the Stacked X-ray spectrum of Galaxy Clusters*, *Astrophys. J.* **789** (2014) 13, [arXiv:1402.2301].

[68] A. Boyarsky, O. Ruchayskiy, D. Iakubovskyi, and J. Franse, *Unidentified Line in X-Ray Spectra of the Andromeda Galaxy and Perseus Galaxy Cluster*, *Phys. Rev. Lett.* **113** (2014) 251301, [`arXiv:1402.4119`].

[69] A. Boyarsky, J. Lesgourgues, O. Ruchayskiy, and M. Viel, *Lyman-alpha constraints on warm and on warm-plus-cold dark matter models*, *JCAP* **0905** (2009) 012, [`arXiv:0812.0010`].

[70] U. Seljak, A. Makarov, P. McDonald, and H. Trac, *Can sterile neutrinos be the dark matter?*, *Phys. Rev. Lett.* **97** (2006) 191303, [`astro-ph/0602430`].

[71] M. Viel, J. Lesgourgues, M. G. Haehnelt, S. Matarrese, and A. Riotto, *Can sterile neutrinos be ruled out as warm dark matter candidates?*, *Phys. Rev. Lett.* **97** (2006) 071301, [`astro-ph/0605706`].

[72] A. Boyarsky, J. Lesgourgues, O. Ruchayskiy, and M. Viel, *Realistic sterile neutrino dark matter with keV mass does not contradict cosmological bounds*, *Phys. Rev. Lett.* **102** (2009) 201304, [`arXiv:0812.3256`].

[73] P. D. Serpico and G. G. Raffelt, *Lepton asymmetry and primordial nucleosynthesis in the era of precision cosmology*, *Phys. Rev.* **D71** (2005) 127301, [`astro-ph/0506162`].

[74] G. Mangano, G. Miele, S. Pastor, O. Pisanti, and S. Sarikas, *Updated BBN bounds on the cosmological lepton asymmetry for non-zero* θ_{13}, *Phys. Lett.* **B708** (2012) 1–5, [`arXiv:1110.4335`].

[75] A. D. Sakharov, *Violation of CP Invariance, c Asymmetry, and Baryon Asymmetry of the Universe*, *Pisma Zh. Eksp. Teor. Fiz.* **5** (1967) 32–35. [Usp. Fiz. Nauk161,61(1991)].

[76] V. A. Kuzmin, V. A. Rubakov, and M. E. Shaposhnikov, *On the Anomalous Electroweak Baryon Number Nonconservation in the Early Universe*, *Phys. Lett.* **B155** (1985) 36.

[77] S. L. Adler, *Axial vector vertex in spinor electrodynamics*, *Phys. Rev.* **177** (1969) 2426–2438.

[78] J. S. Bell and R. Jackiw, *A PCAC puzzle: pi0 –> gamma gamma in the sigma model*, *Nuovo Cim.* **A60** (1969) 47–61.

[79] F. R. Klinkhamer and N. S. Manton, *A Saddle Point Solution in the Weinberg-Salam Theory*, *Phys. Rev.* **D30** (1984) 2212.

[80] S. Davidson, E. Nardi, and Y. Nir, *Leptogenesis*, *Phys. Rept.* **466** (2008) 105–177, [`arXiv:0802.2962`].

[81] E. K. Akhmedov, V. A. Rubakov, and A. Yu. Smirnov, *Baryogenesis via neutrino oscillations*, *Phys. Rev. Lett.* **81** (1998) 1359–1362, [hep-ph/9803255].

[82] T. Asaka and M. Shaposhnikov, *The nuMSM, dark matter and baryon asymmetry of the universe*, *Phys. Lett.* **B620** (2005) 17–26, [hep-ph/0505013].

[83] T. Asaka and S. Eijima, *Direct Search for Right-handed Neutrinos and Neutrinoless Double Beta Decay*, *PTEP* **2013** (2013), no. 11 113B02, [arXiv:1308.3550].

[84] L. Canetti, M. Drewes, and M. Shaposhnikov, *Sterile Neutrinos as the Origin of Dark and Baryonic Matter*, *Phys. Rev. Lett.* **110** (2013), no. 6 061801, [arXiv:1204.3902].

[85] L. Canetti, M. Drewes, T. Frossard, and M. Shaposhnikov, *Dark Matter, Baryogenesis and Neutrino Oscillations from Right Handed Neutrinos*, *Phys. Rev.* **D87** (2013), no. 9 093006, [arXiv:1208.4607].

[86] L. Canetti, M. Drewes, and B. Garbrecht, *Probing leptogenesis with GeV-scale sterile neutrinos at LHCb and Belle II*, *Phys. Rev.* **D90** (2014), no. 12 125005, [arXiv:1404.7114].

[87] F. L. Bezrukov and M. Shaposhnikov, *The Standard Model Higgs boson as the inflaton*, *Phys. Lett.* **B659** (2008) 703–706, [arXiv:0710.3755].

[88] F. Bezrukov, J. Rubio, and M. Shaposhnikov, *Living beyond the edge: Higgs inflation and vacuum metastability*, arXiv:1412.3811.

[89] A. Roy and M. Shaposhnikov, *Resonant production of the sterile neutrino dark matter and fine-tunings in the [nu]MSM*, *Phys. Rev.* **D82** (2010) 056014, [arXiv:1006.4008].

[90] A. Vilenkin, *EQUILIBRIUM PARITY VIOLATING CURRENT IN A MAGNETIC FIELD*, *Phys. Rev.* **D22** (1980) 3080–3084.

[91] V. A. Rubakov, *On the Electroweak Theory at High Fermion Density*, *Prog. Theor. Phys.* **75** (1986) 366.

[92] M. Joyce and M. E. Shaposhnikov, *Primordial magnetic fields, right-handed electrons, and the Abelian anomaly*, *Phys. Rev. Lett.* **79** (1997) 1193–1196, [astro-ph/9703005].

[93] J. Frohlich and B. Pedrini, *New applications of the chiral anomaly*, hep-th/0002195.

[94] J. Frohlich and B. Pedrini, *Axions, quantum mechanical pumping, and primeval magnetic fields*, cond-mat/0201236.

[95] B. A. Campbell, S. Davidson, J. R. Ellis, and K. A. Olive, *On the baryon, lepton flavor and right-handed electron asymmetries of the universe*, *Phys. Lett.* **B297** (1992) 118–124, [hep-ph/9302221].

[96] A. Boyarsky, J. Frohlich, and O. Ruchayskiy, *Self-consistent evolution of magnetic fields and chiral asymmetry in the early Universe*, *Phys.Rev.Lett.* **108** (2012) 031301, [arXiv:1109.3350].

[97] A. Boyarsky, J. Frohlich, and O. Ruchayskiy, *Magnetohydrodynamics of Chiral Relativistic Fluids*, arXiv:1504.04854.

[98] A. Boyarsky, O. Ruchayskiy, and M. Shaposhnikov, *Long-range magnetic fields in the ground state of the Standard Model plasma*, *Phys.Rev.Lett.* **109** (2012) 111602, [arXiv:1204.3604].

[99] D. Gorbunov and M. Shaposhnikov, *How to find neutral leptons of the νMSM?*, *JHEP* **10** (2007) 015, [arXiv:0705.1729]. [Erratum: JHEP11,101(2013)].

[100] W. Bonivento et al., *Proposal to Search for Heavy Neutral Leptons at the SPS*, arXiv:1310.1762.

[101] S. Alekhin et al., *A facility to Search for Hidden Particles at the CERN SPS: the SHiP physics case*, arXiv:1504.04855.

[102] **SHiP** Collaboration, M. Anelli et al., *A facility to Search for Hidden Particles (SHiP) at the CERN SPS*, arXiv:1504.04956.

[103] **FCC-ee study Team** Collaboration, A. Blondel, E. Graverini, N. Serra, and M. Shaposhnikov, *Search for Heavy Right Handed Neutrinos at the FCC-ee*, arXiv:1411.5230.

[104] A. Strumia and F. Vissani, *Neutrino masses and mixings and...*, .

[105] K. Nakamura et al., *Review of particle physics*, *J.Phys.* **G37** (2010) 075021.

[106] E. Komatsu et al., *Seven-Year Wilkinson Microwave Anisotropy Probe (WMAP) Observations: Cosmological Interpretation*, *Astrophys.J.Suppl.* **192** (Feb., 2011) 18.

[107] A. Atre, T. Han, S. Pascoli, and B. Zhang, *The Search for Heavy Majorana Neutrinos*, *JHEP* **0905** (2009) 030.

[108] D. Gorbunov and M. Shaposhnikov, *How to find neutral leptons of the numsm?*, *JHEP* **10** (2007) 015.

[109] M. Shaposhnikov, *The nuMSM, leptonic asymmetries, and properties of singlet fermions*, *JHEP* **0808** (2008) 008.

[110] T. Schwetz, M. Tortola, and J. W. Valle, *Three-flavour neutrino oscillation update*, *New J.Phys.* **10** (2008) 113011.

[111] G. L. Fogli, E. Lisi, A. Marrone, A. Palazzo, and A. M. Rotunno, *Evidence of theta(13)>0 from global neutrino data analysis*, *Phys.Rev.* **D84** (2011) 053007, [arXiv:1106.6028].

[112] T. Asaka, S. Eijima, and H. Ishida, *Mixing of Active and Sterile Neutrinos*, *JHEP* **1104** (2011) 011, [arXiv:1101.1382].

[113] V. Gorkavenko and S. Vilchynskiy, *Some constraints on the Yukawa parameters in the neutrino modification of the Standard Model (nuMSM) and CP-violation*, *Eur.Phys.J.* **C70** (2010) 1091–1098, [arXiv:0907.4484].

[114] World Scientific, *International Conference on the Seesaw Mechanism*, (Singapore), World Scientific, 2005.

[115] J. Schechter and J. Valle, *Neutrino Masses in SU(2) x U(1) Theories*, *Phys.Rev.* **D22** (1980) 2227.

[116] J. Schechter and J. Valle, *Neutrino Decay and Spontaneous Violation of Lepton Number*, *Phys.Rev.* **D25** (1982) 774.

[117] W. Rodejohann and J. Valle, *Symmetrical Parametrizations of the Lepton Mixing Matrix*, *Phys.Rev.* **D84** (2011) 073011, [arXiv:1108.3484].

[118] T. Asaka, S. Blanchet, and M. Shaposhnikov, *The nuMSM, dark matter and neutrino masses*, *Phys.Lett.* **B631** (2005) 151–156.

[119] T. Asaka and M. Shaposhnikov, *The nuMSM, dark matter and baryon asymmetry of the universe*, *Phys.Lett.* **B620** (July, 2005) 17–26.

[120] A. Boyarsky, O. Ruchayskiy, and M. Shaposhnikov, *The Role of sterile neutrinos in cosmology and astrophysics*, *Ann.Rev.Nucl.Part.Sci.* **59** (2009) 191–214.

[121] A. Boyarsky, A. Neronov, O. Ruchayskiy, and M. Shaposhnikov, *The Masses of active neutrinos in the nuMSM from X-ray astronomy*, *JETP Lett.* **83** (2006) 133–135.

[122] M. Shaposhnikov, *A Possible symmetry of the nuMSM*, *Nucl.Phys.* **B763** (2007) 49–59.

[123] T. Schwetz, M. Tortola, and J. Valle, *Where we are on θ_{13}: addendum to 'Global neutrino data and recent reactor fluxes: status of three-flavour oscillation parameters'*, *New J.Phys.* **13** (2011) 109401, [arXiv:1108.1376].

[124] J. Casas and A. Ibarra, *Oscillating neutrinos and muon —&gt; e, gamma*, *Nucl.Phys.* **B618** (2001) 171–204.

[125] G. Bernardi, G. Carugno, J. Chauveau, F. Dicarlo, M. Dris, et al., *Search for Neutrino Decay*, *Phys.Lett.* **B166** (1986) 479.

[126] G. Bernardi et al., *Further limits on heavy neutrino couplings*, *Phys. Lett.* **B203** (1988) 332.

[127] D. Britton, S. Ahmad, D. Bryman, R. Burnbam, E. Clifford, et al., *Measurement of the* $\pi^+ \to e^+\nu$ *branching ratio*, *Phys.Rev.Lett.* **68** (1992) 3000–3003.

[128] D. Britton, S. Ahmad, D. Bryman, R. Burnham, E. Clifford, et al., *Improved search for massive neutrinos in* $\pi^+ \to e^+\nu$ *decay*, *Phys.Rev.* **D46** (1992) 885–887.

[129] A. Vaitaitis et al., *Search for neutral heavy leptons in a high-energy neutrino beam*, *Phys.Rev.Lett.* **83** (1999) 4943–4946.

[130] **CHARM** Collaboration, F. Bergsma et al., *A SEARCH FOR DECAYS OF HEAVY NEUTRINOS IN THE MASS RANGE 0.5-GeV TO 2.8-GeV*, *Phys.Lett.* **B166** (1986) 473.

[131] T. Yamazaki et al., *Search for heavy neutrinos in kaon decay*, . IN *LEIPZIG 1984, PROCEEDINGS, HIGH ENERGY PHYSICS, VOL. 1*, 262.

[132] R. Hayano, T. Taniguchi, T. Yamanaka, T. Tanimori, R. Enomoto, et al., *HEAVY NEUTRINO SEARCH USING K(mu2) DECAY*, *Phys.Rev.Lett.* **49** (1982) 1305.

[133] D. Bryman and T. Numao, *Search for massive neutrinos in* $\pi+ \to \mu + \nu$ *decay*, *Phys.Rev.* **D53** (1996) 558–559.

[134] R. Abela, M. Daum, G. Eaton, R. Frosch, B. Jost, et al., *SEARCH FOR AN ADMIXTURE OF HEAVY NEUTRINO IN PION DECAY*, *Phys.Lett.* **B105** (1981) 263–266.

[135] M. Daum, B. Jost, R. Marshall, R. Minehart, W. Stephens, et al., *SEARCH FOR ADMIXTURES OF MASSIVE NEUTRINOS IN THE DECAY pi+ —> mu+ neutrino*, *Phys.Rev.* **D36** (1987) 2624.

[136] **PIENU Collaboration** Collaboration, M. Aoki et al., *Search for Massive Neutrinos in the Decay* $\pi \to e\nu$, *Phys.Rev.* **D84** (2011) 052002, [`arXiv:1106.4055`].

[137] **DELPHI** Collaboration, P. Abreu et al., *Search for neutral heavy leptons produced in Z decays*, *Z.Phys.* **C74** (1997) 57–71.

[138] M. Blennow, E. Fernandez-Martinez, J. Lopez-Pavon, and J. Menendez, *Neutrinoless double beta decay in seesaw models*, *JHEP* **1007** (2010) 096, [arXiv:1005.3240].

[139] F. Bezrukov, *nu MSM-predictions for neutrinoless double beta decay*, *Phys.Rev.* **D72** (2005) 071303.

[140] R. E. Shrock, *New Tests For, and Bounds On, Neutrino Masses and Lepton Mixing*, *Phys. Lett.* **B96** (1980) 159.

[141] R. E. Shrock, *General Theory of Weak Leptonic and Semileptonic Decays. 1. Leptonic Pseudoscalar Meson Decays, with Associated Tests For, and Bounds on, Neutrino Masses and Lepton Mixing*, *Phys.Rev.* **D24** (1981) 1232.

[142] R. E. Shrock, *General Theory of Weak Processes Involving Neutrinos. 2. Pure Leptonic Decays*, *Phys.Rev.* **D24** (1981) 1275.

[143] R. E. Shrock, *PURE LEPTONIC DECAYS WITH MASSIVE NEUTRINOS AND ARBITRARY LORENTZ STRUCTURE*, *Phys.Lett.* **B112** (1982) 382.

[144] A. Kusenko, S. Pascoli, and D. Semikoz, *New bounds on MeV sterile neutrinos based on the accelerator and Super-Kamiokande results*, *JHEP* **0511** (2005) 028.

[145] P. Astier et al., *Search for heavy neutrinos mixing with tau neutrinos*, *Phys.Lett.* **B506** (2001) 27–38.

[146] J.-M. Levy, *Doctoral thesis, university of paris (1986)*, .

[147] L. Canetti and M. Shaposhnikov, *Baryon Asymmetry of the Universe in the NuMSM*, *JCAP* **1009** (2010) 001.

[148] **LBNE Collaboration** Collaboration, T. Akiri et al., *The 2010 Interim Report of the Long-Baseline Neutrino Experiment Collaboration Physics Working Groups*, arXiv:1110.6249.

[149] K. Abazajian, M. Acero, S. Agarwalla, A. Aguilar-Arevalo, C. Albright, et al., *Light Sterile Neutrinos: A White Paper*, arXiv:1204.5379.

[150] A. Shaykhiev, Y. Kudenko, and A. Khotyantsev, *Searches for heavy neutrinos in the decays of positively charged kaons*, *Phys.Atom.Nucl.* **74** (2011) 788–793.

[151] A. Kusenko, *Sterile neutrinos, dark matter, and the pulsar velocities in models with a Higgs singlet*, *Phys.Rev.Lett.* **97** (2006) 241301.

[152] I. M. Shoemaker, K. Petraki, and A. Kusenko, *Collider signatures of sterile neutrinos in models with a gauge-singlet Higgs*, *JHEP* **1009** (2010) 060, [`arXiv:1006.5458`].

[153] E. K. Akhmedov, V. Rubakov, and A. Y. Smirnov, *Baryogenesis via neutrino oscillations*, *Phys.Rev.Lett.* **81** (1998) 1359–1362.

[154] R. Alpher, H. Bethe, and G. Gamow, *The origin of chemical elements*, *Phys.Rev.* **73** (1948) 803–804.

[155] F. Iocco, G. Mangano, G. Miele, O. Pisanti, and P. D. Serpico, *Primordial Nucleosynthesis: from precision cosmology to fundamental physics*, *Phys.Rept.* **472** (2009) 1–76.

[156] A. Dolgov, S. Hansen, G. Raffelt, and D. Semikoz, *Cosmological and astrophysical bounds on a heavy sterile neutrino and the KARMEN anomaly*, *Nucl.Phys.* **B580** (2000) 331–351.

[157] A. Dolgov, S. Hansen, G. Raffelt, and D. Semikoz, *Heavy sterile neutrinos: Bounds from big bang nucleosynthesis and SN1987A*, *Nucl.Phys.* **B590** (2000) 562–574.

[158] C. J. Smith, G. M. Fuller, and M. S. Smith, *Big Bang Nucleosynthesis with Independent Neutrino Distribution Functions*, *Phys.Rev.* **D79** (2009) 105001, [`arXiv:0812.1253`].

[159] A. Dolgov, S. Hansen, and D. Semikoz, *Impact of massive tau neutrinos on primordial nucleosynthesis. Exact calculations*, *Nucl.Phys.* **B524** (1998) 621–638, [`hep-ph/9712284`].

[160] A. Dolgov and D. Kirilova, *Nonequilibrium decays of light particles and the primordial nucleosynthesis*, *Int.J.Mod.Phys.* **A3** (1988) 267.

[161] M. Kawasaki, P. Kernan, H.-S. Kang, R. J. Scherrer, G. Steigman, et al., *Big bang nucleosynthesis constraints on the tau-neutrino mass*, *Nucl.Phys.* **B419** (1994) 105–128.

[162] M. Kawasaki, K. Kohri, and N. Sugiyama, *MeV scale reheating temperature and thermalization of neutrino background*, *Phys.Rev.* **D62** (2000) 023506, [`astro-ph/0002127`].

[163] S. Hannestad, *What is the lowest possible reheating temperature?*, *Phys.Rev.* **D70** (2004) 043506.

[164] A. D. Dolgov, S. H. Hansen, and D. V. Semikoz, *Nonequilibrium corrections to the spectra of massless neutrinos in the early universe: Addendum*, *Nucl. Phys.* **B543** (1999) 269–274.

[165] A. Dolgov, S. Hansen, and D. Semikoz, *Nonequilibrium corrections to the spectra of massless neutrinos in the early universe*, *Nucl.Phys.* **B503** (1997) 426–444.

[166] Y. Izotov and T. Thuan, *The primordial abundance of 4He: evidence for non-standard big bang nucleosynthesis*, *Astrophys.J.* **710** (2010) L67–L71, [arXiv:1001.4440].

[167] **Particle Data Group** Collaboration, K. Nakamura et al., *Review of particle physics*, *J.Phys.G* **G37** (2010) 075021.

[168] A. Serebrov and A. Fomin, *Neutron lifetime from a new evaluation of ultracold neutron storage experiments*, *Phys.Rev.* **C82** (2010) 035501, [arXiv:1005.4312].

[169] J. Lesgourgues and S. Pastor, *Cosmological implications of a relic neutrino asymmetry*, *Phys.Rev.* **D60** (Nov., 1999) 103521.

[170] P. D. Serpico and G. G. Raffelt, *Lepton asymmetry and primordial nucleosynthesis in the era of precision cosmology*, *Phys.Rev.* **D71** (2005) 127301.

[171] C. J. Smith, G. M. Fuller, C. T. Kishimoto, and K. N. Abazajian, *Light Element Signatures of Sterile Neutrinos and Cosmological Lepton Numbers*, *Phys.Rev.* **D74** (2006) 085008, [astro-ph/0608377].

[172] G. Mangano, G. Miele, S. Pastor, O. Pisanti, and S. Sarikas, *Constraining the cosmic radiation density due to lepton number with Big Bang Nucleosynthesis*, *JCAP* **1103** (2011) 035.

[173] E. Kolb and M. Turner, *The Early Universe*. Addison-Wesley, Reading, MA, USA, 1990. Prepared with LaTeX.

[174] A. Dolgov, S. Hansen, S. Pastor, S. Petcov, G. Raffelt, et al., *Cosmological bounds on neutrino degeneracy improved by flavor oscillations*, *Nucl.Phys.* **B632** (2002) 363–382, [hep-ph/0201287].

[175] A. Dolgov and F. Villante, *BBN bounds on active sterile neutrino mixing*, *Nucl.Phys.* **B679** (2004) 261–298, [hep-ph/0308083].

[176] D. Kirilova, *Non-equilibrium neutrino in the early universe plasma*, *AIP Conf.Proc.* **1121** (2009) 83–89.

[177] A. Strumia and F. Vissani, *Neutrino masses and mixings and...*, .

[178] D. Notzold and G. Raffelt, *Neutrino Dispersion at Finite Temperature and Density*, *Nucl.Phys.* **B307** (1988) 924.

[179] L. Kawano, *Let's Go: Early Universe. Guide to Primordial Nucleosynthesis Programming*, .

[180] L. Kawano, *Let's go: Early universe. 2. Primordial nucleosynthesis: The Computer way*, .

[181] P. J. Kernan and L. M. Krauss, *Refined big bang nucleosynthesis constraints on Omega (baryon) and N (neutrino)*, *Phys.Rev.Lett.* **72** (1994) 3309–3312, [astro-ph/9402010].

[182] R. N. Boyd, C. R. Brune, G. M. Fuller, and C. J. Smith, *New Nuclear Physics for Big Bang Nucleosynthesis*, *Phys.Rev.* **D82** (2010) 105005, [arXiv:1008.0848].

[183] G. M. Fuller and C. J. Smith, *Nuclear weak interaction rates in primordial nucleosynthesis*, *Phys.Rev.* **D82** (2010) 125017, [arXiv:1009.0277].

[184] A. Coc, S. Goriely, Y. Xu, M. Saimpert, and E. Vangioni, *Standard Big-Bang Nucleosynthesis up to CNO with an improved extended nuclear network*, *Astrophys.J.* **744** (2012) 158, [arXiv:1107.1117].

[185] S. Sarkar, *Big bang nucleosynthesis and physics beyond the standard model*, *Rept.Prog.Phys.* **59** (1996) 1493–1610, [hep-ph/9602260]. Dedicated to Dennis Sciama on his 67th birthday.

[186] O. Pisanti, A. Cirillo, S. Esposito, F. Iocco, G. Mangano, et al., *PArthENoPE: Public Algorithm Evaluating the Nucleosynthesis of Primordial Elements*, *Comput.Phys.Commun.* **178** (2008) 956–971, [arXiv:0705.0290].

[187] E. Aver, K. A. Olive, and E. D. Skillman, *An MCMC determination of the primordial helium abundance*, arXiv:1112.3713.

[188] G. Mangano and P. D. Serpico, *A robust upper limit on $N_{\rm eff}$ from BBN, circa 2011*, *Phys.Lett.* **B701** (2011) 296–299, [arXiv:1103.1261].

[189] M. Peimbert, V. Luridiana, and A. Peimbert, *Revised Primordial Helium Abundance Based on New Atomic Data*, *Astrophys.J.* **666** (2007) 636–646, [astro-ph/0701580].

[190] J. Dunkley, R. Hlozek, J. Sievers, V. Acquaviva, P. Ade, et al., *The Atacama Cosmology Telescope: Cosmological Parameters from the 2008 Power Spectra*, *Astrophys.J.* **739** (2011) 52, [arXiv:1009.0866].

[191] R. Keisler, C. Reichardt, K. Aird, B. Benson, L. Bleem, et al., *A Measurement of the Damping Tail of the Cosmic Microwave Background Power Spectrum with the South Pole Telescope*, *Astrophys.J.* **743** (2011) 28, [arXiv:1105.3182].

[192] G. Mangano, G. Miele, S. Pastor, T. Pinto, O. Pisanti, et al., *Relic neutrino decoupling including flavor oscillations*, *Nucl.Phys.* **B729** (2005) 221–234, [`hep-ph/0506164`].

[193] G. M. Fuller, C. T. Kishimoto, and A. Kusenko, *Heavy sterile neutrinos, entropy and relativistic energy production, and the relic neutrino background*, `arXiv:1110.6479`.

[194] G. Gelmini, S. Palomares-Ruiz, and S. Pascoli, *Low reheating temperature and the visible sterile neutrino*, *Phys.Rev.Lett.* **93** (2004) 081302.

[195] G. B. Gelmini, E. Osoba, and S. Palomares-Ruiz, *Inert-Sterile Neutrino: Cold or Warm Dark Matter Candidate*, *Phys.Rev.* **D81** (2010) 063529.

[196] G. M. Fuller, A. Kusenko, and K. Petraki, *Heavy sterile neutrinos and supernova explosions*, *Phys.Lett.* **B670** (2009) 281–284, [`arXiv:0806.4273`].

[197] B. Benson, T. de Haan, J. Dudley, C. Reichardt, K. Aird, et al., *Cosmological Constraints from Sunyaev-Zel'dovich-Selected Clusters with X-ray Observations in the First 178 Square Degrees of the South Pole Telescope Survey*, `arXiv:1112.5435`.

[198] M. Moresco, L. Verde, L. Pozzetti, R. Jimenez, and A. Cimatti, *New constraints on cosmological parameters and neutrino properties using the expansion rate of the Universe to z 1.75*, `arXiv:1201.6658`.

[199] T. Asaka, M. Shaposhnikov, and A. Kusenko, *Opening a new window for warm dark matter*, *Phys.Lett.* **B638** (2006) 401–406.

[200] O. Ruchayskiy and A. Ivashko, *Experimental bounds on sterile neutrino mixing angles*, *JHEP* **1206** (2012) 100, [`arXiv:1112.3319`].

[201] A. Vilenkin, *Equilibrium parity violating current in a magnetic field*, *Phys. Rev.* **D22** (1980) 3080–3084.

[202] A. N. Redlich and L. C. R. Wijewardhana, *Induced Chern-simons Terms at High Temperatures and Finite Densities*, *Phys. Rev. Lett.* **54** (1985) 970.

[203] K. Tsokos, *Topological Mass Terms and the High Temperature Limit of Chiral Gauge Theories*, *Phys. Lett.* **B157** (1985) 413.

[204] A. Y. Alekseev, V. V. Cheianov, and J. Frohlich, *Universality of transport properties in equilibrium, Goldstone theorem and chiral anomaly*, *Phys. Rev. Lett.* **81** (Oct., 1998) 3503–3506.

[205] D. E. Kharzeev, L. D. McLerran, and H. J. Warringa, *The Effects of topological charge change in heavy ion collisions: 'Event by event P and CP violation'*, *Nucl.Phys.* **A803** (2008) 227–253.

[206] D. T. Son and P. Surowka, *Hydrodynamics with Triangle Anomalies*, *Phys.Rev.Lett.* **103** (2009) 191601, [arXiv:0906.5044].

[207] K. Fukushima, D. E. Kharzeev, and H. J. Warringa, *The Chiral Magnetic Effect*, *Phys. Rev.* **D78** (2008) 074033, [arXiv:0808.3382].

[208] D. E. Kharzeev, *The Chiral Magnetic Effect and Anomaly-Induced Transport*, *Prog. Part. Nucl. Phys.* **75** (2014) 133–151, [arXiv:1312.3348].

[209] D. E. Kharzeev and H.-U. Yee, *Anomalies and time reversal invariance in relativistic hydrodynamics: the second order and higher dimensional formulations*, *Phys.Rev.* **D84** (2011) 045025.

[210] K. Fukushima, D. E. Kharzeev, and H. J. Warringa, *The Chiral Magnetic Effect*, *Phys. Rev.* **D78** (2008) 074033.

[211] K. Fukushima, D. E. Kharzeev, and H. J. Warringa, *Real-time dynamics of the Chiral Magnetic Effect*, *Phys. Rev. Lett.* **104** (2010) 212001, [arXiv:1002.2495].

[212] M. Joyce and M. E. Shaposhnikov, *Primordial magnetic fields, right electrons, and the Abelian anomaly*, *Phys. Rev. Lett.* **79** (1997) 1193–1196.

[213] A. Boyarsky, J. Frohlich, and O. Ruchayskiy, *Self-consistent evolution of magnetic fields and chiral asymmetry in the early Universe*, *Phys.Rev.Lett.* **108** (2012) 031301.

[214] M. Dvornikov and V. B. Semikoz, *Magnetic field instability in a neutron star driven by the electroweak electron-nucleon interaction versus the chiral magnetic effect*, *Phys.Rev.* **D91** (2015), no. 6 061301.

[215] M. Dvornikov and V. B. Semikoz, *Generation of the magnetic helicity in a neutron star driven by the electroweak electron-nucleon interaction*, *JCAP* **1505** (2015), no. 05 032, [arXiv:1503.04162].

[216] M. Dvornikov and V. B. Semikoz, *Energy source for the magnetic field growth in magnetars driven by the electron-nucleon interaction*, .

[217] G. Sigl and N. Leite, *Chiral Magnetic Effect in Protoneutron Stars and Magnetic Field Spectral Evolution*, arXiv:1507.04983.

[218] A. Boyarsky, J. Frohlich, and O. Ruchayskiy, *Magnetohydrodynamics of Chiral Relativistic Fluids*, .

[219] D. E. Kharzeev, *The Chiral MagnetoHydroDynamics of QCD fluid at RHIC and LHC*, *J.Phys.* **G38** (2011) 124061, [arXiv:1107.4004].

[220] M. Giovannini, *Anomalous Magnetohydrodynamics*, *Phys. Rev.* **D88** (2013) 063536.

[221] D. T. Son and B. Z. Spivak, *Chiral Anomaly and Classical Negative Magnetoresistance of Weyl Metals*, *Phys. Rev.* **B88** (2013) 104412, [`arXiv:1206.1627`].

[222] A. A. Burkov, *Chiral anomaly and transport in Weyl metals*, *J. Phys. Condens. Matter* **27** (2015) 113201, [`arXiv:1502.07609`].

[223] V. A. Miransky and I. A. Shovkovy, *Quantum field theory in a magnetic field: From quantum chromodynamics to graphene and Dirac semimetals*, *Phys. Rept.* **576** (2015) 1–209.

[224] R. Jackiw and V. A. Kostelecky, *Radiatively induced Lorentz and CPT violation in electrodynamics*, *Phys.Rev.Lett.* **82** (1999) 3572–3575.

[225] R. Jackiw, *When radiative corrections are finite but undetermined*, *Int.J.Mod.Phys.* **B14** (2000) 2011–2022.

[226] S. R. Coleman and S. L. Glashow, *High-energy tests of Lorentz invariance*, *Phys.Rev.* **D59** (1999) 116008.

[227] S. B. Treiman, E. Witten, R. Jackiw, and B. Zumino, *CURRENT ALGEBRA AND ANOMALIES*. 1986.

[228] S. Weinberg, *Gauge and Global Symmetries at High Temperature*, *Phys. Rev.* **D9** (1974) 3357–3378.

[229] S. R. Coleman and B. R. Hill, *No More Corrections to the Topological Mass Term in QED in Three-Dimensions*, *Phys.Lett.* **B159** (1985) 184.

[230] J. Morales, C. Quimbay, and F. Fonseca, *Fermionic dispersion relations at finite temperature and nonvanishing chemical potentials in the minimal standard model*, *Nucl.Phys.* **B560** (1999) 601–616, [`hep-ph/9906207`].

[231] H. A. Weldon, *Covariant Calculations at Finite Temperature: The Relativistic Plasma*, *Phys. Rev.* **D26** (1982) 1394.

Samenvatting

Alhoewel het Standaard Model (SM) van elementaire deeltjes het Heelal succesvol beschrijft tot op de kleinste bekende schalen, weten we dat er een aantal observationele fenomenen bestaan, die niet beschreven worden binnen het raamwerk van deze theorie. Hieronder vallen neutrino-oscillaties, donkere materie en de baryon-asymmetrie van het Heelal.

In dit proefschrift bestuderen we het Neutrino Minimale Standaard Model (νMSM), een minimalistische extensie van het Standaard Model dat alle drie de bovenstaande BSM-fenomenen (Beyond the Standard Model) tegelijk kan beschrijven, doormiddel van het toevoegen van drie rechtshandige neutrinos N_1, N_2 en N_3 aan de bekende drie linkshandige neutrinos. Op deze manier wordt de symmetrie tussen linkshandige en rechtshandige deeltjes, die afwezig is in het Standaard Model, bereikt. Tegelijkertijd worden de massa's van de rechtshandige neutrinos in νMSM gekozen onder de 100 GeV, zodat er geen nieuwe hoge energie schaal wordt toegevoegd aan het Standaard Model.

Hoewel deze nieuwe deeltjes slechts een zwakke wisselwerking hebben met de bekende materie, hebben zij wel een significante uitwerking op het huidige Heelal, voor de volgende reden. Alhoewel de kans dat een enkele steriele neutrino een interactie heeft met een deeltje uit het Standaard Model zeer klein is (vergeleken bij de kans op een interactie tussen de Standaard Modeldeeltjes onderling), wordt de totale kans op een interactie significant op het moment dat we terug gaan naar de tijd van het hete en dichte vroege heelal, vanwege de vele deeltjes die het steriele neutrino op zijn wereldlijn tegen komt. Hieruit volgt dat steriele neutrinos in groten getale geproduceerd kunnen worden en een effect kunnen hebben op de rest van het Heelal. De twee zwaardere deeltjes van νMSM, N_2 en N_3, produceren de baryon- en lepton-asymmetrie van het Heelal en het overgebleven N_1 deeltje speelt de rol van donkere materie en bevat als dusdanig de meeste gravitationele massa in het huidige Heelal.

Het νMSM heeft een groot potentieel om gemeten te worden, aangezien de twee zwaardere N_2 and N_3 deeltjes direct in een deeltjesversneller geproduceerd kunnen worden. Een dergelijk experiment is gepland in CERN, genaamd SHiP (Search for Hidden Particles). Bovendien vervalt het donkeremateriedeeltje N_1 onder productie van een monochromatische Röntgenlijn in de regionen die door donkere materie gedomineerd worden. Dit specifieke signaal kan doormiddel van sterrenkundige waarnemingen worden gemeten.

In dit proefschrift laten we zien dat de steriele neutrinos N_2 en N_3 met massa's kleiner dan 140 MeV (de massa van het π-meson), welke de neutrino-oscillaties verklaren via het wipmechanisme, aanwezig zouden kunnen zijn in het vroege heelal in zulke grote hoeveelheden dat ze de, anders uitstekende, overeenstemming tussen de voorspelling van het Standaard Model voor de productie van lichte elementen tijdens de oerknal en de sterrenkundige waarnemingen hiervan teniet kunnen doen. Op deze manier zijn de steriele-neutrino-massa's van onder begrenst, hetgeen de potentieel interessante parameterruimte voor toekomstige deeltjesversnellerexperimenten verkleint.

Alhoewel N_2 en N_3 de BSM-fenomenen beschrijven die ogenschijnlijk niet gerelateerd zijn aan donkere materie, worden in νMSM de eigenschappen van het donkeremateriedeeltje N_1 beïnvloed door N_2 en N_3. Namelijk, om tegelijk de waargenomen hoeveelheid van donkere materie te produceren en aan de sterrenkundige voorwaarden te voldoen, moet leptonasymmetrie aanwezig zijn in het Heelal op relatief lage temperaturen (onder de 1 GeV). De waarde van deze asymmetrie wordt op hogere temperaturen bepaald door de dynamica van N_2 en N_3. Maar, zoals in dit proefschrift wordt beargumenteerd, is deze dynamica in staat om de productie van magnetische velden op grote schalen in te leiden door het zogenaamde Chirale Magnetische Effect (CME).

CME manifesteert zichzelf op twee manieren. Ten eerste verschijnt het als linkshandige en rechtshandige deeltjes asymmetrisch bevolkt zijn. De fermion massa m is belangrijk voor νMSM, omdat we geïnteresseerd zijn in magnetisch velden op grote schaal, $q \ll m$, waar q een typische golfgetal is van het magnetische veld. In dit proefschrift laten we zien dat CME in dit geval ook aanwezig is, en het moet worden meegenomen in de beschrijving van de νMSM -dynamica in het vroege heelal. CME is in wezen een onevenwichteffect, aangezien de toestand met asymmetrische populatie vervalt naar de symmetrische toestand gedreven door (langzame) processen die het aantal links- en rechtshandige deeltjes veranderen. In deze symmetrische toestand, verwachten we nog steeds dat CME zichzelf manifesteert, aangenomen dat leptonasymmetrie aanwezig is, aangezien de aantallen links- en rechtshandige deeltjes verschillend zijn vanwege de aanwezigheid van pariteitsschendende (zwakke) interacties in het Standaard Model. Op deze manier verwachten we dat de grondtoestand van het plasma verschoven is en dat het magnetische velden op grote schalen bevat. In dit proefschrift laten we echter zien dat het systematisch bijhouden van verschillende bijdragen van de zwakke interacties impliceert dat zij elkaar opheffen en dat de verschuiving van de grondtoestand in werkelijkheid niet plaatsvindt.

We concluderen dat om de evolutie van leptonasymmetrie op lage temperaturen te begrijpen en consistent de hoeveelheid donkere materie te voorspellen en zodoende de parameterruimte van νMSM te verkleinen, het Chirale Magnetische Effect meegenomen moet worden in de beschrijving van het Heelal, samen met de Maxwellvergelijkingen voor het electromagnetische veld en de vergelijking voor chirale asymmetrie. Magnetische velden en elektrische stromen leiden tot de excitatie van macroscopische materiestromen, turbulentie kan ontstaan, en dit systeem moet beschouwd worden met een set van correcte magnetohydrodynamische vergelijkingen, welke de chirale asymmetrie in rekening nemen. Dit is werk voor toekomstige studies.

Summary

Although the Standard Model (SM) of elementary particles successfully describes the Universe up to the smallest known scales, we know that there exists a number of observational phenomena, which do not find explanation in the framework of this theory. Among these problems are Neutrino Oscillations, Dark Matter and the Baryon Asymmetry of the Universe.

In this thesis, we are studying the Neutrino Minimal Standard Model (νMSM), a minimalistic extension of the Standard Model, which can explain all the three above mentioned Beyond the Standard Model (BSM) phenomena simultaneously, by adding only three right-handed neutrinos N_1, N_2, and N_3, to the known three left-handed neutrinos. This way the symmetry between left and right particles, which is absent in the Standard Model, is established. At the same time, the masses of the right-handed neutrinos in the νMSM are chosen to be below 100 GeV, so that no new high energy scale is added to the Standard Model.

Although these new particles interact very weakly with ordinary matter, they nevertheless have a significant impact on the Universe today, for the following reason. Although the probability for an individual sterile neutrino to interact with any Standard-Model particle is suppressed (with respect to the interactions of the SM particles among themselves), once we go back in time to the epoch of the hot and dense early Universe, the total number of the SM particles encountered on the trajectory of the sterile neutrino is so large that the total probability of a sterile neutrino to interact becomes significant. As a result, sterile neutrinos can be produced in large numbers and affect the rest of the Universe. In particular, the two heavier particles of the νMSM, N_2 and N_3, produce the Baryon and Lepton Asymmetry of the Universe, and the remaining particle N_1 plays the role of the Dark Matter particle, and constitutes most of the gravitating matter in the present Universe.

The νMSM has a great potential for discovery, since the two heavier particles N_2 and N_3 can be produced directly in accelerator experiments, like the planned experiment SHiP (Search for Hidden Particles) at CERN. On the other hand, the Dark Matter particle N_1 decays and produces a monochromatic X-ray line in the Dark Matter dominated regions, and this specific signal can be discovered in astrophysical observations.

In this thesis, we show that sterile neutrinos N_2 and N_3 with masses below 140 MeV (mass of π-meson), which explain Neutrino Oscillations via the see-saw mechanism, could have been present in such large amounts in the early Universe that they spoil the otherwise excellent agreement between the Standard-Model prediction of light nuclei production during the Big-Bang Nucleosynthesis and the astrophysical observations. In this way, masses of sterile neutrinos are excluded from below, which reduces the potentially interesting parameter space for future accelerator searches.

Although N_2 and N_3 describe the BSM phenomena, which are apparently not related to Dark Matter, in the νMSM the properties of the Dark Matter particle N_1 *are* affected by N_2 and N_3. Namely, in order to produce the observed abundance of Dark Matter and simultaneously to satisfy the astrophysical bounds, lepton asymmetry should be present in the Universe at relatively low temperatures (below 1 GeV). The value of this asymmetry at higher temperatures is governed by the dynamics of N_2 and N_3. However, as it is argued in this thesis, this dynamics is able to trigger the production of large-scale magnetic fields due to the so-called Chiral Magnetic Effect (CME).

The CME manifests itself in two ways. First, it appears whenever left- and right-handed particles are populated asymmetrically. Fermion mass m is important for the νMSM, since we are interested in large scales of the magnetic field, $q \ll m$, where q is a typical wavenumber of the magnetic field. In this thesis, we demonstrate that CME is present in this case as well, therefore it should be included in the description of the νMSM dynamics in the early Universe. CME is essentially a non-equilibrium effect, since the state with asymmetric population relaxes to a symmetric state due to the presence of (slow) processes that change the number of left- and right-handed particles. In this relaxed state, the CME is still expected to manifest itself, provided that lepton asymmetry is present, since the numbers of left- and right-handed particles are different due to the presence of parity-violating (weak) interactions in the Standard Model. In this way, the ground state of plasma is expected to be shifted, and populated by large-scale magnetic fields. In this thesis it is shown, however, that the systematic account of different contributions of weak interactions implies that they all cancel each other, and the shift of the ground state actually does not happen.

As a conclusion, in order to understand the evolution of lepton asymmetry at lower temperatures, and predict the abundance of Dark Matter consistently, and thus to reduce the parameter space of the νMSM, the Chiral Magnetic Effect should be included in the description of the Universe, together with the Maxwell equations for the electromagnetic field and equation for chiral asymmetry. Magnetic fields and electric currents lead to the excitation of macroscopic matter flows, turbulence may appear, and this system should be considered by a set of correct magnetohydrodynamical equations, which take into account chiral asymmetry. This is the work for future studies.

List of publications

[1] *Experimental bounds on sterile neutrino mixing angles*, *JHEP* **06** (2012) 100 [1112.3319] with Oleg Ruchayskiy [Chapter 2]

[2] *Restrictions on the lifetime of sterile neutrinos from primordial nucleosynthesis*, *JCAP* **1210** (2012) 014 [1202.2841] with Oleg Ruchayskiy [Chapter 3]

[3] *A facility to Search for Hidden Particles at the CERN SPS: the SHiP physics case*, CERN-SPSC-2015-017 (2015) [1504.04855] with Sergey Alekhin, Wolfgang Altmannshofer, Takehiko Asaka, Brian Batell, Fedor Bezrukov, Kyrylo Bondarenko, Alexey Boyarsky and others. [Chapter 2]

[4] *Chiral magnetic current and finite fermion masses* with Alexey Boyarsky and Oleg Ruchayskiy, in preparation. [Chapter 4]

[5] *Long-range magnetic fields from parity-violating interactions in renormalizable gauge theories* with Alexey Boyarsky and Oleg Ruchayskiy, in preparation. [Chapter 5]

Curriculum vitæ

I was born in Kiev, Ukraine, on the 4th of November 1987. I have received the primary education at the Gymnasium No. 136, and the secondary education at the Lyceum No. 171 in Kiev, with specialization in mathematics.

After finishing high school, I entered the Physics Department of the Kiev Taras Shevchenko University in 2005. I have graduated in 2011 with the *cum laude* diploma. My Master thesis was titled “Dark Matter production in the framework of the νMSM model”. After the graduation I started my PhD studies at the Lorentz Insitute for Theoretical Physics in Leiden, under the supervision of dr. Alexey Boyarsky.

During my PhD studies I was a teaching assistant for the course “Particle physics and the early Universe”. I have visited a number of schools and conferences in the Netherlands, Italy, France, and the United Kingdom, where my work was presented.

Acknowledgements

First of all, I want to thank my supervisor Alexey Boyarsky for his scientific (and not only scientific) advices and help, for the constant encouragement during different stages of my PhD studies, for developing my professional skills, and for shaping my current vision of physics.

I am grateful to my promotor Ana Achúcarro, and to my collaborators, Oleg Ruchayskiy, Mikhail Shaposhnikov, Kyrylo Bondarenko, and Andrii Magalich.

I would like to give special thanks to Stanislav Vilchynskyi, Dmytro Iakubovskyi, and to the Scientific and Educational Center of Bogolyubov Institute for Theoretical Physics in Kiev.

I want to express deep gratitude to my wife Inna and to my little son Ivan, to my mother Lyudmila and to my sister Irina, and to my mother-in-law Galyna. Thank you for the inspiration, for the understanding, and for providing the best conditions, which allowed me to concentrate on scientific work.

I thank Bart Clauwens and Wessel Valkenburg for help with the Dutch translation. Finally, I thank the secretaries of our institute, Marianne and Fran, for the help in all sorts of practical things, and all the collegues at the Lorentz Institute for providing great atmosphere.